Extreme Star Formation in Arp 299 from VIXENS: Constraints on the Spatially Resolved SFR–Gas Relations in a Nearby Merger

Amanda Heiderman[1], Neal J. Evans II[1], Karl Gebhardt[1], Guillermo Blanc[2], Timothy A. Davis[3], Casey Papovich[4], Remco van den Bosch[5], Daisuke Iono[6], and Min Yun[7]

ABSTRACT

We investigate the relationship between star formation and gas content in late interaction phase galaxy merger Arp 299 from the VIRUS-P Investigation of the eXtreme Environments of Starbursts (VIXENS) integral field unit (IFU) survey. By comparing IFU Hα and Paα hydrogen recombination line and 24μm data to CO$J = 2 \rightarrow 1$, CO$J = 3 \rightarrow 2$, HCN$J = 1 \rightarrow 0$, HCO$^+J = 1 \rightarrow 0$, and HI maps, we explore the relation between the star formation rate (SFR) and gas surface densities on spatially resolved kpc scales. Extinction laws for a diffuse interstellar medium (R_V= 3.1) and in molecular clouds (R_V= 5.5) are compared and we find the latter to recover the intrinsic Hα/Paα ratio within a factor of $\sim$2, indicating Hα and Paα are heavily extincted and do not reliably trace star formation. Visual extinctions (A_V) from Hα/Hβ and Hα/Paα line ratios are a factor of $\sim$10 below A_V from CO maps. No evidence is found in our IFU data for an AGN in the nuclear regions of IC 694 or near the X-ray confirmed AGN in the nucleus of NGC 3690, however we find high [OI]/Hα and [SII]/Hα extranuclear line ratios which could be attributed to either a Seyfert-like ionization cone or shocked outflow from a superwind. The system average SFR$_{[\mathrm{H}\alpha+24\mu\mathrm{m}]}$ (90$\pm$10 M$_\odot$ yr^{-1}) agrees

[1]Department of Astronomy, University of Texas at Austin, 1 University Station C1400, Austin, TX 78712–0259, USA; alh@astro.as.utexas.edu, nje@astro.as.utexas.edu, gebhardt@astro.as.utexas.edu

[2]Observatories of the Carnegie Institution 813 Santa Barbara Street, Pasadena, California 91101; gblancm@obs.carnegiescience.edu

[3]ESO Karl-Schwarzschild-Strasse 2, D-85748 Garching bei München; tdavis@eso.org

[4]Texas A&M University, Department of Physics and Astronomy, College Station, TX 77843-4242; papovich@physics.tamu.edu

[5]Max-Planck-Institut für Astronomie, Königstuhl 17, D-69117 Heidelberg, Germany; bosch@mpia.de

[6]Nobeyama Radio Observatory, NAOJ Minamimaki, Minamisaku, Nagano, 384-1305, Japan; d.iono@nao.ac.jp

[7]Department of Astronomy, University of Massachusetts, Amherst, MA 01003–9305, USA; myun@astro.umass.edu

well with the total infrared (IR) SFR from IRAS (77±5 $M_\odot$ yr^{-1}), while $SFR_{[H\alpha]}$ and $SFR_{[24\mu m]}$ underestimate the total SFR by factors of ∼4 and 2, respectively. SFRs derived from Paα centered on the nuclear 1.3 kpc regions are a found to be a factor of ∼2 below that derived from $SFR_{[H\alpha+24\mu m]}$. Comparing $SFR_{[H\alpha]}$ to $SFR_{[H\alpha+24\mu m]}$ we find Hα reliably traces star formation in the C-C′ star forming complex and in regions north of the nuclei in the disk of IC 694. An Hα peak to the northwest is associated with the HI peak and a stellar cluster seen in the *HST* optical image suggestive of a tidal dwarf galaxy or possibly a large star cluster in the disk of IC 694 or externally triggered from tidally stripped material. We explore relations between the $SFR_{[H\alpha+24\mu m]}$ and molecular (SFR–Mol) gas surface density using CO$J = 2 \rightarrow 1$ and CO$J = 3 \rightarrow 2$ and find nuclear regions and integrated values to lie on the SFR–Mol gas surface density seen in high-z mergers (Daddi et al. 2010), while regions throughout the merger lie above the high-z relation which is likely due to the choice of CO–to–H_2 conversion factor. The SFR–Dense gas surface density relation in nuclear regions agrees well with the (Gao & Solomon 2004b) relation for normal spirals and (U)LIRGs, however integrated and spatially resolved points lie above this relation with the differences being the choice of HCN$J = 1 \rightarrow 0$ and $HCO^+ J = 1 \rightarrow 0$ to dense gas conversion factor. We compare $\Sigma_{SFR\ [H\alpha]}$ and Σ_{HI} in extranuclear regions and find the SFR–HI surface density relation on 4.7 kpc scales in Arp 299 follows similar trends seen in the outer disks of normal spirals and dwarf galaxies. The average star formation efficiency in extranuclear regions of Arp 299 is higher by a factor of ∼6 compared to spirals and dwarfs, which may indicate star formation is being driven by turbulent motions compressing the gas to dense clumps. Using [NII]/Hα strong line ratio, we find a mean metallicity for Arp 299 to be 12+ log(O/H) of 8.57 and see lower or diluted metallicities in the nuclear region compared to outer regions in agreement with the merger scenario in which galaxy interactions drive gas from outer regions inward. Using the relation between metallicity and CO integrated intensity, we find the a median CO–to–H_2 conversion factor for Arp 299 to be ∼3.2-3.6 $M_\odot$ pc^{-2} $(K\ km\ s^{-1})^{-1}$ which lowers the dispersion in the SFR–Mol relation and moves 1.3 kpc regions in Arp 299 to lie in between the Kennicutt (1998) normal spiral and starburst and Daddi et al. (2010) high-z SFR–gas relations. A relation between IRAS F_{60}/F_{100}–α_{CO} and T_{dust}–α_{CO} gives a range in α_{CO} of 0.67-0.99 $M_\odot$ pc^{-2} $(K\ km\ s^{-1})^{-1}$. This indicates a a Galactic α_{CO} may be more suitable, however α_{CO} likely varies as a function of interaction phase based on whether the system in starburst mode and region by region in galaxy mergers.

Subject headings: stars: formation ISM: clouds — galaxies: ISM — galaxies: interactions — galaxies: starburst — galaxies: star formation — galaxies: individual (Arp 299)

1. Introduction

A detailed understanding of the rate at which molecular gas is converted into stars is an essential prerequisite for models of galaxy formation and evolution. In fact this rate, and the parameters that cause it to vary are currently ill constrained, leading to large uncertainties in theoretical models of galaxy formation. This presents an observational need for a robust determination of the relation between star formation rate (SFR) and the amount of available dense molecular gas. Our focus is to explore the evolution of the rate at which molecular gas is converted into stars through detailed IFU spatially resolved observations of gas-rich nearby interacting galaxies.

Measuring the spatially resolved star formation efficiency in nearby starburst/ interacting galaxies has direct implication at high redshifts, where such galaxies play and increasing role in the total SFR density (Le Floc'h et al. 2005). Recent work by Genzel et al. (2010) and Daddi et al. (2010) found a bi–modal relationship between the SFR and gas surface densities for high redshift merging galaxies and normal disk galaxies (Figure 3). The high redshift mergers from Genzel et al. (2010) lie along the same relation as Galactic low and high mass star forming regions from Heiderman et al. (2010), suggestive that the bulk of gas in merging systems traces star forming gas. While starburst and interacting galaxies are a relatively rarity in the low-z universe, they are the dominant mode of star formation in the distant universe. Understanding the physics of star formation in these systems is therefore paramount. This motivates the observational requirement to study the star formation efficiency in starburst/interacting galaxies.

The idea that there should be a relation between the density of star formation and gas density was first proposed by Schmidt (1959). Schmidt investigated this relation, now known as the "Schmidt law", assuming that it should be in the form of a power law and suggested that the density of star formation was proportional to gas density squared. Observations of many galaxies on global or disk-averaged scales have been fit to a power law of N = 1.4 (Kennicutt 1998). While this relation is previously been called the"Kennicutt–Schmidt law", we refrain from calling this a "law" and instead refer to it as a SFR–gas relation since it is only an assumption that there is *only one relation* that regulates how gas forms stars. Recently, this proposed SFR-gas relation has been studied on ∼kpc scales in nearby spiral galaxies where a deviation from the Kennicut–Schmidt power law index is found (Bigiel et al.

2008; Rahman et al. 2012). While some work on the integrated emission SFR-gas relation in extreme star forming environments has been done (Gao & Solomon 2004a,b), such as those in local (ultra)luminous infrared (IR) galaxies, (U)LIRGs, (Sanders & Mirabel 1996) there has been little work done studying the spatially resolved relation between the SFR and gas surface densities in extreme environments such as the triggered starbursts in interacting galaxies. The VIXENS observational program (Section 1.1) will provide the required constraints on theoretical models for galaxy evolution as well as provide a comparison sample to multiwavelength observational studies of high-z interacting galaxies.

On global scales, the total IR SFR correlates with gas content measured from CO luminosities (e.g., Sanders & Mirabel 1996). However, extreme star forming environments like that in local (U)LIRGs, lie above the classical Kennicutt-Schmidt relation (Genzel et al. 2010; Daddi et al. 2010). With critical densities ∼100-300 times larger than CO, the HCN$J = 1 \rightarrow 0$ line traces dense gas better than CO and is found to have a tighter, linear correlation between the IR SFR over two orders of magnitude in luminosity from normal spirals to (U)LIRGs (Gao & Solomon 2004b), as well as on smaller scales in massive star forming regions (Wu et al. 2005). Furthermore, it has been shown that starbursting IR luminous systems exhibit enhanced dense HCN$J = 1 \rightarrow 0$ gas luminosity compared to CO gas at moderate density (Juneau et al. 2009). This may be due to the gas inflow produced by the gravitational tidal torques into the nuclear region. Alternatively it may be due to an increase in gas velocity dispersion during the interaction, triggering the formation of star forming clouds with densities $\gtrsim 10^4$ cm^{-3} (Gao & Solomon 2004a) far outside the nuclei as predicted in recent theoretical simulations (Bournaud et al. 2010).

Arp 299 is a nearby (z[1] =0.010) infrared luminous ($L_{\rm IR} \sim 5.1 \times 10^{11} L_{\odot}$; Table 2) late interaction phase merger. This systems is composed of two main separate components IC 694 (Arp 299 A) and NGC 3690 with two components Arp 299 B and C (Gehrz et al. 1983). Since Arp 299 is a LIRG, we can assume most of the total bolometric luminosity is emitted in the infrared with luminosity ratios ($\sim L_{\rm IR,NGC\,3690}$:$L_{\rm IR,IC\,694}$ = $1.4{\times}10^{11} L_{\odot}$:$2.6{\times}10^{11} L_{\odot}$ =1:2) and a separation of ∼4.3 kpc, indicative of late interaction stage 2:1 mass ratio major merger. The Arp 299 C-C′ component is considered a non-nuclear component as it has a dense molecular gas concentration (Aalto et al. 1997; Casoli et al. 1999; Imanishi & Nakanishi 2006), but lacks evidence for a significant potential well for it to be considered an individual galaxy as this region does not contain a concentration of old redder stars (Alonso-Herrero et al. 2000). Optical and HI observations (Hibbard & Yun 1999) show that Arp 299 likely results from a prograde- retrograde encounter as the system contains one tidal tail in both the optical

[1]In this paper, we assume a flat cosmology with $\Omega_m = 1 - \Omega_\lambda = 0.3$ and H_0 =70 km s^{-1} Mpc^{-1} and the distance to Arp 299 is 44.1 Mpc and $1'' = 214$ pc.

and HI stripped from the disk of NGC 3690, while the HI disk of IC 694 remains relatively intact and displays one prominent spiral arm with dust lane in the optical (Figure 3, Mihos & Hernquist 1996). The merger is estimated to have occurred ∼750 Myr ago between a gas- rich Sab-Sb galaxy (IC 694) and SBc-Sc galaxy (NGC 3690). Based on this and the rotational speed of 240 km s^{-1} Hibbard & Yun (1999) predict the system will merge in ∼20-60 Myr. The age of star formation bursts in each component ranges from ∼4-5 Myr (C-C′), ∼7.5 My (B), and ∼11 Myr (A) (Alonso-Herrero et al. 2000).

1.1. The VIRUS-P Investigation of the eXtreme ENvironments of Starbursts (VIXENS) Survey

VIXENS[2] is a large integral field unit (IFU) survey of 15 nearby IR bright ($L_{IR} > 3 \times 10^{10} L_{\odot}$) interacting/starburst galaxies (see Heiderman et al. (2011) for full survey description). Our sample is selected to include a full range of interaction stages (from early stage close pairs to late stage systems with multiple nuclei), implied mass ratios of $1/3 < M_1/M_2 \leq 1/1$ estimated from optical luminosity ratios, and existing ancillary data sets including *Spitzer* 24μm, and CO and HI maps. In addition we have single dish line survey of dense gas as traced by molecules such as HCN(1–0), HCO^+(1–0), and HNC(1–0)from Nobeyama 45m and IRAM 30m telescopes for the sample (Davis et al. , in prep.) , as well as HCN(1–0) maps for a subset of our sample from CARMA (Heiderman, Davis et al. , in prep.).

2. Observations

We use the VIRUS-P (now Mitchell Spectrograph) on the 2.7-m Harlan J. Smith telescope at McDonald Observatory. The IFU has a field of view (FOV) of $1.7' \times 1.7'$, and has 246 4.3″ optical fibers with a 1/3 filling factor for which three dithers provide contiguous coverage. The spectra covers the wavelength range 4555–6830Å and has a mean instrumental spectral resolution of ≃5.4Å FWHM or $\sigma_{\rm inst}$ ≃120.5 km s^{-1} (Section 3.1). The observations of Arp 299 were taken on May 16, 2009 with an average seeing of 1.″2. The central coordinates of Arp 299 are J2000 (α, δ) = (11:28:28.33, +58:33:38.6) and we obtain three dithers from the central position at $(\Delta\alpha, \Delta\delta) = (0''.0, 0''.0), (-3''.6, -2''.0)$, and $(0''.0, -4''.0)$ for full coverage of our FOV. We obtained three 10 minute exposures on each dither position bracketed by a 5 minute sky exposure each with a 30′ off position. The spectrophotometric

[2]http://www.as.utexas.edu/ alh/vixens.html

standard star PG1708+602 was observed using a 6–point dither pattern with and exposure time of 200 seconds each to ensure sampling of the PSF for flux calibration. Taking into account one fiber which falls off the CCD due to alignment, this gives a total of 735 individual spectra with a spatial resolution of 4.″235 or ∼900 pc at the distance of Arp 299.

2.1. IFU Data Reduction and Emission Line Flux Measurements

(A.H.- Lots of repetition in this section for reduction of VIRUS-P data compared to the submitted Blanc et al. (2012) VENGA paper. Suggestion was to summarize and cite Blanc et al. (2012). I am leaving this in for now to put into my dissertation, will summarize before circulating/submitting final version.)

2.1.1. Data Reduction, Flux Calibration, Astrometry, and Final Data Products

We provide an overview of the VIXENS IFU data reduction, astrometric calibration, and flux calibration below. A detailed description of data reduction and flux calibration will be included in a forthcoming paper (or rather just in dissertation). The reduction of VIXENS IFU data is performed using the VACCINE reduction pipeline (Adams et al. 2011). Due to the unique gimbal mount design of VIRUS-P, the instrument is kept at constant gravity, providing negligible flexure effects on the light path to the CCD. Bias frames spanning the entire observing run are combined and all data (arc lamp, twilight flat field, sky, and science frames) are first overscan then bias subtracted using the combined bias frame. Cosmic ray rejection is performed on the overscan and bias subtracted science frames using the LA–Cosmic (van Dokkum 2001), an algorithm based on a variation of laplacian edge detection with an additional two pixel buffer applied. Residual cosmic rays such as those that hit the CCD at an oblique angle will be removed when the three frames for each dither position are combined (Section 3.1). A combined twilight flat field frame is made and then used to trace the position of each fiber spectrum on the CCD. The solar spectrum is removed from the master flat field by using a B–spline fit to combined neighboring fibers with similar spectral resolution. Each fiber is then normalized by the combined spectrum and the frame is median smoothed. The Ne+Cd arc frames are combined and the wavelength solution is initially computed using a 4th order polynomial to 10 matched emission lines. Then, all frames are flat fielded using the median smoothed solar spectrum subtracted master flat. The final wavelength solution is determined by using the initial parameters determined before on the flat fielded master arc frame, varying parameters until reaching a solution. Sky subtraction is done in two steps: 1) since the sky brightness varies non-linearly throughout the observations,

we determine a variable fit during the time frame for our science observations as a function of wavelength and 2) the before and after sky frames corrected for this variate for each science exposure are averaged before background subtracting science frames. To perform the first step, we rebin spectra over our science frames (both of Arp 299 and our spectrophotometric standard PG1708+602) into 500 Å bins and measure the median value per bin. A cubic-spline fit to the median rebinned spectra over the time span of our observations were performed to obtain a correction factor to the sky frames. A 5th order polynomial fit to these correction factors as a function of wavelength is determined and sky frames are multiplied by this smooth function to obtain final sky frames. We then perform the second step, averaging the before and after corrected sky frames and use these to background subtract our science frames. The initial astrometric calibration is performed using guide camera pointing that is offset by $\sim 9'$ North of the IFU field which images a $4'.5 \times 4'.5$ FOV positioned on the corresponding pixel coordinates of a guide star. We determine our final astrometry as discussed below.

Observations of spectrophotometric standard PG1708+602 (Massey et al. 1988) are used to perform relative flux calibration as a function of wavelength for the Arp 299 IFU data. Since the IFU only samples a portion of the standard star's PSF, we observe in an overlapping 6–point dither pattern to fully sample the PSF and recover the star's total flux. The centroid position is calculated by taking the first order moment or the weighted average of the fiber fluxes as a function of position, which is used to reconstruct the shape of the PSF. The reconstructed PSF is fit to a Moffat profile which gives the total flux measured in each of the fibers. Each spectrum was normalized by the fraction of total flux sampled and an average value above 5σ was used to determine the total instrumental spectrum. The total spectrum was corrected for atmospheric extinction measured at McDonald Observatory as a function of wavelength and the spectrum of PG1708+602 from Massey et al. (1988) was used to determine our relative flux calibration. We estimate the systematic uncertainty in our relative flux calibration during these observations to be 3.6% by normalizing and averaging derived flux calibration curves as a function of wavelength for the four standard stars obtained during the same VIXENS May 2009 observing run. We use this average flux calibration curves over the entire observing run for our relative flux calibration for Arp 299.

We perform absolute flux calibration and final astrometry using a cross-correlation between a reconstructed broad-band image of Arp 299 from our IFU data with an SDSS-III DR8 r–band image mosaic[3]. We measure the monochromatic flux at the effective wavelength of the r–band filter by integrate each fiber's spectrum over the corresponding SDSS

[3]http://data.sdss3.org/mosaics

transmission curve. The r–band image is simultaneously convolved with a Gaussian kernel to match the PSF plus seeing of our observations and fiber size aperture photometry is performed at each fiber position as determined in our initial astrometric calibration. We then fit a linear relation (F_{r-band} =N×F_{fiber}+B) to the atmospheric extinction corrected IFU fluxes (F_{fiber}) at the airmass of our observations with fluxes from our photometry (F_{r-band}) to recover a normalization factor (N) and residual background (B) for our absolute flux calibration. The mean fit parameters for our three dithers on Arp 299 are $\langle N \rangle = 1.1 \pm 0.001$ and $\langle B \rangle = 5.9 \pm 2 \times 10^{-19}$ erg s^{-1} cm^{-2} Å^{-1} which is a factor of 50 smaller than the continuum level of the average spectrum ($\sim 3 \times 10^{-17}$ erg s^{-1} cm^{-2} Å^{-1}), so sky subtraction residuals are minimal.

Since systematic offsets were found in astrometry between identical pointings over different observations with the largest variations found over different observing runs (Adams et al. 2011), we determine our final astrometry calibration using the SDSS r–band image. To determine and correct for astrometric offsets, we vary the initial astrometry in both RA and DEC by small amounts (ΔRA and ΔDEC) simultaneously during our fit for the absolute flux calibration until a minimum χ^2 is reached for the fit. The average astrometric offsets for the three dither positions for our observations are $\langle \Delta RA \rangle = 3''.3 \pm 0.03$ and $\langle \Delta DEC \rangle = 1''.6 \pm 0.03$, which is within the IFU fiber size. We use the corrected registered coordinates from this procedure as the final astrometry for the Arp 299 data.

2.2. Ancillary Data

2.2.1. Molecular Gas Maps

We use ^{12}CO$J = 2 \rightarrow 1$ and ^{12}CO$J = 3 \rightarrow 2$ maps from the Luminous IR Galaxies Submillimeter Array (SMA) Survey (Wilson et al. 2008) which were corrected for short spacings using the James Clerk Maxwell Telescope (JCMT) (Sliwa et al. 2012) and HCN$J = 1 \rightarrow 0$ and HCO$^+$$J = 1 \rightarrow 0$ maps from Imanishi & Nakanishi (2006) to derive molecular gas masses. The beam sizes for CO$J = 2 \rightarrow 1$ and C)$J = 3 \rightarrow 2$ are $3''.0 \times 1''.8$ and $2''.2 \times 1''.9$, respectively and $4''.2 \times 3''.8$ for the HCN(1–0) and HCO$^+$(1–0) maps. The 1–σ_{rms} noise in each map are 1.7 and 3.5 Jy beam^{-1} km s^{-1} for CO$J = 2 \rightarrow 1$and CO$J = 3 \rightarrow 2$ corresponding to a molecular gas surface density (Σ_{Mol}) of 4.1 and 4.8 M$_\odot$ pc^{-2}(see Section 3.2). The HCN$J = 1 \rightarrow 0$ and HCO$^+$$J = 1 \rightarrow 0$ maps have a 1–σ_{rms} noise level of 545 mJy beam^{-1} km s^{-1} corresponding to a Σ_{Dense} of $\sim$36 M$_\odot$ pc^{-2}(Section 3.2).

2.3. Neutral Hydrogen Map

We use the Very Large Array (VLA) neutral hydrogen (HI) combined C+D array configuration map from Hibbard & Yun (1999) with a robust weighting of 1 and a beam size of $22'' \times 20''$ (4.7×4.3 kpc). The 1–$\sigma_{\rm rms}$ noise per 10.5 km s^{-1} channel in the HI map is 0.30 mJy beam^{-1} which corresponds to a HI gas surface density ($\Sigma_{\rm HI}$) of 0.09 M$_\odot$ pc^{-2}(Section 3.2).

2.3.1. Spitzer 24μm Data

We obtain the *Spitzer* MIPS 24μm image of Arp 299 directly from the *Spitzer* Heritage Archive (P.I. Giovanni Fazio, unpublished). The FWHM of the MIPS PSF at 24μm is 6″. Flux outside of this beam is non-Gaussian, however we only consider flux measurements that lay inner to the first Airy ring so this is a minor concern. To obtain our science image, we set the edges of the Post-Basic Calibrated Data map to zero and fit a plane to the to subtract the background under the assumption this will subtracts both the contribution from zodiacal light and diffuse emission from the Milky Way. The 24 μm image is saturated in nuclear regions (Figure 3) and thus will treat the saturated flux measurements as a lower limit (Section 5).

2.3.2. HST NICMOS Paα *Data*

The nuclear regions of Arp 299 were imaged by *HST* NICMOS 2 by Alonso-Herrero et al. (2000). F190N continuum subtracted F187N Paα images of IC 694 and NGC 3690 were kindly provided by those authors. These images have a FOV of $19''.5 \times 19''.5$ each and a plate scale of $0''.076$ pixel^{-1} (Figure 3). The data reduction, calibration, and continuum subtraction are described in Alonso-Herrero et al. (2000) and references therein.

3. Data Analysis

3.1. Emission Line Flux Measurements

Before we measure emission lines from our calibrated data we first extract the fiber fluxes and combine the three data frames for each dither into a multidimensional row stacked spectrum (RSS) Flexible Image Transportation System (FITS) files. Our final RSS FITS file includes: 1) flux ($F_\lambda(\lambda)$) in units of erg s^{-1} cm^{-2} Å^{-1} and corresponding error in flux

as a function of wavelength, 2) the wavelength at each pixel center, 3) the J2000 Right Ascension and Declination in units of degrees, and 4) the instrumental FWHM as a function of wavelength. To calculate $F_\lambda(\lambda)$, the data is regridded into 1.1Å bins and flux in each fiber as a function of wavelength is computed from the weighted average of the calibrated data in an aperture of five pixels is given by the relation:

$$F_\lambda(\lambda) = \frac{\sum_{i=1}^{5} w_i F_{\lambda,i}(\lambda)}{\sum_{i=1}^{5} w_i}, \quad (1)$$

where w_i are the weights and are the inverse of the errors from VACCINE squared ($w_i = 1/\sigma_i^2$). We make a 3σ cut to remove any residual cosmic rays and mask fluxes and the coordinates are from the final astrometry calibration discussed in Section 2.1. The instrumental spectral resolution as a function of wavelength for each fiber is determined from performing a Gaussian fit to the unblended emission lines in the combined arc lamp frame and then fitting a second order polynomial fit to the FWHM from the Gaussian fits as a function of wavelength. The final instrumental spectral resolution has a range of 4.4–6.1Å with a mean of $\simeq$5.4Å FWHM ($\sigma_{\rm inst}$ $\simeq$120.5 km s^{-1}).

Emission line fluxes are measured using GANDALF software developed by Sarzi et al. (2006). Empirical stellar templates from version 9.1 of the MILES stellar library (Sánchez-Blázquez et al. 2006; Falcón-Barroso et al. 2011) are used. We use a subset of the MILES library containing 72 stars that span a range in luminosity classes (I–V), spectral types (O–M), metallicities (-2 <[Fe/H]<1.5), and include horizontal giant branch and asymptotic giant branch stars. The templates and data are convolved using a changing Gaussian kernel with a FWHM equal to the highest instrumental resolution of the data, $\sigma_{\rm inst}$=149 km s^{-1}. We first mask regions around bright night sky lines that have high residuals from our sky subtraction and use GANDALF to fit the full spectrum of each fiber including the emission lines. In order to more accurately measure emission lines at low S/N, we tie the kinematics of all emission lines to a common gas velocity and dispersion of the Hα the brightest emission line in the spectrum and perform a simultaneous kinematic fit to all lines. The stellar kinematics are measured using the Penalized Pixel-Fitting method, pPXF, (Cappellari & Emsellem 2004) and the details of the kinematic measurements are beyond the scope of this paper and are discussed in detail in (Heiderman et al. , in prep.). A secondary fit it then performed by GANDALF in which is recomputes weights given to stellar templates from the pPXF kinematics solution while modeling emission lines using Gaussian profiles. Figures 1 and 2 show an example of the observed and fit spectrum for both a fiber with a lowS/N as determined using the A/N criteria (Sarzi et al. 2006, Section 6) of 7 and a high A/N of 100. The observed spectrum and 1σ uncertainties are shown in black and the green envelope, respectively. The best fit stellar plus emission line spectrum is shown by the red solid line

and the dotted blue line shows the stellar component of the fit without the emission lines. The vertical green bands are masked regions around sky line residuals.

We derived errors in emission line fluxes by running a Monte Carlo emission line flux simulation assuming errors in line amplitude, velocity, and velocity dispersion are uncorrelated. Since the measurement of the other emission lines are tied to the Hα kinematics, GANDALF provides errors in only the Hα emission line flux, velocity, and velocity dispersion. For all other emission lines, GANDALF only outputs emission line amplitudes and associated errors as well as the velocity and velocity dispersion. For each emission line, we use these line amplitudes, errors in line amplitudes and the Hα line velocity and dispersion errors combined with the instrumental spectral resolution ($\sigma_{\rm inst}$=149 km s^{-1}) to compute simulated emission line fluxes in a Gaussian profile for 100 realizations. To obtain our emission line flux errors, we compute the standard deviation of Gaussian distribution for the 100 simulated emission line fluxes. Table **??** (to be made) is a list of all measured emission line parameters.

3.2. Molecular Gas Surface Density Measurements

We derive molecular hydrogen (H_2) gas surface densities from the maps of CO $J = 2 \rightarrow 1$ and $J = 3 \rightarrow 2$, made with the SMA and corrected for short spacings with data from the JCMT (Sliwa et al. 2012) (Section 2.2.1).

These integrated intensities are first put on the scale of the integrated intensity of the $J = 1 \rightarrow 0$ line (I(CO)) in K km s^{-1}. by assuming a constant ratio R_{ij} =CO($J = i \rightarrow i - 1$)/CO($J = j \rightarrow j - 1$). Sliwa et al. (2012) find the following average values over their maps: $R_{21} = 1.4 \pm 0.08$, and $R_{31} = 0.95 \pm 0.09$.

The mass surface density is then

$$\Sigma_{\rm H_2} = \alpha_{\rm CO} \times R_{ij} \times \left(\frac{I({\rm CO})}{\rm K\ km\ s^{-1}} \right) (M_\odot\ {\rm pc}^{-2}) \quad (2)$$

where $\alpha_{\rm CO}$ is a conversion factor to surface density from the integrated intensity of CO $J = 1 \rightarrow 0$. For local clouds in the Milky Way, $\alpha_{\rm CO} = 3.6\ {\rm M}_\odot\ {\rm pc}^{-2}({\rm K\ km\ s^{-1}})^{-1}$, but centers of galaxies, including the Milky Way, have evidence for values lower by factors of 3 to 10. Based on LVG models of their CO and ^{13}CO data, Sliwa et al. (2012) find a best match for $\alpha_{\rm CO} = 0.4 \pm 0.3\ {\rm M}_\odot\ {\rm pc}^{-2}({\rm K\ km\ s^{-1}})^{-1}$. This value is consistent with the values of $\alpha_{\rm CO} = 0.35 - 0.42\ {\rm M}_\odot\ {\rm pc}^{-2}({\rm K\ km\ s^{-1}})^{-1}$ found by Papadopoulos et al. (2012) for Arp 299, using LVG models of single-dish data (check) including higher J lines of CO and

lines of HCN. Since the resulting molecular mass (1–1.2×10^9 $M_\odot$) using this range of α_{CO} values would imply a star formation rate per unit gas mass above the usual maximum value, Papadopoulos et al. (2012) suggest that higher values of α_{CO} remain possible if most of the gas is in dense gas structures that are forming stars with maximum efficiency.

We will adopt the value of $\alpha_{CO} = 0.40 \pm 0.3$ $M_\odot$ pc^{-2}(K km s^{-1})$^{-1}$ However we consider the possibility of higher values in Section 7.6.1. An additional factor of 1.37 to include helium was applied to our gas surface density measurements resulting in $\Sigma_{Mol} = 1.37\Sigma_{H_2}$. As discussed by Kennicutt & Evans (2012) these simple conversion factors can hide a great deal of uncertainty and variability from place to place in a galaxy.

We also consider dense gas tracers, in particular, the $J = 1 \rightarrow 0$ transitions of HCO$^+$(1–0) and HCN(1–0). These transitions have critical densities that are roughly 100-300 times larger than those of CO for $T_K = 100$ K. The critical density (e.g., 2.7×10^6 cm^{-3} for HCN $J = 1 \rightarrow 0$ at $T_K = 100$ K) will greatly overestimate the actual density. For example, to produce a radiation temperature for HCN $J = 1 \rightarrow 0$ of 1 K at $T_K = 100$ K in a resolved region with typical column density, an effective density (for definition and examples, see Evans 1999; Reiter et al. 2011) of 6.0×10^3 cm^{-3} will suffice. However, the same argument applies to CO, with the result that the ratio of effective densities is also 300 to 1000.

Dense molecular gas surface densities were calculated using the relation:

$$\Sigma_{\rm Dense} = \alpha_{\rm Dense} \left(\frac{I({\rm Dense})}{\rm K\ km\ s^{-1}} \right) (M_\odot\ {\rm pc}^{-2}) \quad (3)$$

where I(Dense) is the integrated intensity of a tracer of denser gas and $\alpha_{\rm Dense}$ is a conversion factor parallel to α_{CO}. From a study of dense clumps in the Milky Way, Wu et al. (2010) found

$$\log(L_{\rm HCN(1-0)}) = 1.04 \times \log(M_{\rm Vir}(R_{\rm HCN(1-0)})) - 1.35, \quad (4)$$

where $L_{\rm HCN(1-0)}$ is the HCN(1–0) line luminosity and $M_{\rm Vir}$ is the virial mass inside the radial distribution. This relation would suggest a value of $\alpha_{\rm Dense} \sim 20$ $M_\odot$ pc^{-2}(K km s^{-1})$^{-1}$. A commonly used value for extragalactic studies is $\alpha_{\rm Dense} = 10$ $M_\odot$ pc^{-2}(K km s^{-1})$^{-1}$ (Gao & Solomon 2004b; García-Burillo et al. 2012). These simple conversions are subject to the same caveats that apply to α_{CO}, as discussed in detail by Papadopoulos et al. (2012) and García-Burillo et al. (2012).

Observations by Imanishi & Nakanishi (2006) with a 4.″2 by 3.″8 beam, using the Nobeyama Millimeter Array show strong HCN and HCO$^+$ emission toward component A, and weaker emission by both toward component C, but only rather weak HCO$^+$ emission toward component B1. While Graciá-Carpio et al. (2006) have argued that X-rays from AGN enhance

the HCN emission, Imanishi & Nakanishi (2006) show that all the HCN/HCO^+ ratios in Arp 299, even those toward the AGN in component B, are consistent with starburst ratios, suggesting that the large quantity of dense gas may mitigate any effects from X-rays.

From the maps in Sliwa et al. (2012) and Imanishi & Nakanishi (2006), kindly supplied by those authors, we computed line luminosities and mean line intensities in circular apertures of 4.″235 diameter (corresponding to 0.9 kpc) around components A, B1, C and C′. If we use $\alpha_{\rm Dense} = 10$ $M_\odot$ pc^{-2}/(K km s^{-1}) for both HCN and HCO^+ emission, the resulting $M_{\rm Dense} = 3.7 \times 10^8$ $M_\odot$ for HCN and 4.6×10^8 $M_\odot$ for HCO^+ in component A, exceeds the total molecular mass from CO of $3 - 3.6 \times 10^8$ $M_\odot$, indicating that $\alpha_{\rm Dense}$ is lower for the same kind of reasons that $\alpha_{\rm CO}$ appears to be lower. Alternatively, $\alpha_{\rm CO}$ may be higher that we assumed, which would allow a higher value of $\alpha_{\rm Dense}$.

We adopt values of $\alpha_{\rm CO} = 0.4 \pm 0.3$, with a correction of 1.37 for He, and $\alpha_{\rm Dense} = 5 \pm 2.5$ (assuming a 50% error in $\alpha_{\rm Dense}$) for further analysis. As a result, the mean mass surface densities in a 4.″235 diameter aperture centered on region A are $\Sigma_{\rm Mol} = 460 - 560$ $M_\odot$ pc^{-2} for CO $J = 2 \rightarrow 1$ and $J = 3 \rightarrow 2$, respectively, and $\Sigma_{\rm Dense} \leq 289 - 358$ $M_\odot$ pc^{-2} for HCN and HCO^+, respectively (Table 1). Masses and surface densities for the other regions are lower, with $\Sigma_{\rm Mol}$ lower by factors of 3-4. HCN is only clearly detected outside region A for region C; however all three components show clear detections in maps with more sensitivity (Casoli et al. 1999).

Since the molecular gas maps only reliably cover the central regions of Arp 299 with significant $\gtrsim 3\sigma$ detections, we use the neutral hydrogen (HI) map of Arp 299 from Hibbard & Yun (1999) (Section 2.3) to measure atomic hydrogen gas surface densities outside the nuclear regions. $\Sigma_{\rm HI}$is calculated from the integrated HI brightness temperature including a factor of 1.37 for helium using the relation:

$$\Sigma_{\rm HI} = 1.99 \times 10^{-2} \left(\frac{I({\rm HI})}{\rm K\ km\ s^{-1}} \right) (M_\odot\ {\rm pc}^{-2}) \quad (5)$$

The HI distribution is likely associated with the disk of IC 694 as the HI (Hibbard & Yun (1999), their Figure 3) and Hα kinematics from our IFU data (Figures 4 and 5) are consistent. However, there is a disassociated peak in Hα velocity near the HI peak in the southeast. The central region of Arp 299 is seen in HI absorption against all the nuclear continuum sources, A, B1, C, and C′ (Baan & Haschick 1990) with an estimated integrated $\Sigma_{\rm HI}$∼8-16 $M_\odot$ pc^{-2} (Hibbard & Yun 1999). The HI absorption is found to have both a broad and narrow component at the systemic velocities of IC 694 and NGC 3690, respectively and Baan & Haschick (1990) conclude that the absorbed HI originates from the outer disks of IC 694 and NGC 3690. Since this material is not associated with the nuclear regions where

we have CO, HCN, and HCO^+ coverage, we do not include it in our analysis.

4. Extinction

The observed line flux ratio of two lines (e.g., Hα and Hβ) can be used to determine the foreground extinction that the lines suffer if we know the intrinsic ratio of those lines $(F_{\rm H\alpha}/F_{\rm H\beta})_{\rm int}$ and the ratio of total to selective extinction for those lines, $R_{\rm H\alpha} = A_{\rm H\alpha}/E(\beta-\alpha) = \kappa({\rm H\alpha})/(\kappa({\rm H\alpha})-\kappa({\rm H\beta})$, where $\kappa({\rm H\alpha})$ is the opacity at the wavelength of Hα.

$$\begin{aligned} A_{\rm H\alpha} &= E(\beta-\alpha)R_{\rm H\alpha} \\ &= -2.5\log\left[\left(\frac{F_{\rm H\alpha}}{F_{\rm H\beta}}\right)_{\rm obs} - \left(\frac{F_{\rm H\alpha}}{F_{\rm H\beta}}\right)_{\rm int}\right] \times \\ &\qquad \left(\frac{\kappa({\rm H\alpha})}{\kappa({\rm H\alpha})-\kappa({\rm H\beta})}\right) \end{aligned} \tag{6}$$

A similar equation applies for the ratio of Paα to Hα, with $R_{\rm Pa\alpha} = \kappa({\rm Pa\alpha})/(\kappa({\rm Pa\alpha})-\kappa({\rm H\alpha})$.

Since the nebular conditions in starburst galaxies are well constrained to have electron densities of $n_e \sim 5\times10^2-5\times10^4$ cm^{-3}) and low temperatures, $T_e \sim 5\times10^3$ K (Roy et al. 2008 and references therein), the range of case B recombination line intensities is small. We adopt intrinsic Hα/Hβ and Hα/Paα flux ratios of 3.00 and 7.58, respectively for a temperature of 5×10^3 K and a density of 10^4 cm^{-3} from Osterbrock & Ferland (2006).

Galactic extinction laws (Draine 2003) vary with density and R_V increases from 3.1 in the diffuse interstellar medium to something similar to $R_V = 5.5$ in molecular clouds. Because the overall extinction is high in Arp 299, we apply both extinction laws to see how much difference they make. Using values of κ from the online tables[4], we find $R_{\rm H\alpha} = 1.997$ for $R_V = 3.1$ and $R_{\rm H\alpha} = 2.841$ for $R_V = 5.5$. For Paα, $R_{\rm Pa\alpha} = 0.236$ for $R_V = 3.1$ and $R_{\rm Pa\alpha} = 0.212$ for $R_V = 5.5$.

Over the smaller (19.″5 by 19.″5) region with Paα data, we can compute extinctions from comparing Paα to Hα, using the data from Alonso-Herrero et al. (2000) described in Section 2.3.2. We linearly interpolate the Hα IFU data on to a grid with a pixel scale of 0.5″, we convolve the higher resolution NICMOS image to match the fiber sized Gaussian

[4]Available at http://www.astro.princeton.edu/ draine/dust/dust.html

FWHM and use fiber sized apertures diameter of 4.″235 (0.9 kpc) to measure the line fluxes from our Hα map and the Paα image.

In Figures 6 and 7, we show the Hα flux after extinction correction using the Balmer decrement versus extinction-corrected Paα flux, using the Hα/Paα line ratio and a histogram of the ratios of the extinction-corrected Hα fluxes and Paα fluxes. We also show Paα contours (yellow) overlaid on our Hα IFU map (red) in Figure 3. The black dashed line indicates the intrinsic Hα/Paα line ratio of 7.58 from case B recombination theory for a typical starburst galaxy as discussed above. Values for the four densest concentrations of star formation, A, B1, C, and C$'$ are used as test cases. Since the Paα image could not be registered properly (Alonso-Herrero et al. 2000), we choose apertures centered on the Paα peaks of A, B1, and C (Figure 3). We could not determine the Paα peak reliably to C$'$, so we do not include a measurement of that region. Correcting for extinction using $R_V = 5.5$ works substantially better, yielding a mean ratio of 3.8 for extinction corrected Hα to extinction corrected Paα, while $R_V = 3.1$ gives a mean ratio of 2.7. These values are factors of $\sim$2 and 3 below the intrinsic Hα/Paα line ratio for R_V of 5.5 and 3.1, respectively. However, even with $R_V = 5.5$, in three dense regions of star formation lie well below the expected ratio, indicating that neither the Hα or Paα line reliably trace all of the star formation.

We can compare the extinctions from the recombination lines to other estimates. For convenience, we refer extinctions in the V–band. For $R_V = 3.1$, $A_V/A_{\mathrm{H}\alpha} = 1.552$ versus 1.94 for $R_V = 5.5$. For the nuclear regions A, B1, C, and C$'$ using the Balmer decrement and R_V= 5.5, A_V is 1.3, 1.2, 0.78, 0.66 mag and using the Hα to Paα line ratio for A, B1, and C, A_V is 2.3, 1.6, and 1.4 mag. Using the gas surface densities from Section 3.2, and the Draine (2003) R_V= 5.5 extinction law, we would predict a total extinction in the visible for the four regions of $A_V = 29$, 11, 7.9, and 6.9 mag for A, B1, C, and C$'$, respectively. Figures 8 and 9 show the spatial distribution and histogram of A_V from the Balmer decrement fiber measurements. Figure 10 shows the fiber to fiber extinction corrected Hα map using the Draine (2003) R_V = 5.5 extinction law.

5. Star Formation Rates and Surface Density Measurements

We use star formation calibrations from Murphy et al. (2011) to derive SFRs with a consistent Kroupa (Kroupa 2001) IMF. The Hα based SFR (SFR$_{[\mathrm{H}\alpha]}$) is calculated using the extinction corrected Hα line flux from Section 4 by the following equation:

$$\mathrm{SFR}\ [\mathrm{H}\alpha]\ (M_\odot\ \mathrm{yr}^{-1}) = 5.37 \times 10^{-42} \mathrm{L}_{\mathrm{H}\alpha,\mathrm{cor}}\ (\mathrm{erg\ s}^{-1}). \quad (7)$$

Assuming an intrinsic Hα/Paα line ratio of 7.58, we convert the SFR$_{[\mathrm{H}\alpha]}$ from Murphy et al. (2011) into a Paα SFR (SFR$_{[\mathrm{Pa}\alpha]}$) by the following relation:

$$\mathrm{SFR}\ [\mathrm{Pa}\alpha]\ (M_{\odot}\ \mathrm{yr}^{-1}) = 4.07 \times 10^{-41} \mathrm{L}_{\mathrm{Pa}\alpha}, \mathrm{cor}\ (\mathrm{erg\ s}^{-1}). \quad (8)$$

We compute the 24μm based SFR using the formula:

$$\mathrm{SFR}\ [24\mu\mathrm{m}]\ (M_{\odot}\ \mathrm{yr}^{-1}) = 5.58 \times 10^{-36} \nu \mathrm{L}_{\nu}, 24\mu\mathrm{m}\ (\mathrm{erg\ s}^{-1}). \quad (9)$$

Since we find Hα and Paα do not reliably trace all the star formation (Section 4), we will also use the 24μm corrected observed Hα flux plus the 24μm to derive the SFR$_{[\mathrm{H}\alpha+24\mu\mathrm{m}]}$, accounting for the obscured and unobscured star formation using the equation:

$$\mathrm{SFR}\ [\mathrm{H}\alpha + 24\mu\mathrm{m}]\ (M_{\odot}\ \mathrm{yr}^{-1}) = 5.37 \times 10^{-42}\ [\mathrm{L}_{\mathrm{H}\alpha,\mathrm{obs}} + 0.031\mathrm{L}_{24\mu\mathrm{m}}](\mathrm{ergs}^{-1}). \quad (10)$$

We calculate the SFR surface density of each SFR tracer using the relation:

$$\Sigma_{\mathrm{SFR}}\ [\mathrm{tracer}] = \frac{\mathrm{SFR}\ [\mathrm{tracer}]}{\mathrm{A}_{\mathrm{kpc}}}\ (\mathrm{M}_{\odot}\ \mathrm{kpc}^{-2}), \quad (11)$$

where tracer is either Hα, Paα, or Hα+24μm and A$_{\mathrm{kpc}}$ is the area of the measurement aperture in kpc. We measure the SFR surface densities using SFR$_{[\mathrm{H}\alpha]}$ and SFR$_{[\mathrm{Pa}\alpha]}$ using apertures on fiber sized scales of 4$''$.235 (0.9 kpc). For the 24μm SFR prescriptions we are limited to the FWHM of the 24μm PSF which is 6$''$ (1.3 kpc) and thus we derive SFR$_{[24\mu\mathrm{m}]}$ and SFR$_{[\mathrm{H}\alpha+24\mu\mathrm{m}]}$ surface densities on this scale. We show measurements for the nuclear star forming regions of Arp 299 in Table 1 and discuss the results in Section 7.

6. Active Galactic Nuclei Activity in Arp 299

Since our goal is to investigate the star formation activity in Arp 299, we must first disentangle any contribution from an AGN component in the nuclear regions. The difficult aspect of separating a starburst region from an AGN in a LIRG is that the concentration

of gas and dust fueling the central energy source typically obscure the AGN. Methods to investigate the presence of an buried AGN typically require 1) hard X-ray band ($E > 2$ keV) measurements where the AGN spectral signature of Fe-Kα lines appear and the AGN emits stronger at this wavelength than a starburst, 2) millimeter interferometric observations that look for chemical signatures, and 3) infrared spectroscopy. We can however use our extinction corrected IFU optical emission line fluxes to explore Baldwin-Phillips-Terlevich (BPT) diagrams (Baldwin et al. 1981) and classify the dominate energy sources in IC 694 and NGC 3690 on a fiber-by-fiber basis and compare that to previous studies.

Using the [OIII] /Hβ and [NII]/Hα emission line fluxes, Coziol et al. (1998) showed that IC 694 can be classified as a pure starburst, while NGC 3690 showed properties that border starburst and liner classification. García-Marín et al. (2006) used integral field spectroscopy and separated IC 694 and NGC 3690 into nuclear components A and B, respectively, as well as an interface region C between the nuclei. They found that the nucleus B of NGC 3690 showed clear signs of an AGN with a mix of starburst and liner-like ionization surrounding the nucleus. Nucleus A in IC 694, however, was found to be starburst dominated and surrounded by liner-like ionization.

X-ray observations from the *BeppoSAX* satellite (Della Ceca et al. 2002) showed the presence of a highly obscured ($N_{\rm H} \simeq 2.5 \times 10^{24}{\rm cm}^{-2}$) AGN in Arp 299, however the spatial location remained unresolved. Later $XMM-Newton$(Ballo et al. 2004) and high resolution *Chandra* (Zezas et al. 2003) observations showed the clear presence AGN in the nuclear region B1 of NGC 3690 and recovered positional coordinates. Evidence remains ambiguous, however, that central power source in nuclear region of IC 694 is an AGN. Observations indicate the possibility of an obscured ($N_{\rm H} \leq 10^{22} cm^{-2}$) low luminosity ($L_X \sim 10^{41}{\rm ergs}^{-1}$) AGN surrounded by a strong nuclear starburst in IC 694, however this may be due to integrated emission from X-ray binaries combined with a thermal component.

Infrared imaging (Gallais et al. 2004 and references therein) and spectroscopy (Gallais et al. 2004; Imanishi & Nakanishi 2006), as well as interferometric observations (Imanishi & Nakanishi 2006) of Arp 299 to investigate the presence of a buried AGN. These studies find NGC 3690 nuclear region clearly harbor a dust enshrouded AGN, however no clear AGN signatures from the nuclear region of IC 694 was seen and evidence points to a pure nuclear starburst as the dominant energy source.

BPT diagnostic diagrams for extinction corrected line ratios in Arp 299 are shown in Figures 11-13. These diagrams show the relative strengths of emission lines to determine the nebular conditions, either photoionization dominated by star formation or photoionization dominated by a hard radiation field from an accretion disk of a central AGN. We select fibers based on the Kewley et al. (2001) extreme starburst criteria (red solid line and hashed

diagonal line region) where AGN dominated fibers lie above that criteria and starburst/HII region dominated fibers lie below. To make a S/N cut, we use the line amplitude–to–noise ratio ($A/N \geq 4$) as defined in Sarzi et al. (2006). We checked individual spectra by eye for the [OIII] (6300Å) line which is red shifted near a bright sky line at 6363.78Å and for [SII](λ6717Å+λ6731Å), which lies near the edge of the VIRUS-P chip and in some fibers falls completely outside the chip. For the 121 fibers that contained both [SII] lines, we found a mean ratio of [SII]λ6731Å/[SII]λ6717Åof 0.74±0.09 and applied it to the 332 fibers that contained only the strongest [SII] (6717Å) line. The top panels in Figures 11-13 show the points selected from our criteria and the bottom panels show the position of fibers on flux map. The Kewley et al. (2006) Seyfert-LINER line is shown by the blue solid and dashed lines on the [OIII] /Hβ versus [SII]/Hα and [OIII] /Hβ versus [OI]/Hα BPT diagrams. The integrated line ratios for the whole system are shown as yellow stars. Points that lie above the Kewley et al. (2001) starburst criteria are shown as solid stars. The hard ($E > 2$ keV) *Chandra* X-ray centroid position for the confirmed AGN in NGC 3690 is marked by a thick cross in the right panels in Figures 11-13. Four fiber regions around this centroid that might be contaminated that lie within the hard X-ray region, a 6″ radius of the X-ray centroid, are also indicated by crosses.

We find 164 extra nuclear regions that lie above the Kewley et al. (2001) starburst criteria in at least two of the the [OIII] /Hβ versus [SII]/Hα and [OIII] /Hβ versus [OI]/Hα BPT diagrams and those points are outlined with boxes in Figures 11-13. Four fibers that show clear Seyfert-like ionization in three BPT diagrams are shown as white stars. Two of these regions lie far from the nuclear regions have low A/N ∼4-10 and low S/N ∼3–7 as defined by the line flux over the error in line flux so low we discount these regions as AGN contaminated. The AGN selected fibers are denoted by stars in all three BPT diagrams and lie near, but on opposites sides of the X-ray centroid in NGC 3690 and are likely a signature of photoionization of the extranuclear interstellar gas by the central AGN or a shocked outflow from a starburst superwind (Heckman et al. 1999). A Seyfert-like ionization cone located below the nuclear region of NGC 3690 was first reported by García-Marín et al. (2006) using integral field spectroscopy, however their data did not cover the region of high ionization above the nucleus so they only saw high line fluxes below the nuclear region in NGC 3690. The other possibility is that the interstellar gas, especially the regions that aren't Seyfert-like, are being heated by photoionization by massive stars. Many regions that lie outside >3kpc from the nuclear regions show a high [OI]/H$\alpha$and [SII]/Hα ratios which could also be explained by a large population of Wolf-Rayet (W-R) stars that are a signature of recent star formation. W-R stars have higher effective temperatures than OB stars and provide more hard energy photons for excitation of the interstellar gas. Another possibility are cooling shocks (Dopita & Sutherland 1995). These shocks would naturally

form outside of the starburst nucleus due to supernova explosions that followed shortly after the starburst leading to a superwind blow out or shocked outflow of interstellar gas from the nuclear region. There is also an area of dense gas as traced by CO$J = 3 \rightarrow 2$ (Figure 16) as well as a region of higher metallicities (Section 7.6.1) that trace a potential outflow from a starburst superwind. Heckman et al. (1999) used a combination of X-ray data and long slit spectra that intercepted the nuclear regions B1 and C concluded that Arp 299 had enough internal energy to heat up the ISM to significant temperature and outflow velocity such that gas may be able to escape from the system, making a superwind dominated system is highly plausible. We mark both regions within a 6″ radius of the X-ray centroid (Zezas et al. 2003) as well as the 164 extranuclear regions that were selected by the AGN criteria in the BPT diagrams throughout the paper.

7. Results

7.1. Comparison of Global SFRs

We measure the system wide average or global SFRs for the Arp 299 merger in a contour aperture region that has a $A/N \geq 4$ in Hα line flux as determined from our interpolated Hα map. For the SFR comparisons, we use Murphy et al. (2011) calibrations that have a common (Kroupa (2001) IMF). These measurements are shown in Table 2 and an image showing all star formation tracers is shown in Figure 3. Comparing to the total SFR_{IR} of 76.6±4.6 $M_\odot$ yr^{-1} from IRAS, we are only recovering $\lesssim$1/4 of the global SFR from the Hα flux from our IFU data ($SFR_{[H\alpha]}$ = 18.9±0.7 $M_\odot$ yr^{-1}), and $\lesssim$1/2 of the total IR SFR from the saturated 24 μm image ($SFR_{[24\mu m]}$ = 43.6±6.3 $M_\odot$ yr^{-1}). However, when we correct the observed Hα flux using 24μm we obtain a total $SFR_{[H\alpha+24\mu m]}$ of 89.8±9.9 $M_\odot$ yr^{-1} in agreement with the SFR from IRAS within the errors. Since the beam sizes of the IRAS 60 and 100μm (see Table 2) bands are $1.5' \times 4.75'$ and $3' \times 5'$, respectively, it fully covers the Arp 299 merger so there is little missing IR flux. The Paα image only covers the nuclear regions so we can only estimate the $SFR_{[Pa\alpha]}$ to be $\gtrsim$13±3 $M_\odot$ yr^{-1}, similar to the *total* Hα flux over the whole system. A comparison of the$SFR_{[Pa\alpha]}$ to $SFR_{[H\alpha+24\mu m]}$ show the $SFR_{[H\alpha+24\mu m]}$ are a factor of $\gtrsim$2 higher on average in 6″ regions centered at the peak Paα emission. This is due to the high extinction in both the Paα and Hα line fluxes. Since the total SFR_{IR} from IRAS is in agreement with the total $SFR_{[H\alpha+24\mu m]}$ within the errors, we use this SFR indicator for the rest of our analysis with the exception of the comparison to HI (Section 7.6).

7.2. Region–by–Region Comparison of SFRs

In order to directly compare our IFU data to the *Spitzer* 24 μm map, we convolve our interpolated Hα map using a Gaussian kernel with a FWHM of the *Spitzer* 24μm 6″ PSF then regrid onto the 2.45″ plate scale of the 24 μm image. We measure our Hα map and 24 μm image in only regions where the Hα fiber flux has a $A/N \geq 4$ using apertures matched to the 6″ ($\sim$1.3 kpc) 24μm image PSF. In Figure 14, we compare the SFR derived from the observed Hα flux corrected by the 24μm flux versus the Balmer decrement extinction corrected Hα SFR. Regions determined to be contaminated by an AGN in NGC 3690 by either the X-ray or optical spectroscopy from our IFU fiber analysis are marked by open squares. We find a non-linear relation which indicates our extinction corrected Hα flux is underestimating the total SFR in each region by at least a factor of $\sim$10 on average compared to the observed Hα flux corrected by the saturated 24μm SFR. While the average ratio of these two SFR tracers is very high, there are regions that are not as heavily extincted where the Balmer decrement extinction corrections show an Hα flux great enough to match the 24μm, Hα corrected flux when both are converted to SFRs.

In order to understand where SFRs derived using Hα might be reliable in a nearby merger, we show the distribution of the ratio of $SFR_{[H\alpha+24\mu m]}/SFR_{[H\alpha]}$ across the Arp 299 system in Figure 14 (bottom panel). We find a range of values for the ratio of $SFR_{[H\alpha+24\mu m]}$ to $SFR_{[H\alpha]}$ from 1 (linear, see Figure 14 top panel) to 60. This figure shows that dark blue regions near the C-C′ complex, above both nuclei, and a region to the northwest (top right) where the Hα flux is high enough to match the Hα corrected 24μm flux converted to a SFR. Most of these regions lie at low extinction (Figure 8), except for the region above both nuclei where there is a peak in the extinction map from the Balmer decrement. From this figure we show that Hα flux likely traces the younger stellar population in regions that lie outside the nuclei in the north outer region of the Arp 299 merger.

We have measured $\Sigma_{SFR\ [H\alpha]}$, $\Sigma_{SFR\ [Pa\alpha]}$, $\Sigma_{SFR\ [24\mu m]}$, and $\Sigma_{SFR\ [H\alpha+24\mu m]}$ in both fiber (4″.235) and 6″ scale regions of 0.9 and 1.3 kpc, respectively in nuclear regions A, B1, C and C′ with the exception that we only measure at the peak Paα emission at the location of the C-C′ region. Figure 15 shows the distribution of $\Sigma_{SFR\ [H\alpha+24\mu m]}$ on 1.3 kpc scales and Table 1 shows the measurements each tracer and region size. The nucleus of NGC 3690, B1, has the highest SFR surface density in all tracers using 24μm fluxes, which could mean there is contamination from the AGN in the region measured or the other regions have lower fluxes due to image saturation (Section 2.3.1). However, AGN contamination should not be the case since a measurement on either size scale lies outside of the X-ray emission peak (Section 6) and the potential IFU AGN contaminated regions. Measurements using 24μm fluxes ($\Sigma_{SFR\ [H\alpha+24\mu m]}$, $\Sigma_{SFR\ [24\mu m]}$) show that after region B1, the star forming

complex region C has the highest SFR surface density followed by nucleus A and region C′. Region C has the highest $\Sigma_{\rm SFR\ [H\alpha]}$, which is likely due to low extinction (Figure 8), in that region and Hα is a more reliable SFR tracer. The next highest $\Sigma_{\rm SFR\ [H\alpha]}$ is seen in IC 694 nucleus (region A), followed by regions B1 and C′. Since nuclear region A is classified as pure starburst (Section 6), a low SFR surface density using recombination lines is likely due to a high level of extinction in Hα and Paα even as discussed in Section 4.

The northwest region of this system shows evidence for star forming complex associated with and Hα peak and the peak in the HI gas distribution in both the map from Hibbard & Yun (1999) and a higher resolution (10″) map from Stanford & Wood (1989). This region lies at low extinction (Figure 8) and contains a close association of stars visible in the *HST* F814W optical image (Figure 3). This association or cluster of stars could either be a tidal dwarf galaxy (if it is a bound structure) that is unresolved in the HI kinematics from Hibbard & Yun (1999) or is possibly a large (super?) star cluster in the disk of IC 694 or externally formed out of tidally stripped material. This feature has a higher redshifted Hα velocity (Figure 4) which is slightly higher than the velocity seen in the HI tidal tail that extends linearly outward from this region. The Hα derived SFR of this stellar cluster in an 11″ aperture is 0.029±0.001 $M_\odot$ $yr^{-1}$and it has an HI gas surface density of 40.2±9$M_\odot$ pc^{-2}.

7.3. SFR–Gas Surface Density Relation in Nuclear Regions

Measurements of the relations between SFRs and gas surface densities in starburst galaxies have been measured globally, most notably by Kennicutt (1998), however little work has been done to explore this relation on smaller spatial scales compared to the extensive work done by Bigiel et al. (2008); VENGA (Blanc et al. , in prep.) ref here? and others on non–interacting normal spiral and dwarf galaxies. In order to investigate this relation in the nuclear regions of the nearby Arp 299 merger, we use the SFR and gas surface densities from Sections 5 and 3.2 to look at the SFR–Gas surface density relation in the nuclear regions on 1.3 kpc (6″) size apertures. Figures 16 and 17 show the interpolated Hα flux map with the CO$J = 2 \rightarrow 1$ (blue) and CO$J = 3 \rightarrow 2$ (white) and HCN$J = 1 \rightarrow 0$ (cyan) and $HCO^+J = 1 \rightarrow 0$ (white) contours overlaid, respectively. In Figure 18 shows the SFR–Mol gas relations for each nuclear region using molecular gas traced by CO$J = 2 \rightarrow 1$ (yellow points) and CO$J = 3 \rightarrow 2$ (orange points). We compare to SFR-gas relations on disk-averaged scales for spirals and starbursts using a combination of HI+CO gas (Kennicutt 1998), using molecular gas as traced by CO only in high–z mergers (Daddi et al. 2010) and in 1 kpc regions in spirals and dwarf galaxies (Bigiel et al. 2011). The solid lines indicate the parameter space of the SFR-gas relation fit of Kennicutt (1998) and the dashed lines are

extrapolations. Another caveat is that each of these relations uses a different SFR tracer: Hα (normal spirals) and IR (IR bright starbursts) (Kennicutt 1998), Hα and FUV+24μm (spirals), IR (starbursts/SMGs), and UV (BZKs/normal disks) (Daddi et al. 2010), and a combined *GALEX* far–UV (FUV) +24μm (Bigiel et al. 2011)). The nuclear regions lie on the relation for high–z mergers within the errors in $\Sigma_{\rm Mol}$ which is mainly due to the $\alpha_{\rm CO}$ chosen for Arp 299. In Figure 19 we show the SFR–Dense gas relation as traced by HCN$J = 1 \rightarrow 0$ (cyan points) and HCO$^{+}J = 1 \rightarrow 0$ (purple points). The HCN$J = 1 \rightarrow 0$ measurements for regions B1, C, and C$'$ are upper limits denoted by arrows. The yellow line indicates the SFR–Dense gas relation converted to surface densities using $\alpha_{\rm Dense}$= 10 and HCN$J = 1 \rightarrow 0$ integrated intensities for spirals and (U)LIRGs using dense gas as traced by HCN$J = 1 \rightarrow 0$ from Gao & Solomon (2004b) and black horizonal lines indicate the region of parameter space. Other than the upper limits, the nuclear regions lie close to the Gao & Solomon (2004b) SFR–Dense gas relation within the errors despite changing $\alpha_{\rm Dense}$ to 5 for Arp 299. Changing the $\alpha_{\rm Dense}$ to 5 in the Gao & Solomon (2004b) relation would shift the relation to the left in alignment with regions B1, C and C$'$, but farther away from the starburst nucleus A.

7.4. Spatially Resolved SFR–Gas Surface Density Relation

We show the spatially resolved SFR–gas surface density on 1.3 kpc scales in regions covered by the CO$J = 2 \rightarrow 1$ (blue) and CO$J = 3 \rightarrow 2$ maps in Figure 20 and 21 (yellow stars). Also shown are regions that may be affected by the AGN in NGC 3690 or by a starburst superwind (Section 6) as seen in line ratios from our IFU fiber measurements (stars, squares) as well as regions near the X-ray centroid (crosses). The depletion timescale ($\tau_{\rm dep}$) which is the inverse of the star formation efficiency (SFE) as defined by the SFR per unit gas mass or the $\Sigma_{\rm SFR}/\Sigma_{\rm Mol}$ (yr^{-1}) is indicated by the dotted diagonal lines. These regions lie mainly outside of the nuclear regions at low $\Sigma_{\rm Mol}$ or areas not covered by the CO maps, but there are a a few regions with CO measurements that lie near the other points within the scatter. The SFR–Mol gas relations for disk–average measurement sof non-interacting galaxies are also shown (Kennicutt 1998; Daddi et al. 2010; Bigiel et al. 2011). We find that regions in both CO$J = 2 \rightarrow 1$ and CO$J = 3 \rightarrow 2$ transitions lie above the high–z merger relation from Daddi et al. (2010), which is likely due to the low value of $\alpha_{\rm CO}$ used (Section 3.2), but was calculated directly for Arp 299 (Papadopoulos et al. 2012; Sliwa et al. 2012), however see Section 7.6.1. The Spearman rank correlation coefficient is 0.88 and 0.71 for CO$J = 2 \rightarrow 1$ and CO$J = 3 \rightarrow 2$, respectively, indicating a strong correlation between $\Sigma_{\rm Mol}$ and $\Sigma_{\rm SFR\ [H\alpha+24\mu m]}$ in both transitions. The integrated $\Sigma_{\rm Mol}$ and $\Sigma_{\rm SFR\ [H\alpha+24\mu m]}$ is also shown in both figures and are seen to lie on or near the Daddi et al. (2010) SFR–Mol

relation.

7.5. Spatially Resolved SFR–Dense Gas Surface Density Relation

Gao & Solomon (2004b) found the SFR–Dense gas relation to be a tighter linear relation in both non-interacting normal spiral galaxies and (U)LIRGs using the IRAS IR SFRs and the HCN$J = 1 \rightarrow 0$ line then the relation found using CO on *global* or disk-average scales. Since Arp 299 is a nearby IR bright merger, does this tight linear relation still hold on scales of 1.3 kpc? In Figure 22, we show the SFR–Dense gas relation for $\Sigma_{\rm SFR\ [H\alpha+24\mu m]}$ and $\Sigma_{\rm Dense}$ as traced by HCN$J = 1 \rightarrow 0$ and HCO$^+J = 1 \rightarrow 0$. Also shown is the relation from Gao & Solomon (2004b) converted to $\Sigma_{\rm Dense}$ using and $\alpha_{\rm Dense}$ of 10 (yellow solid line) and the dashed line is an extrapolation and $\tau_{\rm dep}$ are the dotted diagonal lines. We also show the integrated values for HCN$J = 1 \rightarrow 0$ (cyan)and HCO$^+J = 1 \rightarrow 0$ (purple) as large stars. The integrated values for both dense gas tracers line up remarkably well with the Gao & Solomon (2004b) SFR–Dense gas relation with the only offset being the choice of $\alpha_{\rm Dense}$ where we used $\alpha_{\rm Dense}$of 5 for Arp 299. If we use an $\alpha_{\rm Dense}$ of 10, this would shift the integrated points to lie on the Gao & Solomon (2004b) relation. The spatially resolved points (small cyan and purple stars) lie along the same line as the integrated values and have Spearman correlation coefficients of 0.68 and 0.83 for HCN$J = 1 \rightarrow 0$ and HCO$^+J = 1 \rightarrow 0$, respectively, indicating there is a strong relation between $\Sigma_{\rm SFR\ [H\alpha+24\mu m]}$ and $\Sigma_{\rm Dense}$ for both dense gas tracers. Although the displacement between our points and the Gao & Solomon (2004b) relation is likely due to the choice of $\alpha_{\rm Dense}$, the difference in the SFR tracer (SFR$_{\rm [H\alpha+24\mu m]}$versus SFR from IRAS) or the spatial scales measured (global scales compared to 1.3 kpc scales) might also contribute to the offset.

7.6. Spatially Resolved SFR–HI Gas Surface Density Relation

Since we find that the SFR$_{\rm [H\alpha]}$ recovers the SFR$_{\rm [H\alpha+24\mu m]}$ within a factor of ∼2-3 (Section 7.2), we can use it to reliably estimate the SFR–gas relation using HI as a gas tracer in the outer regions of the Arp 299 merger. We are limited to the resolution of the HI map $\sim$22″ and we make measurements in 11 apertures on scales of the HI resolution of 4.7 kpc. In Figure 23 we show the interpolated Hα flux map with the HI contours overlaid in red as well as X-ray AGN contaminated regions (crosses) and IFU AGN regions (white stars). As discussed in Section 7.2, the HI peak emission is associated with a region that has bright Hα flux and a stellar cluster as seen in the *HST* optical image. We convolve our IFU Hα map with a Gaussian beam of 22″ FWHM to match the HI map resolution. We compare our

measurements to the data points from the outer disks of normal spiral and dwarf galaxies from Bigiel et al. (2010) on spatial scales of 15″ or ∼0.6-1 kpc at the distance of their sample galaxies. One caveat is that Bigiel et al. (2010) estimate the SFR using the *GALEX* FUV as a tracer which uses a slightly different normalization that the SFRs we derive using relations from Murphy et al. (2011). Their measurements are normalized to the same Kroupa (2001) IMF, however the normalization they use from Salim et al. (2007) is a factor of 1.3 lower than that derived in Murphy et al. (2011) different from the SFR calibration they used. We therefore multiply their SFRs by this factor in order to directly compare to our measurements and this distribution for normal spirals (orange points) and dwarf galaxies (purple points) is shown in Figure 24. We also include a factor of 1.37 to account for helium in their measurements of $\Sigma_{\rm HI}$. Another caveat is that their spatial scales are a factor of ∼5-8 lower than the regions we measure in Arp 299.

Figure 24 shows the SFR–HI extranuclear relation (yellow stars) as well as the range of normal spiral and starburst galaxies from Kennicutt (1998) and $\tau_{\rm dep}$ (where $\tau_{\rm dep}$=1/SFE) are the dotted diagonal lines. The Spearmans correlation coefficient for the 11 regions in Arp 299 is 0.15 which indicates a weak correlation that can be attributed to the wide scatter in data points. However, we do find points that are likely associated with the disk of IC 694 to lie along the same relation as the outer disks of normal spiral and dwarf galaxies. We also find there to be points that lie above the distribution of spirals and dwarfs. Since we area measuring points in the outer region of the Arp 299 merger, the star formation could be coming from a different physical process than that seen in the nuclear regions (i.e., gas driven inflow of dense material collapsing to form stars). Extranuclear star formation in galaxy mergers could be driven by turbulence due to the high velocity dispersion in the gas which can either support clouds against gravitational collapse or turbulent flows can compress the gas to form dense clumps and drive star formation (Elmegreen 2002). These processes may explain the difference in SFR–gas relations at high-z (Genzel et al. 2010; Daddi et al. 2010) and in nearby spirals and starbursts on global scales (Kennicutt 1998) as seen in numerical simulations (Teyssier et al. 2010). The SFR–HI relation seen in 4.7 kpc regions in the Arp 299 merger follow the same trends with the exception of a few points. On average, the SFE as defined by the SFR per unit gas mass or the $\Sigma_{\rm SFR}/\Sigma_{\rm HI}$ ($\rm yr^{-1}$) is found to be higher by a factor of ∼6 than the sample of normal spiral galaxies. The increase in SFE may be due to turbulent motions, but the increase is not extreme as it is likely the extranuclear star formation in Arp 299 is being driven by molecular cloud collapse at a lower rate than the nuclear regions. There could be significant deviation from this relation, for example, in interacting galaxies at different interaction phases which is something that we will test with the VIXENS sample of interacting galaxies (Heiderman et al. 2011).

7.6.1. Variation of CO–to–H_2 Conversion Factor with Metallicity, IRAS F_{60}/F_{100} Flux Ratio, and Dust Temperature

Since it is unlikely that there is only a single CO–to–H_2 conversion factor in any given galaxy, we investigate the variation of the CO–to–H_2 conversion factor ($\alpha_{\rm CO}$) on small scales in the Arp 299 system as a function of metallicity and compare to the commonly assumed starburst (Downes & Solomon 1998) and Galactic (Bloemen et al. 1986) conversion factors. We use the model proposed by Narayanan et al. (2012) for the conversion factor ($\alpha_{\rm CO}({\rm Z}')$) as a function of metallicity normalized by the solar value (Z′) described by the equation:

$$\alpha_{\rm CO}({\rm Z}') = 10.7 \times \left(\frac{\langle I({\rm CO})\rangle^{-0.32}}{\rm K\ km\ s^{-1}}\right) \times \left(\frac{1}{{\rm Z}'^{0.65}}\right)\ (M_\odot\ {\rm pc}^{-2}\ ({\rm K\ km\ s^{-1}})^{-1}). \qquad (12)$$

The N2 metallicity calibration from Pettini & Pagel (2004) which uses the [NII]/Hα strong line ratio was used to determine metallicities assuming a solar metallicity of 12 + log(O/H) = 8.69±0.05 (Asplund et al. 2009). Figure 25 shows the fiber–to–fiber distribution of metallicities across the merger. The mean metallicity of Arp 299 is 8.57±0.01. We find higher metallicities in the outer regions of the merger and lower or diluted metallicities in the nuclear regions in agreement with merger scenario in which galaxy interactions drive lower metallicity gas from the outer regions of the system into the central regions (Kewley et al. 2010 and references therein).

Using the relationship between metallicity and integrated CO line intensity from Narayanan et al. (2012), we explore the variation in $\alpha_{\rm CO}({\rm Z}')$ on a 6″ or 1.3 kpc spatial scale **(results do not vary on fiber size scales)** to compare later with our Hα + 24μm based SFRs. To measure over 1.3 kpc apertures, we use our fiber–to–fiber metallicity measurements and make an interpolated 2–D metallicity map and convolve this with a Gaussian kernel with a 6″ FWHM. Figure 26 shows the distribution of $\alpha_{\rm CO}({\rm Z}')$ for both CO$J = 1 \rightarrow 0$ and CO$J = 3 \rightarrow 2$ integrated line intensities converted to CO$J = 1 \rightarrow 0$ using the line ratios in Section 3.2 on and 6″ scales. We find that $\alpha_{\rm CO}({\rm Z}')$ varies based on which CO line transition is used to make the measurement. The median $\alpha_{\rm CO}({\rm Z}')$ using CO$J = 2 \rightarrow 1$ integrated intensities is 3.6±0.2 $M_\odot$ pc^{-2} (K km s^{-1})$^{-1}$ and using the CO$J = 3 \rightarrow 2$ line intensity it is 3.2±0.1 $M_\odot$ pc^{-2} (K km s^{-1})$^{-1}$ on 1.3 kpc scales. The difference between CO$J = 2 \rightarrow 1$ and CO$J = 3 \rightarrow 2$ is likely due to the cloud filling factor with CO$J = 2 \rightarrow 1$ emission being more extended and CO$J = 3 \rightarrow 2$ emission being more compact (see Figure 16). Overall on average, the $\alpha_{\rm CO}({\rm Z}')$ factors agree well with the commonly used Galactic conversion factor of 4.5 $M_\odot$ pc^{-2}(K km s^{-1})$^{-1}$ (Bloemen et al. 1986) rather than the commonly used starburst factor (Downes & Solomon 1998) and $\alpha_{\rm CO}$ calculated using this relation. We find little variation in metallicity across Arp 299 so the values obtained for $\alpha_{\rm CO}$ are dominated by the variation in integrated line intensity for both CO transitions in these regions.

We explore the SFR–gas surface density relations using the varying $\alpha_{\rm CO}$(Z′) factor in Figures 27 and 28 which show the SFR–Mol surface density relations on 1.3 kpc using $\alpha_{\rm CO}$(Z′) and a factor of 1.37 for helium to convert from H_2 to total molecular gas surface densities. We find using $\alpha_{\rm CO}$(Z′) does lower the dispersion in the SFR–Mol relations compared to what we found using just a single conversion factor (Figures 20 and 21) and since higher $\alpha_{\rm CO}$ values were found using the metallicity–CO line intensity relation, the points move to the right in gas surface density.

An alternative method to determine $\alpha_{\rm CO}$ is to use a measurement of the dust content. Assuming a dust emissivity spectral index $\beta = 1.5$ and the ratio of F_{60}/F_{100} IRAS fluxes from Table 2, we calculate a dust temperature ($T_{\rm dust}$) of 42.5 K. Using the linear relations between the IRAS flux ratio and CO–to–H_2 conversion factor (F_{60}/F_{100}–$\alpha_{\rm CO}$) and our derived dust temperature and conversion factor ($T_{\rm dust}$–$\alpha_{\rm CO}$) from Magnelli et al. (2012) (their Table 4), we obtain a values of 0.67 and 0.99 $M_\odot$ pc^{-2}(km s^{-1})$^{-1}$. These values lie in between the $\alpha_{\rm CO}$ from Sliwa et al. (2012) and Papadopoulos et al. (2012) for Arp 299 and our results using the metallicity–CO line intensity relation from Narayanan et al. (2012). This indicates that a higher Milky Way like value for $\alpha_{\rm CO}$ may be more suitable for Arp 299 than the two lower values previously found. Another possibility is that $\alpha_{\rm CO}$ likely varies as a function of interaction phase based on if the system is in starburst mode and therefore a bimodal $\alpha_{\rm CO}$ (eg., starburst or Galactic) is highly unlikely (Tacconi et al. 2008). In order to better understand these relations and conversion factors $\alpha_{\rm CO}$ and $\alpha_{\rm Dense}$ in more detail as a function of interacting phase in nearby galaxy mergers, obtaining molecular gas maps with more coverage and higher sensitivity and resolution from facilities such as ALMA would be highly beneficial.

8. Summary

We investigate relations between the SFR and gas surface densities using a variety of star formation and gas tracers in the nearby IR bright galaxy merger Arp 299. We use an IFU Hα map from the VIXENS survey of interacting galaxies, archival 24μm and *HST* Paα, to derive SFR surface densities and use maps of molecular gas from CO$J = 2 \rightarrow 1$ and CO$J = 3 \rightarrow 2$, dense gas from HCN$J = 1 \rightarrow 0$ and HCO$^+$ $J = 1 \rightarrow 0$, and atomic gas from HI to compute gas surface densities.

Our results are as follows:

1. We compare two Galactic extinction laws from Draine (2003) using R_V= 3.1 (diffuse ISM) and R_V= 5.5 (molecular clouds), using the Balmer decrement Hα/Hβ flux ratio

from our IFU data and from the Hα/Paα/ flux ratio from the IFU Hα map and an *HST* NICMOS Paα map. We find that the R_V= 5.5 extinction law yields a higher Hα/Paα ratio then using R_V= 3.1 in the nuclear regions of Arp 299, however the ratio is still a factor of ∼2 below the intrinsic Paα/Ha ratio from recombination line theory indicating that neither the Hα or Paα line reliably trace all of the star formation (Section 4). Comparing the A_V from the Hα/Hβ/ (∼0.7-1.3 mag)and Hα/Paα (∼1.4-2.3) we find A_V both flux ratios are much lower by a factor of ∼10 than those found using CO maps (∼7-29 mag).

2. Using BPT line diagnostic diagrams, we find no evidence for an AGN in either of the two nuclear regions A and B1 (Section 6). Two regions are selected as AGN by all three BPT diagrams that lie near the nuclear region of B1 similar to that reported in García-Marín et al. (2006) which could be a Seyfert-like ionization cone, however it could also be a interstellar gas heated by photoionization by massive stars. We also find high [OI]/Hα and [SII]/Hα line ratios covering a large area outside the nuclear regions which can be attributed to either a large population of Wolf-Rayet stars or supernova driving a starburst superwind shocked outflow of gas.

3. SFR tracers are calibrated using a common IMF (Murphy et al. 2011) are used to compare the global or system-averaged SFR for different tracers. We find the $SFR_{[H\alpha+24\mu m]}$ (90±10 $M_\odot$ yr^{-1}) is in agreement with the total IR SFR from IRAS (77±5 $M_\odot$ yr^{-1}), while the $SFR_{[H\alpha]}$ (19±1) and $SFR_{[24\mu m]}$ (44±6) underestimate the total SFR by factors of ∼4 and 2, respectively (Section 7.1). The total nuclear $SFR_{[Pa\alpha]}$ is $\gtrsim$13±3 is similar to the *total* $SFR_{[H\alpha]}$, which is due to the high extinction in both the Paα and Hα line fluxes. The $SFR_{[Pa\alpha]}$ in 6″ apertures centered on the peak Paα emission are a factor of ∼ 2 lower on average than the $SFR_{[H\alpha+24\mu m]}$.

4. We compare $SFR_{[H\alpha]}$ to $SFR_{[H\alpha+24\mu m]}$ on a region-by-region basis to see the extent to which using Hα to trace star formation in a nearby galaxy merger is limited. We find a mostly non-linear relation between $SFR_{[H\alpha]}$ and $SFR_{[H\alpha+24\mu m]}$ which demonstrates that the $SFR_{[H\alpha]}$ underestimates the true SFR by at least a factor of ∼10 on average but ranges from 1-60 (Section 7.2). The reliability of Hα as a tracer of star formation in Arp 299 is tested and we find that regions near the C-C′ complex, as well as regions to the north and northwest of the nuclei have a similar $SFR_{[H\alpha]}$ and $SFR_{[H\alpha+24\mu m]}$ within factor of ∼1-3. Hα recovers the true SFR outside the nuclei and in the interface region of Arp 299.

5. The nucleus of NGC 3690, region B1, has the highest SFR surface density when a 24μm SFR tracer is used and star forming complex region C has the highest $\Sigma_{SFR\ [H\alpha]}$ followed by IC 694 nucleus (region A), B1 and C′ (Section 7.2). The low hydrogen

recombination line SFR surface density in region A is likely due to the high level of extinction in Hα and Paα (Section 4).

6. The northwest region of Arp 299 has an Hα peak associated the HI peak and a stellar cluster seen in the *HST* F814W optical image, which could either be a tidal dwarf galaxy or possible a large cluster in the disk of IC 694 or external cluster formed out of tidally stripped material (Section 7.2).

7. We explore the SFR-Mol relation between the SFR using $SFR_{[H\alpha+24\mu m]}$ and molecular gas surface densities in the nuclear regions of Arp 299 using CO$J = 2 \rightarrow 1$ and CO$J = 3 \rightarrow 2$ converted to CO$J = 1 \rightarrow 0$ using a line ratio. We also look at the SFR-dense gas surface density relation using HCN$J = 1 \rightarrow 0$ and $HCO^+ J = 1 \rightarrow 0$ lines as dense gas tracers. We find the nuclear regions to lie on the SFR-Mol surface density relation found in high-z mergers (Daddi et al. 2010) and on the SFR-dense gas relation of Gao & Solomon (2004b) within the errors (Section 7.3).

8. Spatially resolved regions of size 1.3 kpc throughout the Arp 299 merger using CO$J = 2 \rightarrow 1$ and CO$J = 3 \rightarrow 2$ are strongly correlated in $\Sigma_{SFR\ [H\alpha+24\mu m]}$ and Σ_{Mol} and are found to lie above the Daddi et al. (2010) high-z merger relation in the SFR-Mol gas surface density plane while the integrated SFR-Mol surface densities lie on the (Daddi et al. 2010) relation (Section 7.4). The discrepancy is likely due to the lower α_{CO} chosen for Arp 299 or a combination of that and the choice in SFR tracer and spatial scale measured.

9. The SFR–Dense gas relations on 1.3 kpc scales in Arp 299 using $\Sigma_{SFR\ [H\alpha+24\mu m]}$ and HCN$J = 1 \rightarrow 0$ and $HCO^+ J = 1 \rightarrow 0$ to trace Σ_{Dense} are strongly correlated and lie along the same line as the integrated values for Arp 299 (Section 7.5). Both the integrated and spatially resolved points lie above the Gao & Solomon (2004b) relation with the differences being the choice of α_{Dense} for Arp 299 of 5 and α_{Dense} of 10 used in that study, the SFR tracer ($SFR_{[H\alpha+24\mu m]}$versus SFR from IRAS), or comparing different spatial scales.

10. Since $SFR_{[H\alpha]}$ recovers $SFR_{[H\alpha+24\mu m]}$ within a factor of ∼2-3 (Section 7.2), we use it to investigate the SFR–HI gas surface density relation in the extranuclear regions of Arp 299 on 4.7 kpc scales. We compare SFR–HI surface density relation in Arp 299 to a sample of spiral and dwarf galaxies from Bigiel et al. (2010) and find that regions in Arp 299 seem to follow the same general trend as in the outer disks of normal spirals and dwarfs with the exception of a few points that have higher SFR surface densities (Section **??**). The SFE of regions in Arp 299 are higher by a factor of ∼6 compared to spirals and dwarfs and this could be due to the effects of a high velocity dispersion in

interacting galaxies driving star formation, however the increase in SFE is not extreme and star formation is likely driven by molecular cloud collapse at a lower rate then in the nuclear regions.

11. We use the [NII]/Hα strong line ratio was used to determine metallicities and find the mean metallicity of Arp 299 to be 12+ log(O/H) of 8.57±0.01 (Section 7.6.1). Higher metallicities are found in the outer regions of Arp 299 and lower or diluted metallicities in the nuclear regions in agreement with merger scenario in which galaxy interactions drive lower metallicity gas from the outer regions of the system into the central regions (Kewley et al. 2010 and references therein).

12. A large uncertainty in calculating $\Sigma_{\rm Mol}$ is the CO–to–H_2 conversion factor, $\alpha_{\rm CO}$. We explore the variation of $\alpha_{\rm CO}$ as a function of metallicity IRAS 60 to 100μm flux ratio, and dust temperature. We use the relation from Narayanan et al. (2012) to compute $\alpha_{\rm CO}({\rm Z}')$ as well as the F_{60}/F_{100}–$\alpha_{\rm CO}$ and $T_{\rm dust}$–$\alpha_{\rm CO}$ from Magnelli et al. (2012) (Section 7.6.1). We find $\alpha_{\rm CO}$ varies based on CO line transition used with a median value for CO$J = 2 \rightarrow 1$ of 3.2 $M_\odot$ pc^{-2}(K km s^{-1})$^{-1}$ to 3.6 using CO$J = 3 \rightarrow 2$ $M_\odot$ pc^{-2}(K km s^{-1})$^{-1}$ and the variation in $\alpha_{\rm CO}$ is dominated by the lower I(CO) line intensities (Section **??**). Both values are closer to the commonly used Galactic value of 4.5 $M_\odot$ pc^{-2}(K km s^{-1})$^{-1}$ (Bloemen et al. 1986) as opposed to the common starburst conversion factor of 0.8 $M_\odot$ pc^{-2}(K km s^{-1})$^{-1}$ (Downes & Solomon 1998) and the value previously found for Arp 299 of ∼0.4 $M_\odot$ pc^{-2}(K km s^{-1})$^{-1}$. The SFR–Mol relation using $\alpha_{\rm CO}({\rm Z}')$ lowers the dispersion in the relations compared to a single conversion factor and moves the points to the right in $\Sigma_{\rm Mol}$ in between the Daddi et al. (2010) and Kennicutt (1998) relations. The conversion factor using F_{60}/F_{100} and $T_{\rm dust}$ for Arp 299 are 0.67 and 0.99 $M_\odot$ pc^{-2}(K km s^{-1})$^{-1}$, respectively. A higher Milky Way value of $\alpha_{\rm CO}$ for late interaction phase merger, Arp 299, may be more suitable than the lower values previously found. The other possibility is that $\alpha_{\rm CO}$ likely varies as a function of interaction phase based on whether the system is in starburst mode and region by region in interacting galaxies.

The authors thank Daniela Calzetti, X, Y, and Z for informative discussions. A.H., N.J.E., and K.G. acknowledge support for this work from grant XX, YY.... G.B., T.A.D, C.P., R.V., D.I., and M.Y. acknowledge support from .....**please email individual acknowledgments for this section to A.H.**

SDSS-III is managed by the Astrophysical Research Consortium for the Participating Institutions of the SDSS-III Collaboration including the University of Arizona, the Brazilian

Participation Group, Brookhaven National Laboratory, University of Cambridge, Carnegie Mellon University, University of Florida, the French Participation Group, the German Participation Group, Harvard University, the Instituto de Astrofisica de Canarias, the Michigan State/Notre Dame/JINA Participation Group, Johns Hopkins University, Lawrence Berkeley National Laboratory, Max Planck Institute for Astrophysics, Max Planck Institute for Extraterrestrial Physics, New Mexico State University, New York University, Ohio State University, Pennsylvania State University, University of Portsmouth, Princeton University, the Spanish Participation Group, University of Tokyo, University of Utah, Vanderbilt University, University of Virginia, University of Washington, and Yale University.

REFERENCES

Aalto, S., Radford, S. J. E., Scoville, N. Z., & Sargent, A. I. 1997, ApJL, 475, L107

Adams, J. J., Blanc, G. A., Hill, G. J., et al. 2011, ApJS, 192, 5

Alonso-Herrero, A., Rieke, G. H., Rieke, M. J., & Scoville, N. Z. 2000, ApJ, 532, 845

Asplund, M., Grevesse, N., Sauval, A. J., & Scott, P. 2009, ARAA, 47, 481

Baan, W. A., & Haschick, A. 1990, ApJ, 364, 65

Baldwin, A., Phillips, M. M., & Terlevich, R. 1981, PASP, 93, 817

Ballo, L., Braito, V., Della Ceca, R., et al. 2004, ApJ, 600, 634

Bigiel, F., Leroy, A., Walter, F., et al. 2010, AJ, 140, 1194

—. 2008, AJ, 136, 2846

Bigiel, F., Leroy, A. K., Walter, F., et al. 2011, ApJL, 730, L13

Bloemen, J. B. G. M., Strong, A. W., Mayer-Hasselwander, H. A., et al. 1986, A&A, 154, 25

Bournaud, F., Elmegreen, B. G., Teyssier, R., Block, D. L., & Puerari, I. 2010, MNRAS, 409, 1088

Calzetti, D., Armus, L., Bohlin, R. C., et al. 2000, ApJ, 533, 682

Cappellari, M., & Emsellem, E. 2004, PASP, 116, 138

Casoli, F., Willaime, M.-C., Viallefond, F., & Gerin, M. 1999, A&A, 346, 663

Coziol, R., Torres, C. A. O., Quast, G. R., Contini, T., & Davoust, E. 1998, ApJS, 119, 239

Daddi, E., Elbaz, D., Walter, F., et al. 2010, ApJL, 714, L118

Della Ceca, R., Ballo, L., Tavecchio, F., et al. 2002, ApJL, 581, L9

Dopita, M. A., & Sutherland, R. S. 1995, ApJ, 455, 468

Downes, D., & Solomon, P. M. 1998, ApJ, 507, 615

Draine, B. T. 2003, ARAA, 41, 241

Elmegreen, B. G. 2002, ApJ, 577, 206

Evans, II, N. J. 1999, ARAA, 37, 311

Falcón-Barroso, J., Sánchez-Blázquez, P., Vazdekis, A., et al. 2011, A&A, 532, A95

Gallais, P., Charmandaris, V., Le Floc'h, E., et al. 2004, A&A, 414, 845

Gao, Y., & Solomon, P. M. 2004a, ApJS, 152, 63

—. 2004b, ApJ, 606, 271

García-Burillo, S., Usero, A., Alonso-Herrero, A., et al. 2012, A&A, 539, A8

García-Marín, M., Colina, L., Arribas, S., Alonso-Herrero, A., & Mediavilla, E. 2006, ApJ, 650, 850

Gehrz, R. D., Sramek, R. A., & Weedman, D. W. 1983, ApJ, 267, 551

Genzel, R., Tacconi, L. J., Gracia-Carpio, J., et al. 2010, MNRAS, 407, 2091

Graciá-Carpio, J., García-Burillo, S., Planesas, P., & Colina, L. 2006, ApJL, 640, L135

Heckman, T. M., Armus, L., Weaver, K. A., & Wang, J. 1999, ApJ, 517, 130

Heiderman, A., Evans, II, N. J., Allen, L. E., Huard, T., & Heyer, M. 2010, ApJ, 723, 1019

Heiderman, A. L., Evans, II, N. J., Gebhardt, K., et al. 2011, in New Horizons in Astronomy, Proceedings of the Frank N. Bash Symposium 2011, held October 9-11, 2011. Austin, Texas, USA. Edited by S. Salviander, J. Green, and A. Pawlik. Published online at http: //pos.sissa.it/cgi-bin/reader/conf.cgi?confid=149., id.29

Helou, G. 1986, ApJL, 311, L33

Hibbard, J. E., & Yun, M. S. 1999, AJ, 118, 162

Ho, L. C., Filippenko, A. V., & Sargent, W. L. W. 1997, ApJS, 112, 315

Imanishi, M., & Nakanishi, K. 2006, PASJ, 58, 813

Juneau, S., Narayanan, D. T., Moustakas, J., et al. 2009, ApJ, 707, 1217

Kauffmann, G., Heckman, T. M., Tremonti, C., et al. 2003, MNRAS, 346, 1055

Kennicutt, R. C., & Evans, N. J. 2012, ARAA, 50, 531

Kennicutt, Jr., R. C. 1998, ApJ, 498, 541

Kewley, L. J., Dopita, M. A., Sutherland, R. S., Heisler, C. A., & Trevena, J. 2001, ApJ, 556, 121

Kewley, L. J., Groves, B., Kauffmann, G., & Heckman, T. 2006, MNRAS, 372, 961

Kewley, L. J., Rupke, D., Zahid, H. J., Geller, M. J., & Barton, E. J. 2010, ApJL, 721, L48

Kroupa, P. 2001, MNRAS, 322, 231

Le Floc'h, E., Papovich, C., Dole, H., et al. 2005, ApJ, 632, 169

Magnelli, B., Saintonge, A., Lutz, D., et al. 2012, ArXiv e-prints

Massey, P., Strobel, K., Barnes, J. V., & Anderson, E. 1988, ApJ, 328, 315

Mihos, J. C., & Hernquist, L. 1996, ApJ, 464, 641

Murphy, E. J., Condon, J. J., Schinnerer, E., et al. 2011, ApJ, 737, 67

Narayanan, D., Krumholz, M. R., Ostriker, E. C., & Hernquist, L. 2012, MNRAS, 421, 3127

Neff, S. G., Ulvestad, J. S., & Teng, S. H. 2004, ApJ, 611, 186

Osterbrock, D. E., & Ferland, G. J. 2006, Astrophysics of gaseous nebulae and active galactic nuclei

Papadopoulos, P. P., van der Werf, P., Xilouris, E., Isaak, K. G., & Gao, Y. 2012, ApJ, 751, 10

Pettini, M., & Pagel, B. E. J. 2004, MNRAS, 348, L59

Rahman, N., Bolatto, A. D., Xue, R., et al. 2012, ApJ, 745, 183

Reiter, M., Shirley, Y. L., Wu, J., et al. 2011, ApJS, 195, 1

Roy, A. L., Goss, W. M., & Anantharamaiah, K. R. 2008, A&A, 483, 79

Salim, S., Rich, R. M., Charlot, S., et al. 2007, ApJS, 173, 267

Sánchez-Blázquez, P., Peletier, R. F., Jiménez-Vicente, J., et al. 2006, MNRAS, 371, 703

Sanders, D. B., & Mirabel, I. F. 1996, ARAA, 34, 749

Sarzi, M., Falcón-Barroso, J., Davies, R. L., et al. 2006, MNRAS, 366, 1151

Schmidt, M. 1959, ApJ, 129, 243

Sliwa, K., Wilson, C. D., Petitpas, G. R., et al. 2012, ApJ, 753, 46

Stanford, S. A., & Wood, D. O. S. 1989, ApJ, 346, 712

Tacconi, L. J., Genzel, R., Smail, I., et al. 2008, ApJ, 680, 246

Teyssier, R., Chapon, D., & Bournaud, F. 2010, ApJL, 720, L149

van Dokkum, P. G. 2001, PASP, 113, 1420

Wilson, C. D., Petitpas, G. R., Iono, D., et al. 2008, ApJS, 178, 189

Wu, J., Evans, N. J., Shirley, Y. L., & Knez, C. 2010, ApJS, 188, 313

Wu, J., Evans, II, N. J., Gao, Y., et al. 2005, ApJL, 635, L173

Zezas, A., Ward, M. J., & Murray, S. S. 2003, ApJL, 594, L31

Table 1. Star formation and Gas Surface Densities in Regions A, B1, C, and C′

Region Name (1)	Σ [H$_\alpha$] (2)	Σ [24μm] (3)	Σ [H$_\alpha$+24μm] (4)	Σ [Pa$_\alpha$] (5)	$\Sigma_{\rm Mol}$ [CO(2–1)] (6)	$\Sigma_{\rm Mol}$ [CO(3–2)] (7)	$\Sigma_{\rm Dense}$ [HCN(1–0)] (8)	$\Sigma_{\rm Dense}$ [HCO$^+$(1–0)] (9)
4″.235 apertures[a]								
A	1.66 ± 0.003	-	-	3.79 ± 3.6	460.8 ± 346	560.7 ± 423	289.0 ± 147	357.9 ± 183
B1	1.56 ± 0.003	-	-	2.16 ± 2.6	170.8 ± 128	209.7 ± 158	<11.2 ± 5	122.9 ± 62
C	2.65 ± 0.003	-	-	3.90[b] ± 3.5	126.0 ± 94	100.0 ± 75	<21.0 ± 10	107.6 ± 54
C′	1.34 ± 0.002	-	-	-	110.3 ± 82	118.6 ± 89	<32.5 ± 16	83.6 ± 42
6″ apertures								
A	0.68 ± 0.001	2.6 ± 0.10	3.0 ± 0.06	2.42±2.0	303.6 ± 228	347.3 ± 262	213.5 ± 109	275.6 ± 143
B1	0.60 ± 0.001	4.2 ± 0.12	5.0 ± 0.07	1.56±1.5	113.0 ± 84	132.7 ± 100	<9.1 ± 4	93.6 ± 47
C	1.00 ± 0.001	2.9 ± 0.10	3.6 ± 0.06	2.95±2.3	92.4 ± 69	66.9 ± 50	<18.1 ± 9	94.9 ± 48
C′	0.62 ± 0.001	2.3 ± 0.09	2.7 ± 0.06	-	86.3 ± 64	93.8 ± 70	<28.6 ± 14	83.1 ± 42

Note. — (a) Measurements on fiber size scales are restricted to only the Hα and Paα map due to the limitation placed by the 24μm PSF; (b) Paα SFR measured for the C–C′ complex at the Paα peak.;(1) Region name using source coordinates from Neff et al. (2004) their Table 3; (2)–(5): SFR surface densities in units of $M_\odot$ yr^{-1} kpc^{-2}; (3)–(8): $\Sigma_{\rm Mol}$ or $\Sigma_{\rm Dense}$ gas surface densities in units of M$_\odot$ pc^{-2} using values of $\alpha_{\rm CO}$= 0.4 and $\alpha_{\rm Dense}$= 5 M$_\odot$ pc^{-2} (K km s^{-1})$^{-1}$, respectively. The 4″.235 apertures can only be used to measure Paα SFRs reliably as the 6″ apertures lie outside of the FoV of the Paα images. See Sections 3.2 and 5.

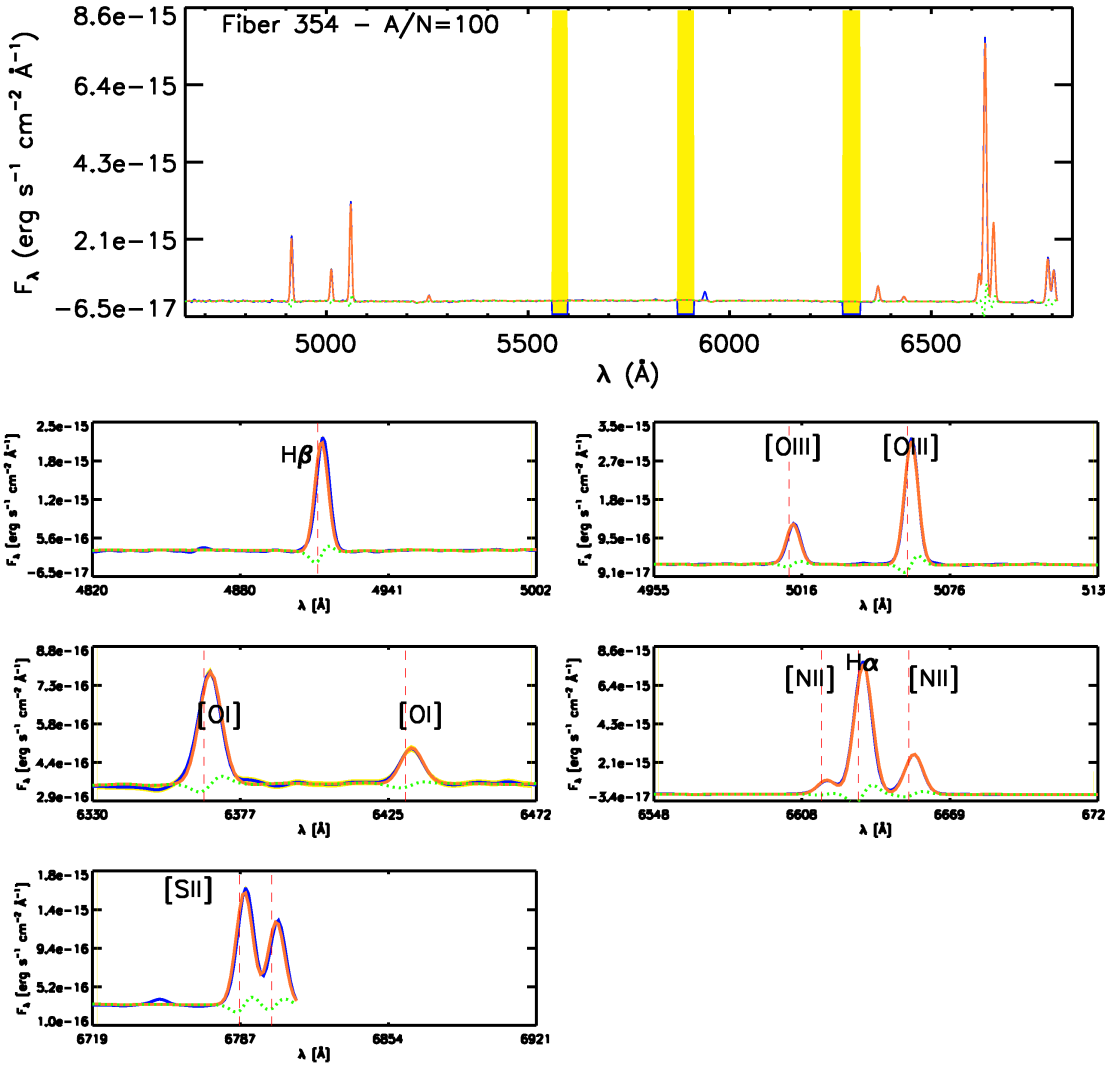

Fig. 1.— Spectrum of fiber 354 with a high A/N =100 in the Arp 299 data cube. The observed spectrum and 1σ uncertainties are shown in blue and the yellow envelope, respectively. The best fit stellar plus emission line spectrum is shown by the orange solid line and the dotted green line shows the stellar component of the fit without the emission lines. The vertical yellow bands are masked regions around sky line residuals.

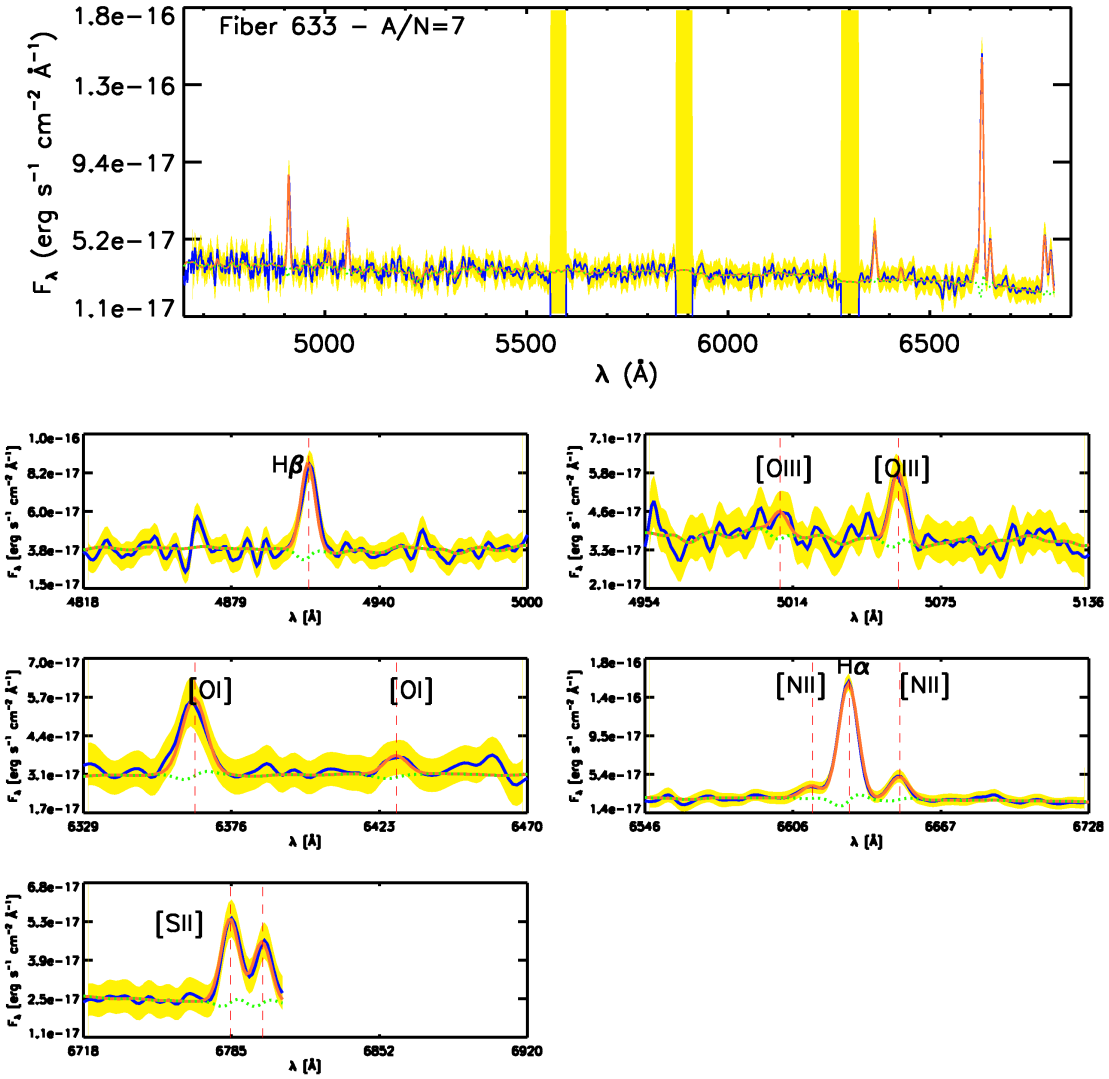

Fig. 2.— Spectrum of fiber 633 with a low A/N =7 in the Arp 299 RSS file. The observed spectrum and 1σ uncertainties are shown in blue and the yellow envelope, respectively. The best fit stellar plus emission line spectrum is shown by the orange solid line and the dotted green line shows the stellar component of the fit without the emission lines. The vertical yellow bands are masked regions around sky line residuals.

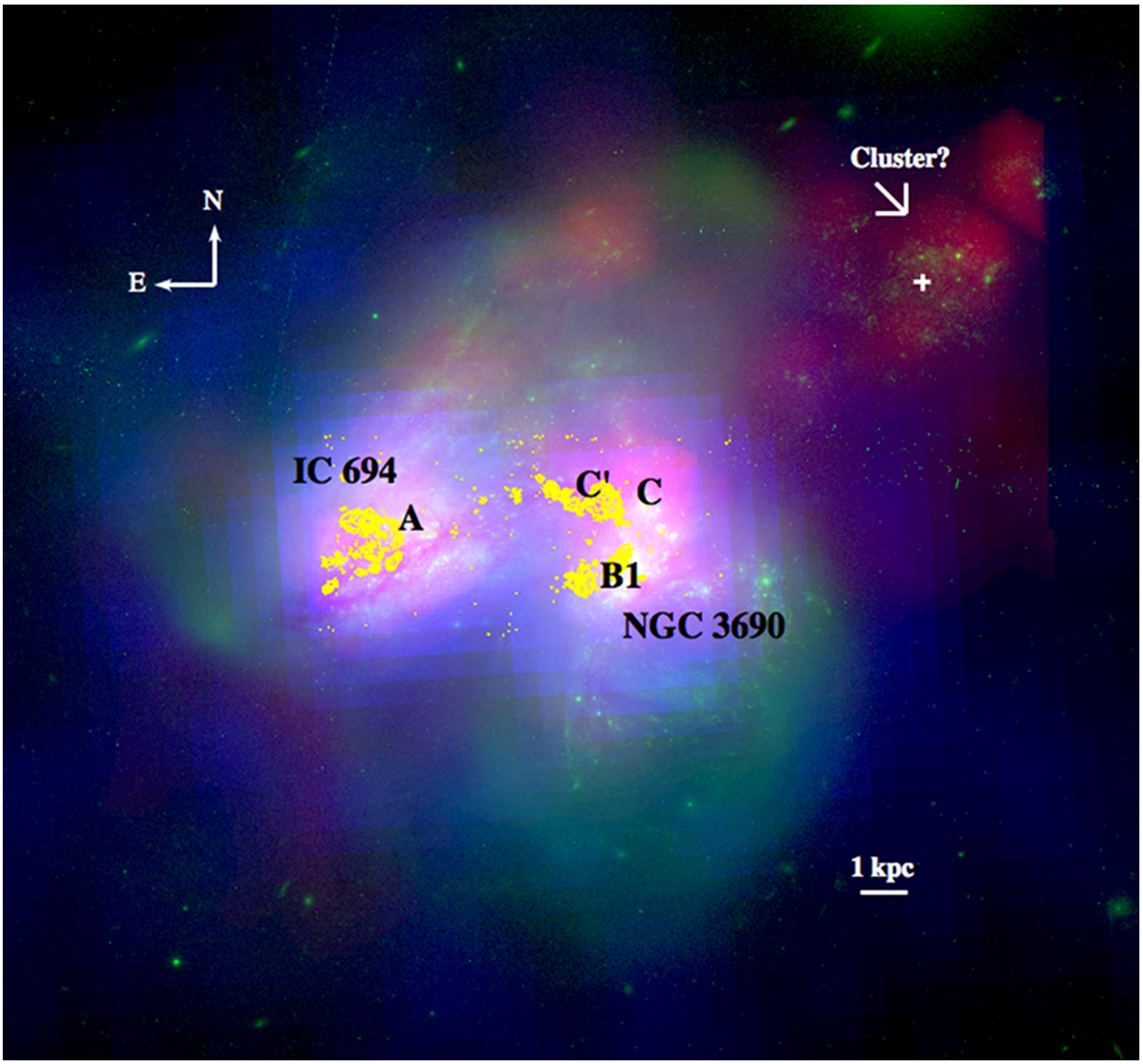

Fig. 3.— RGB image of interpolated Hα flux map based on discrete values at each IFU fiber position (red), archival *HST* 814W image (green), *Spitzer* 24μm image (blue), and contours of *HST* Paα emission (yellow; note coordinates are offset see Alonso-Herrero et al. (2000)). The two main separate components of the Arp 299 merger IC 694 and NGC 3690 and individual nuclei (A and B1) and star forming complexes (C, and C$'$ are indicated. Also shown is a possible stellar cluster associated with a peak in both Hα and HI.

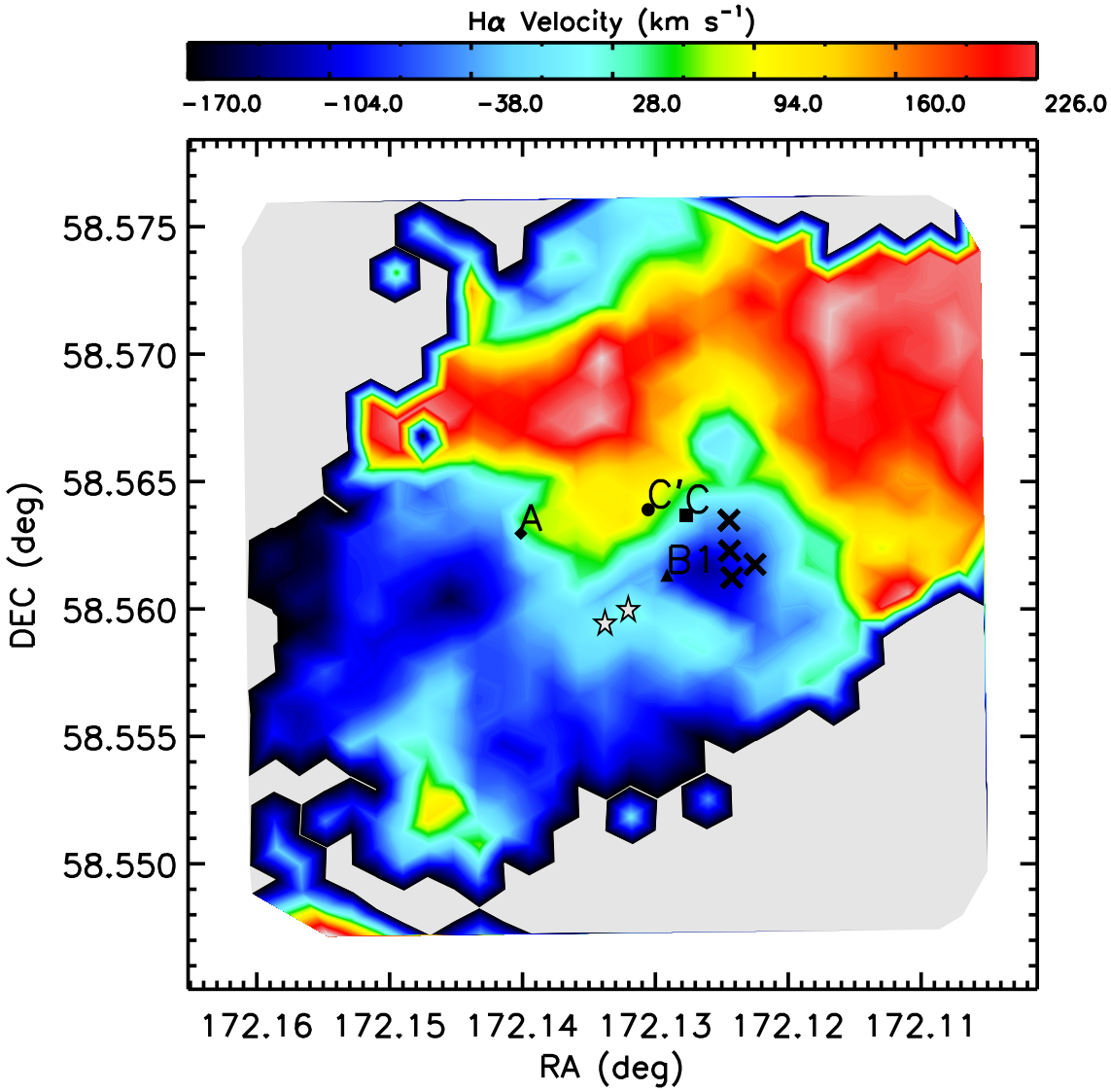

Fig. 4.— Hα ionized gas velocity field. AGN contaminated regions are marked with black cross (X-ray) and stars (IFU).

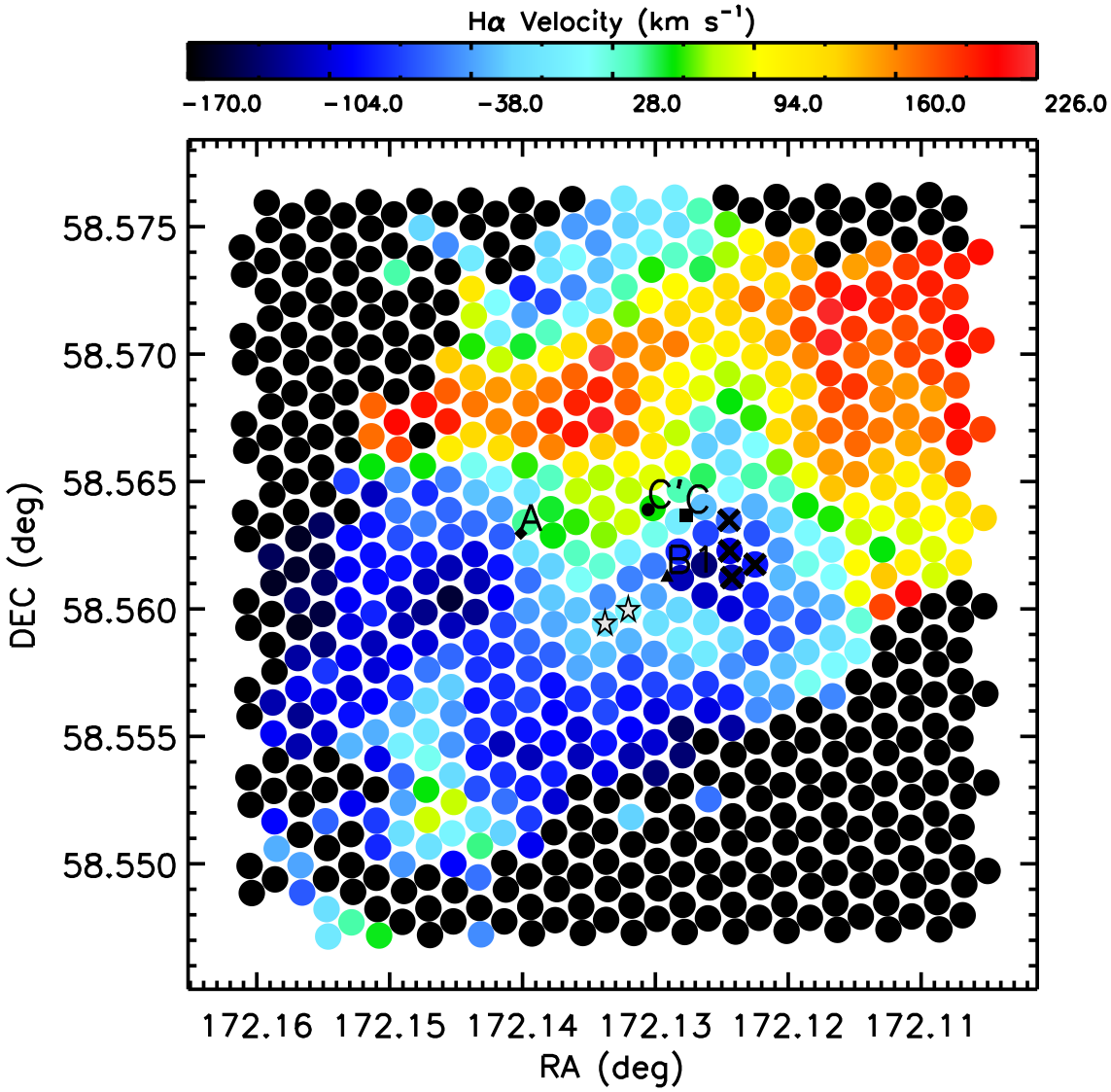

Fig. 5.— Hα ionized gas velocity field. AGN contaminated regions are marked with black cross (X-ray) and stars (IFU) .

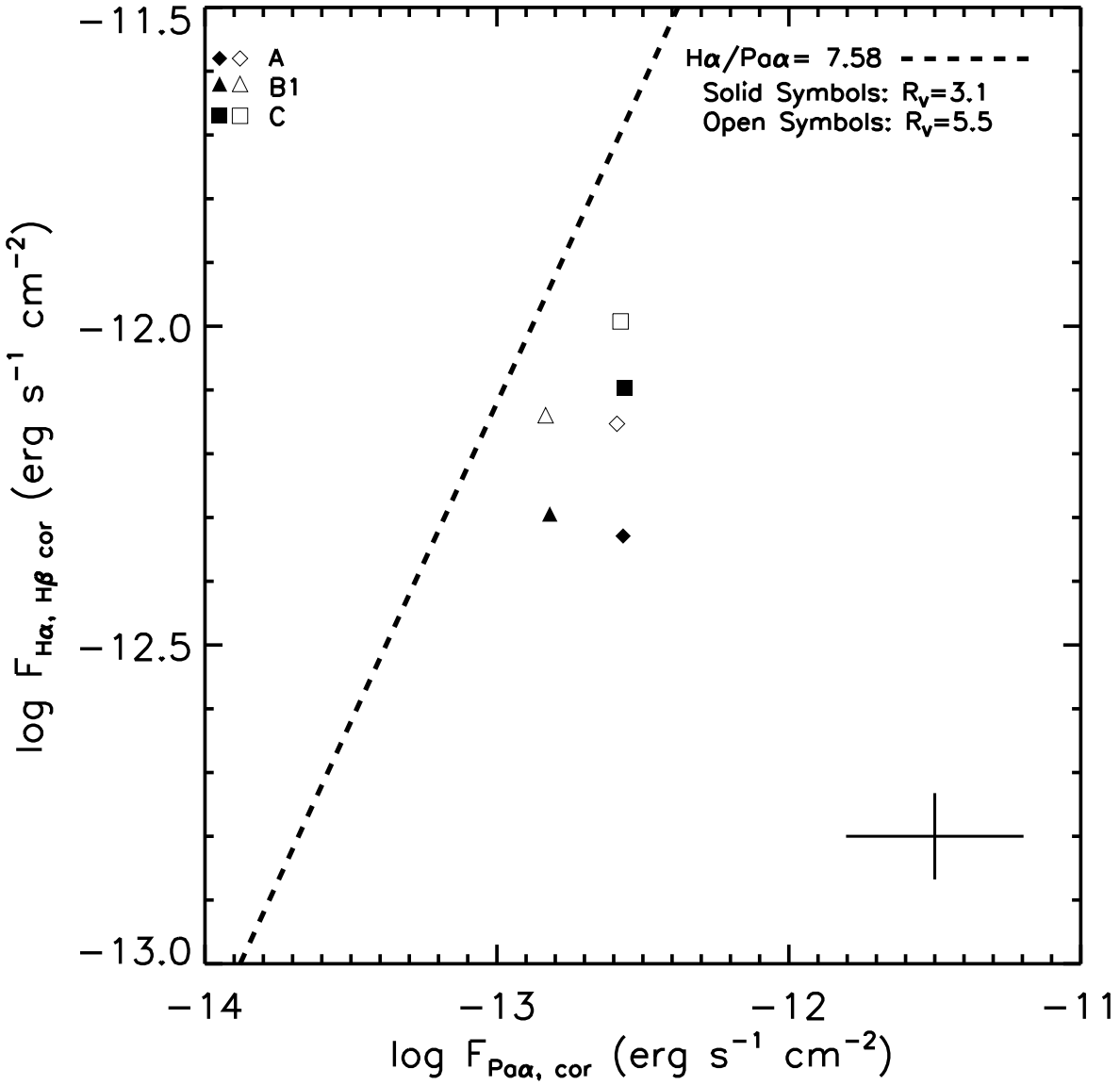

Fig. 6.— Extinction corrected Hαversus Paα fluxes measured in 6″ size apertures in the nuclear regions in Arp 299.

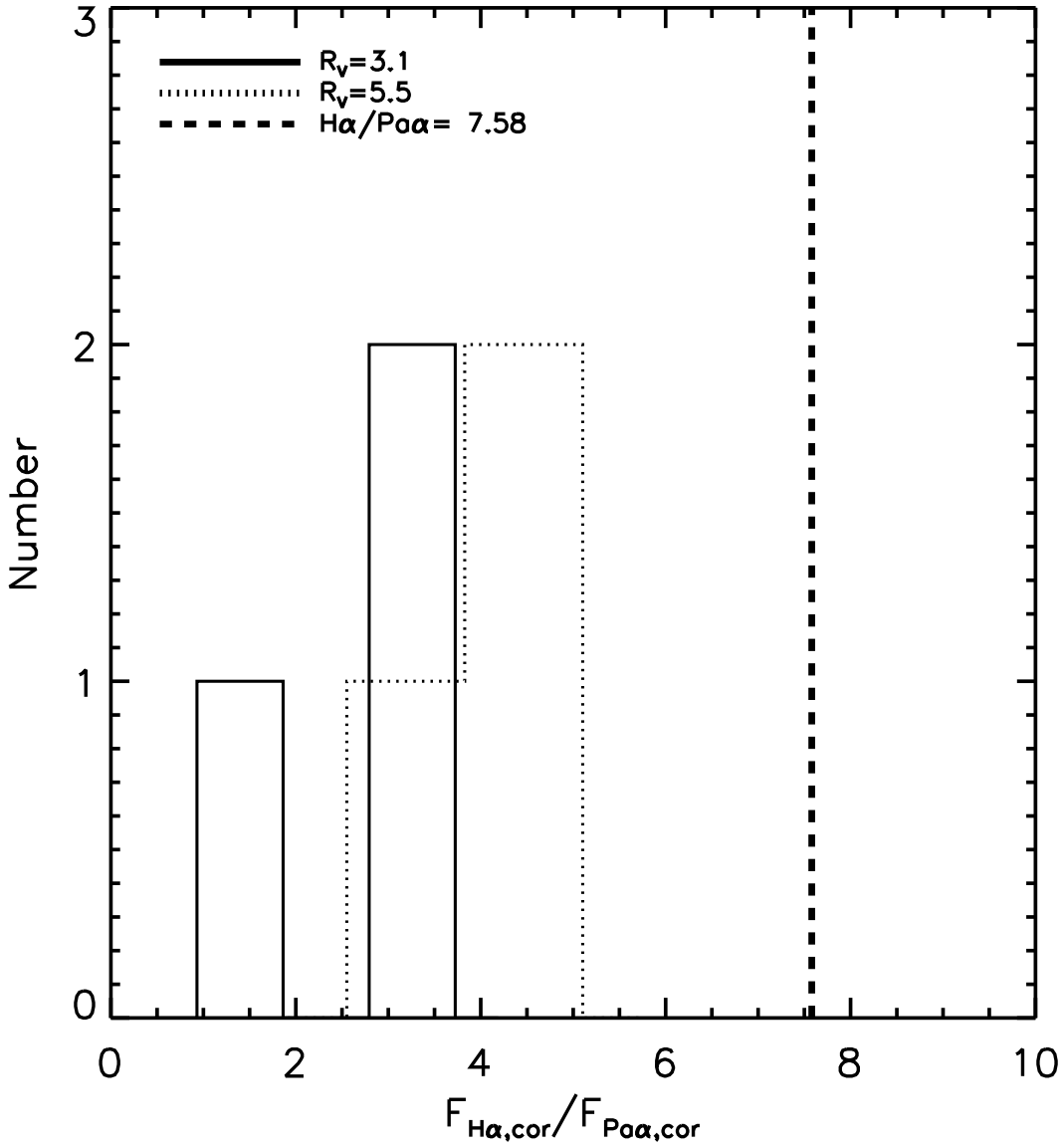

Fig. 7.— Histogram of the extinction corrected Hα/ Paα flux ratio. The dashed line indicates the intrinsic Hα/Paα line ratio of 7.58 from case B recombination line theory.

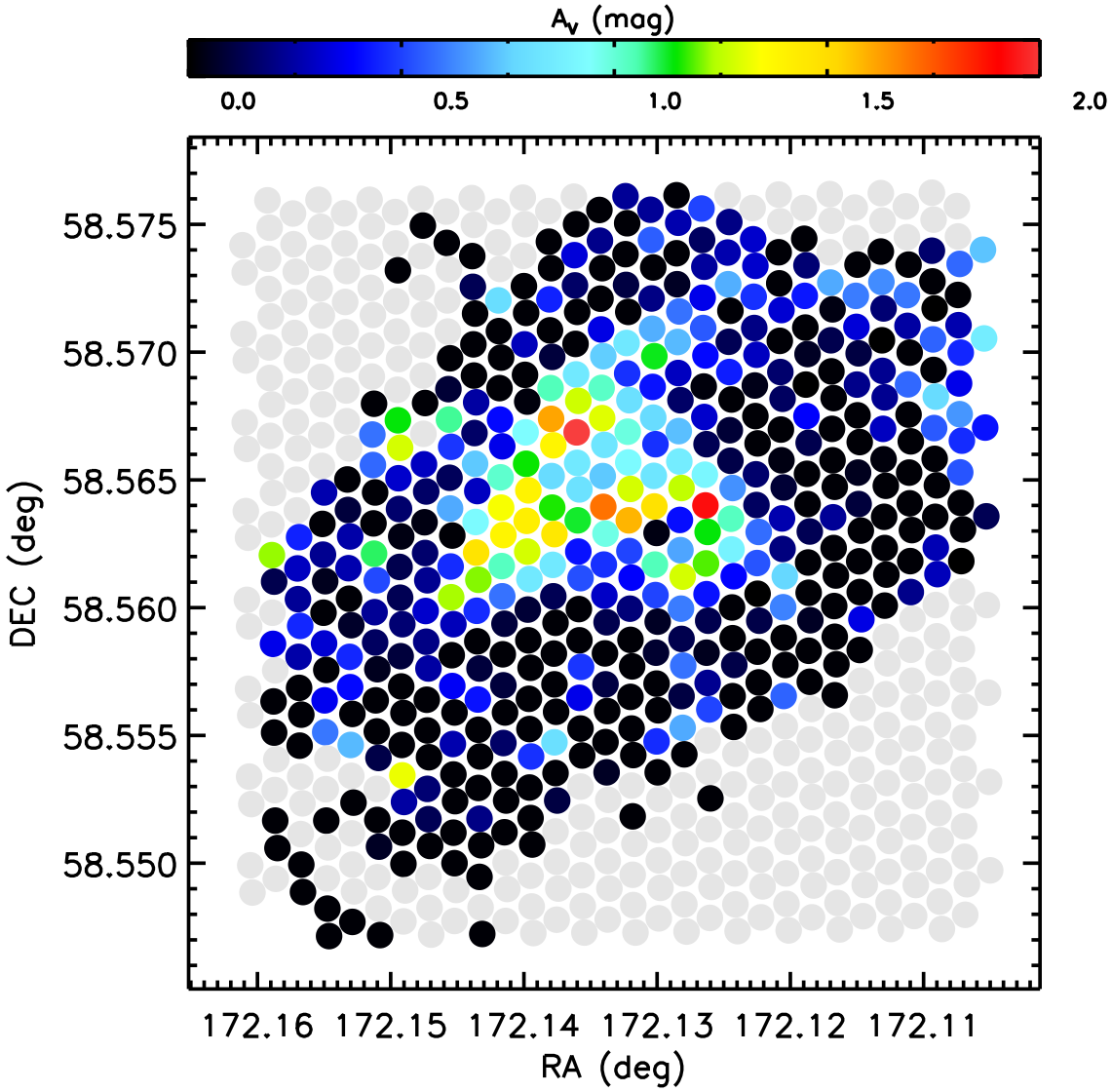

Fig. 8.— Visual extinction map (A_V) from the Balmer decrement (Hβ/Hα) line ratio in IFU fiber sized regions assuming a foreground dust screen model, and a mean interstellar extinction law from Draine (2003).

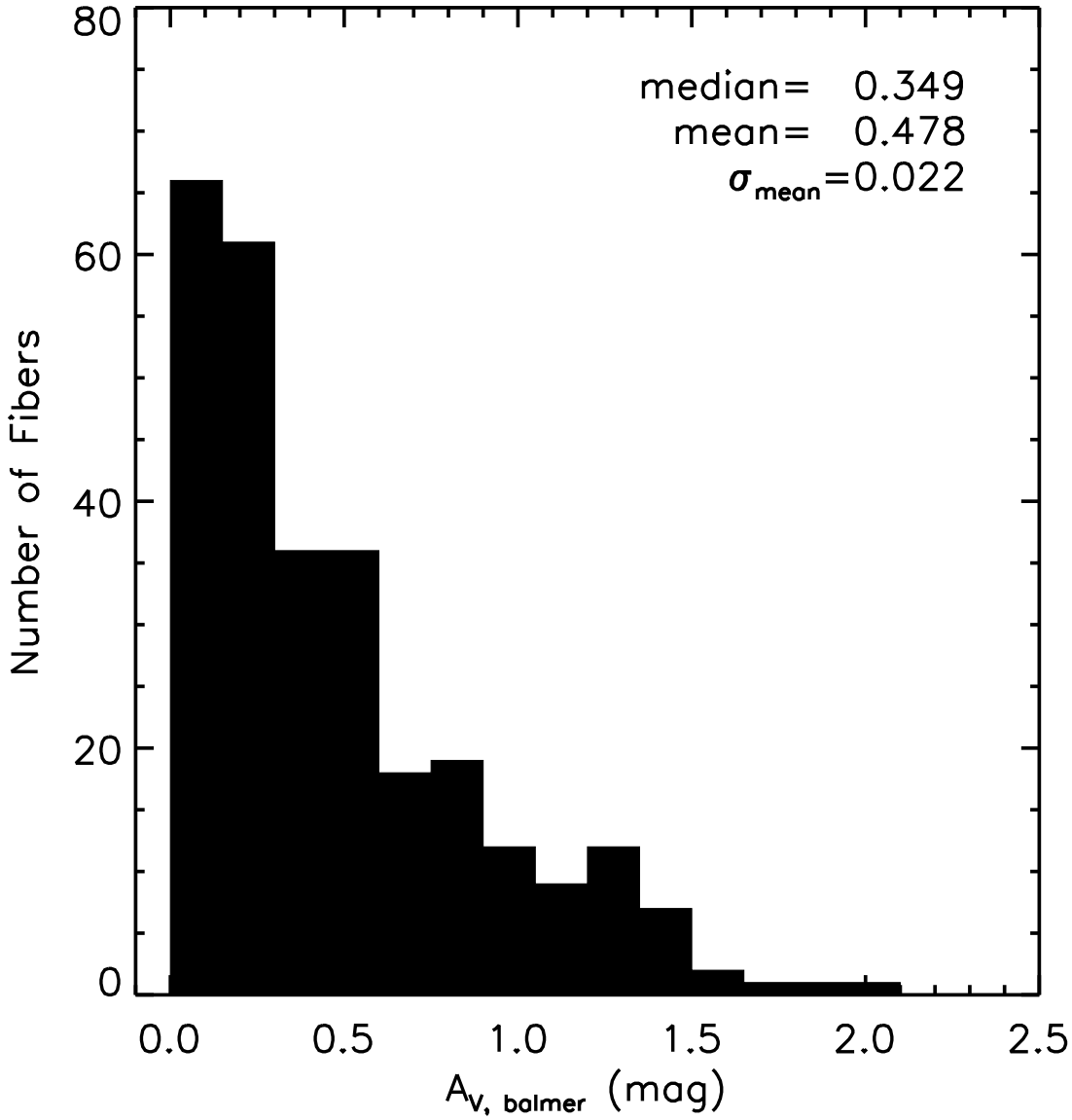

Fig. 9.— Visual extinctions for IFU fiber sized regions with a $S/N > 5$ from the Balmer decrement (Hβ/Hα) line ratio, a foreground dust screen model, and a Galactic extinction law from Draine (2003).

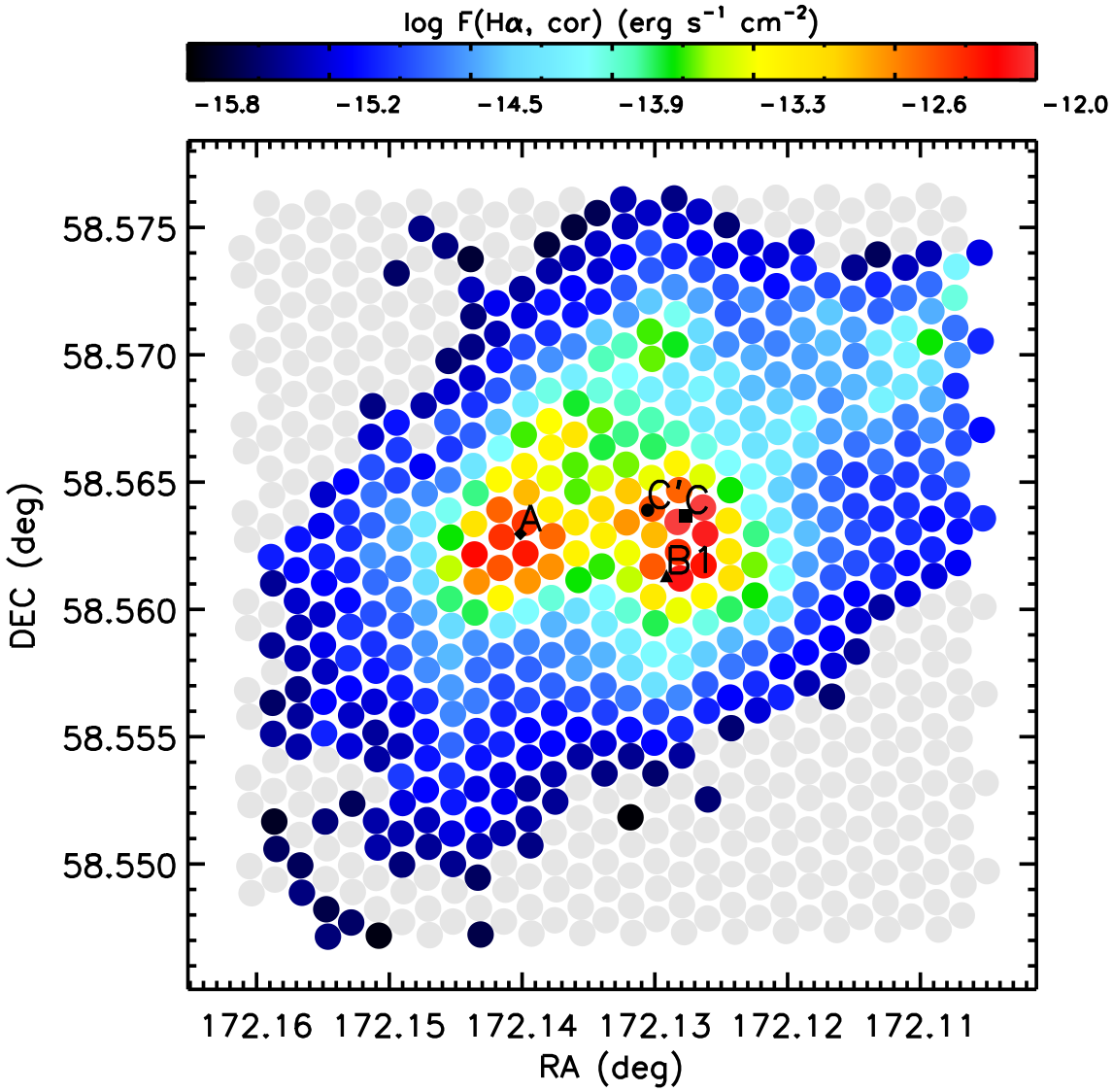

Fig. 10.— Extinction corrected fiber to fiber Hα map of Arp 299 with the locations of nuclear regions A, B1, C, and C′ indicated.

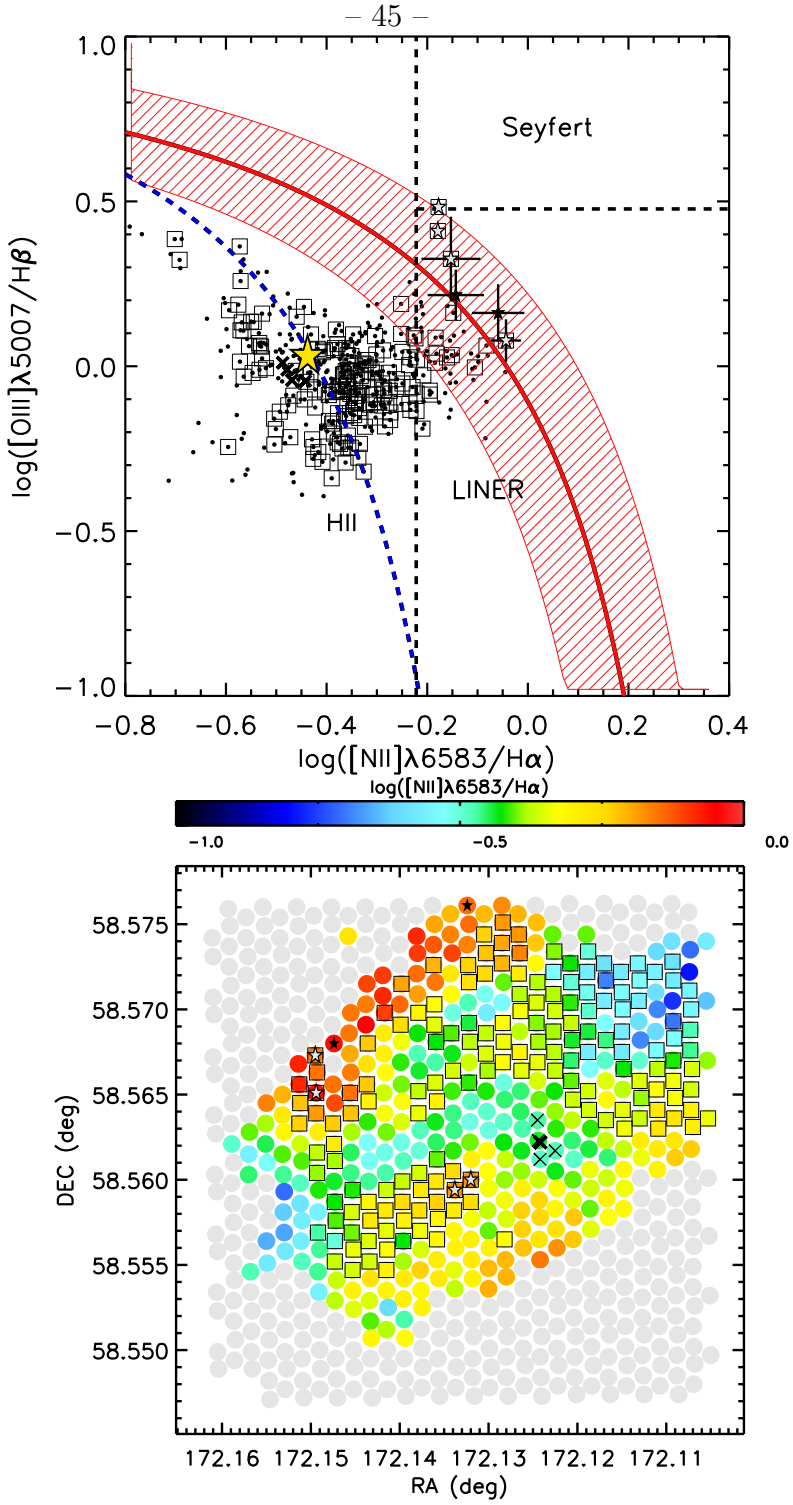

Fig. 11.— **Top:** BPT diagram showing Kewley et al. (2001) extreme starburst classification line (red solid line) and errors (red diagonal line region), the pure star formation classification line from Kauffmann et al. (2003) (blue solid line), and the Ho et al. (1997) classification schemes (black dashed lines). White star points indicated regions that were selected by all three BPT diagrams, boxed points indicate regions selected by two or more BPT diagrams, and crosses mark regions within a 6″ radius of the X-ray selected AGN from (Ballo et al. 2004). The solid yellow star shows the integrated ratio for the system. **Bottom:** The AGN selected regions (star and boxed points) are overlaid on an fiber-by-fiber [NII]/Hα flux map.

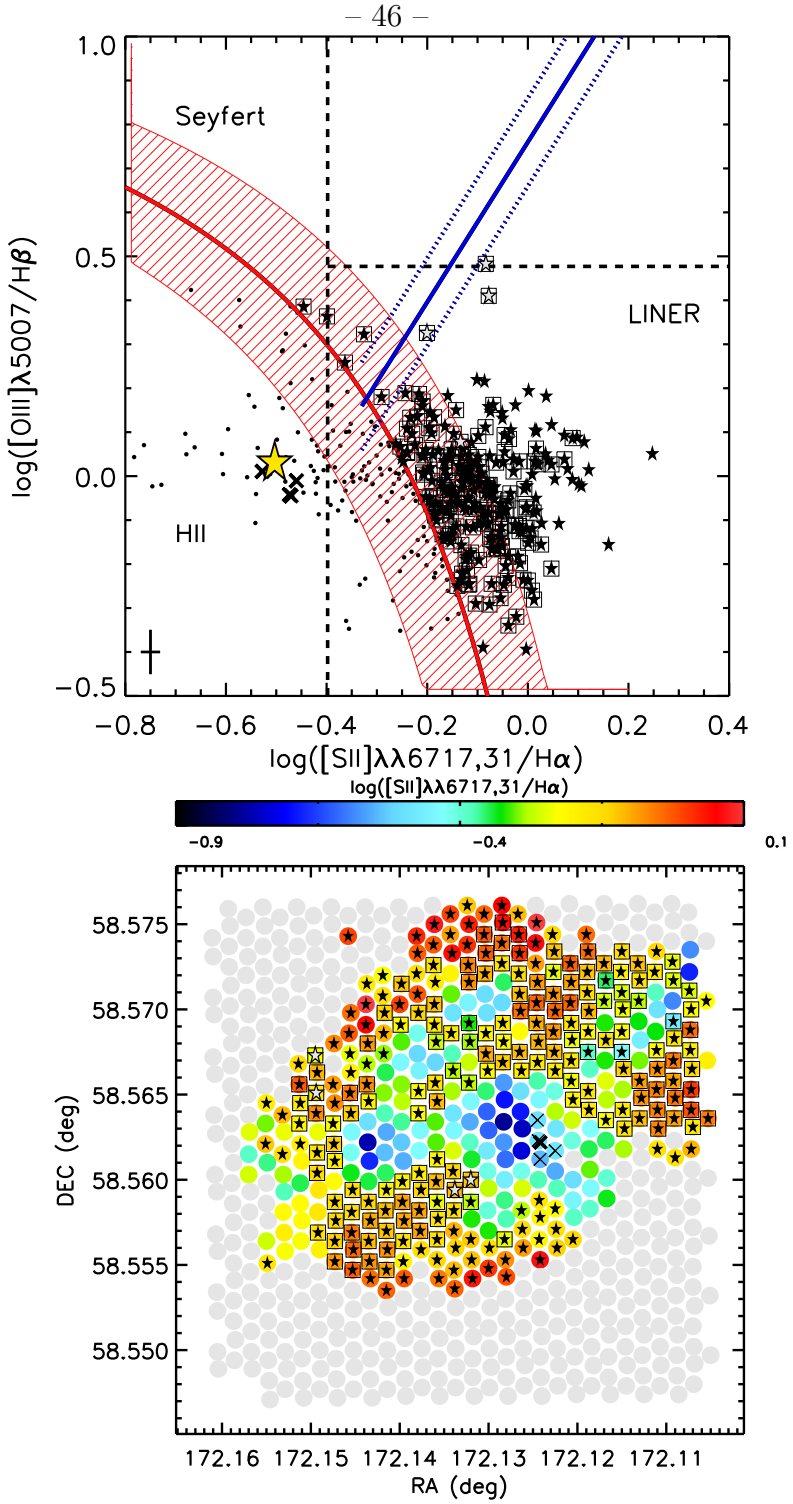

Fig. 12.— **Top:** BPT diagram showing Kewley et al. (2001) extreme starburst classification line (red solid line) and errors (red diagonal line region), the Kewley et al. (2006) Seyfert-LINER line (blue and solid diagonal lines), and the Ho et al. (1997) classification schemes (black dashed lines). White star points indicated regions that were selected by all three BPT diagrams, boxed points indicate regions selected by two or more BPT diagrams, and crosses mark regions within a 6″ radius of the X-ray selected AGN from (Ballo et al. 2004). The solid yellow star shows the integrated ratio for the system. **Bottom:** The AGN selected regions (star and boxed points) are overlaid on an fiber-by-fiber [SII]/Hα flux map.

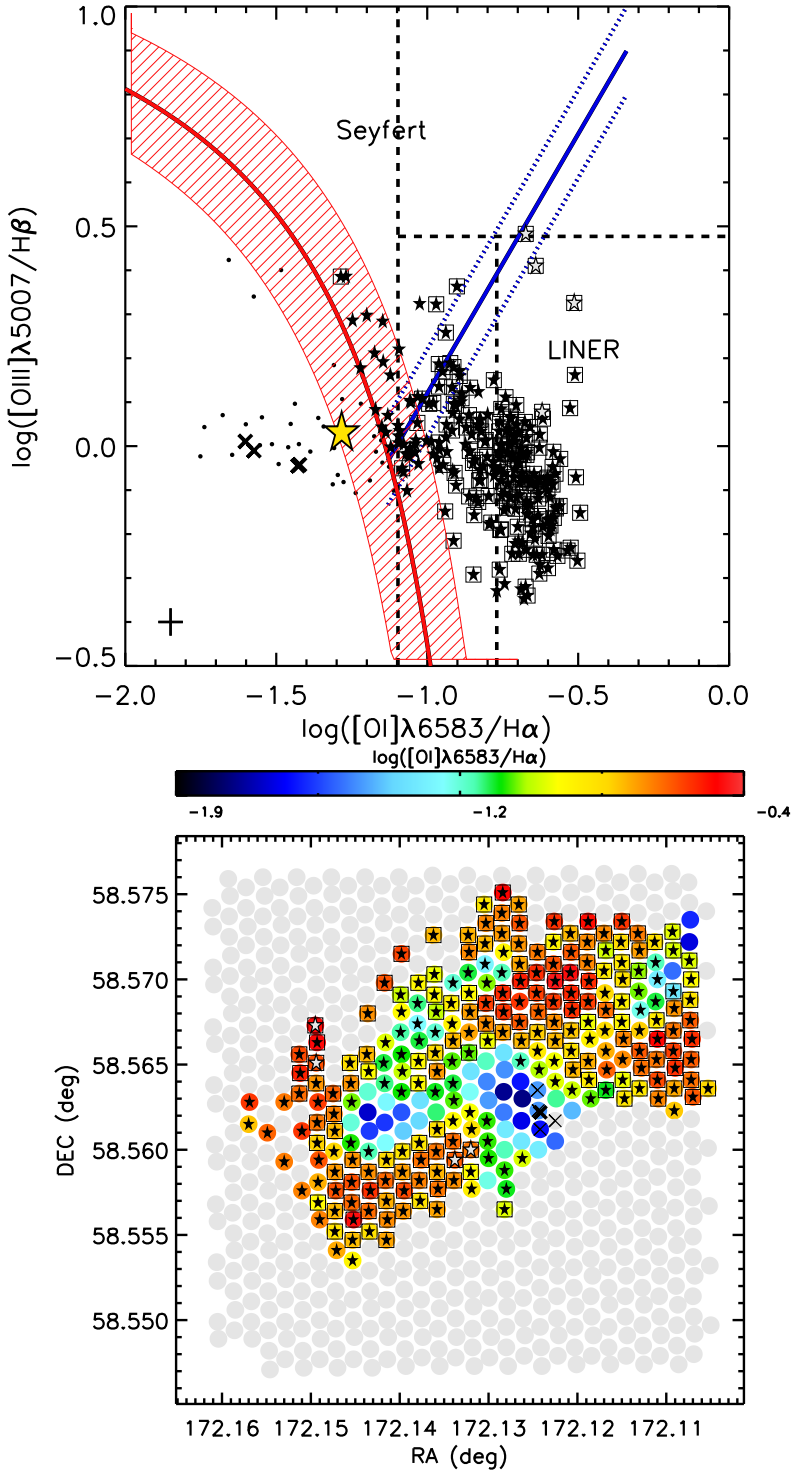

Fig. 13.— **Top:** BPT diagram showing Kewley et al. (2001) extreme starburst classification line (red solid line) and errors (red diagonal line region), the Kewley et al. (2006) Seyfert-LINER line (blue and solid diagonal lines), and the Ho et al. (1997) classification schemes (black dashed lines). White star points indicated regions that were selected by all three BPT diagrams, boxed points indicate regions selected by two or more BPT diagrams, and crosses mark regions within a 6″ radius of the X-ray selected AGN from (Ballo et al. 2004). The solid yellow star shows the integrated ratio for the system. **Bottom:** The AGN selected regions (star and boxed points) are overlaid on an fiber-by-fiber [OI]/Hα flux map.

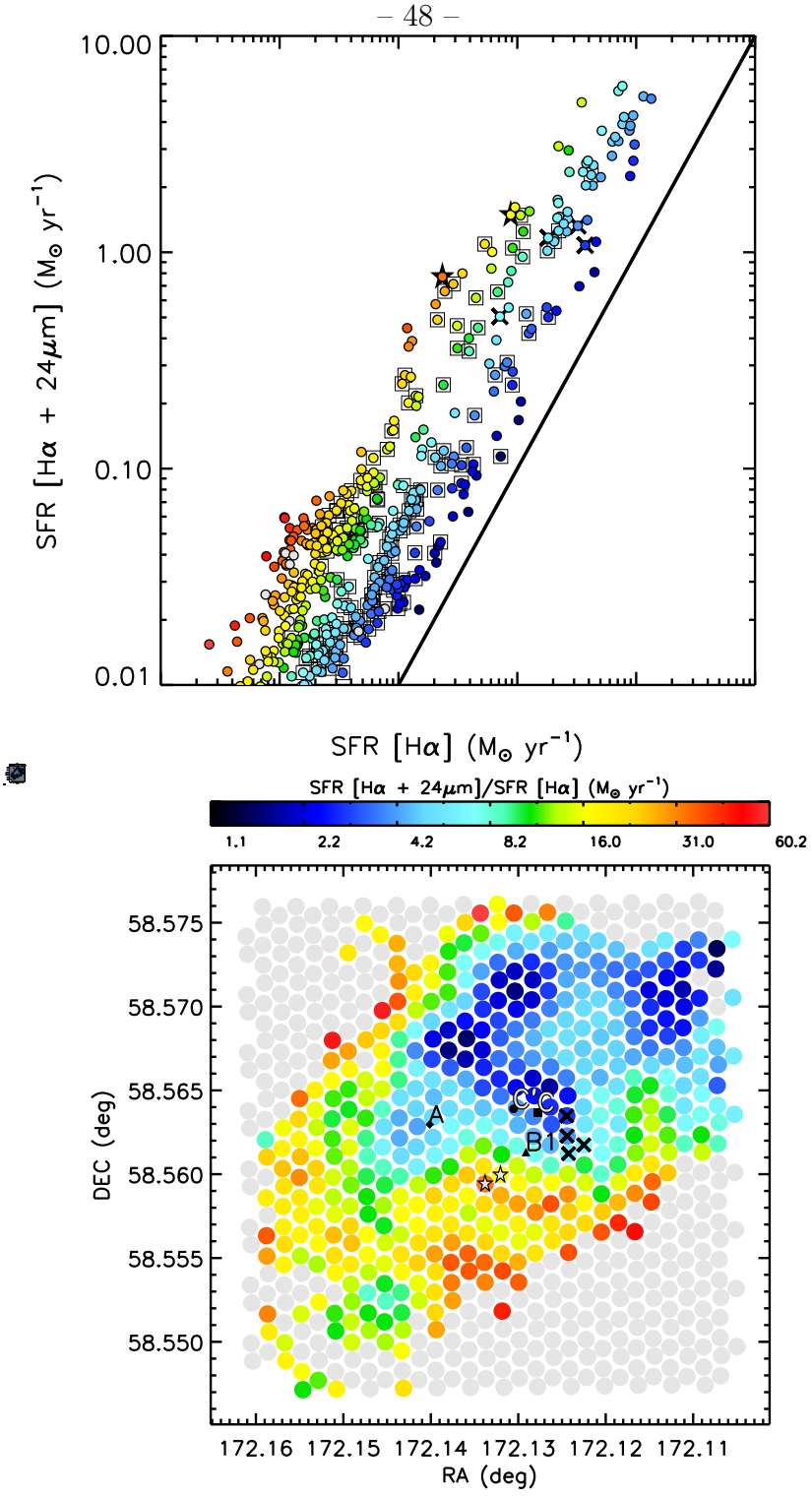

Fig. 14.— **Top:** Comparison of extinction corrected Hα and 24μm SFRs measured on scales of 24μm resolution (6″). Potential AGN contaminated points are denoted by stars and open squares. The colors represent the ratio of SFR [Hα +24μm] /SFR[Hα] shown in the bottom panel. The dark blue points represent where there is a roughly linear relation between the Hα +24μm and Hα based SFRs. The solid black line is a linear relation at a SFR of 0.01. **Bottom:** The ratio of Ha+24μm to extinction corrected Hα SFRs measured on scales of 24μm resolution (6″). AGN contaminated regions are marked with black cross (X-ray) and stars (IFU)

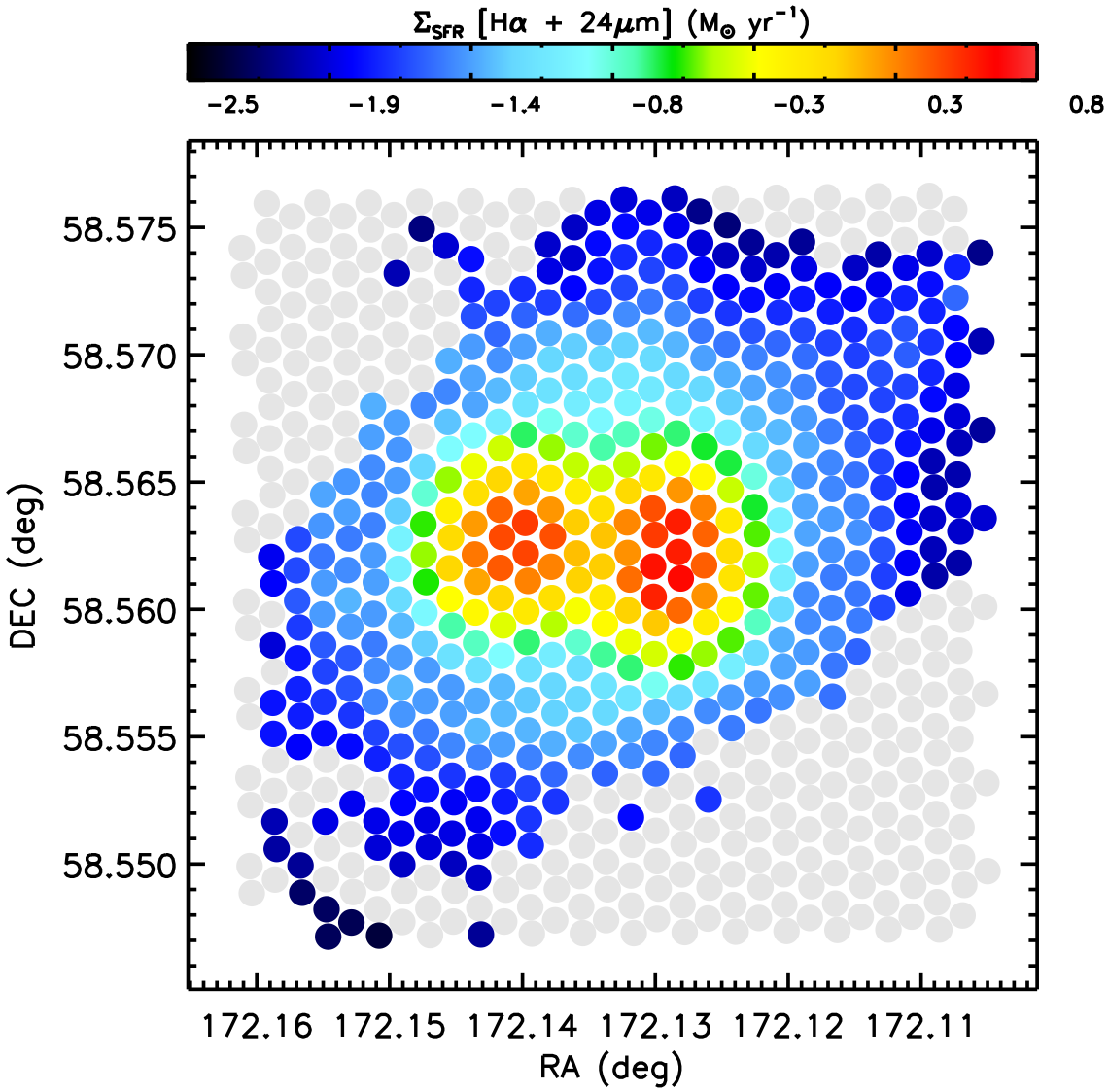

Fig. 15.— $\Sigma_{\rm SFR\ [H\alpha+24\mu m]}$map where circles indicated 1.3 kpc scales and Hα line fluxes have $A/N \geq 4$.

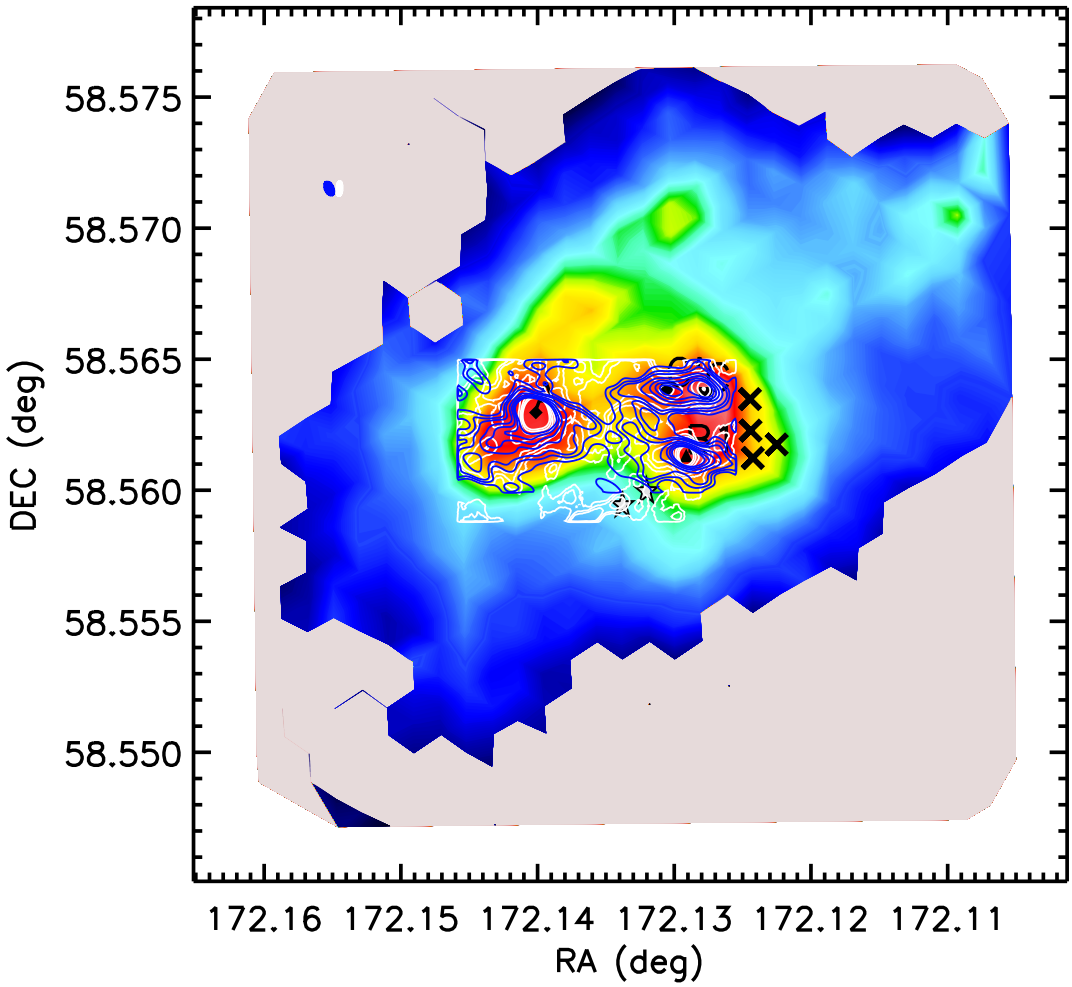

Fig. 16.— Interpolated Hα flux map based on discrete values at each IFU fiber position overlaid with HI (red) contours and contours starting at 2σ above the noise level and increase intervals of 2σ... Hα flux map overlaid with CO$J = 2 \rightarrow 1$ (blue) CO$J = 3 \rightarrow 2$ (white) contours starting at 2σ above the noise level and increase... Map beam sizes are shown in the top left corner. AGN contaminated regions are marked with black cross (X-ray) and stars (IFU).

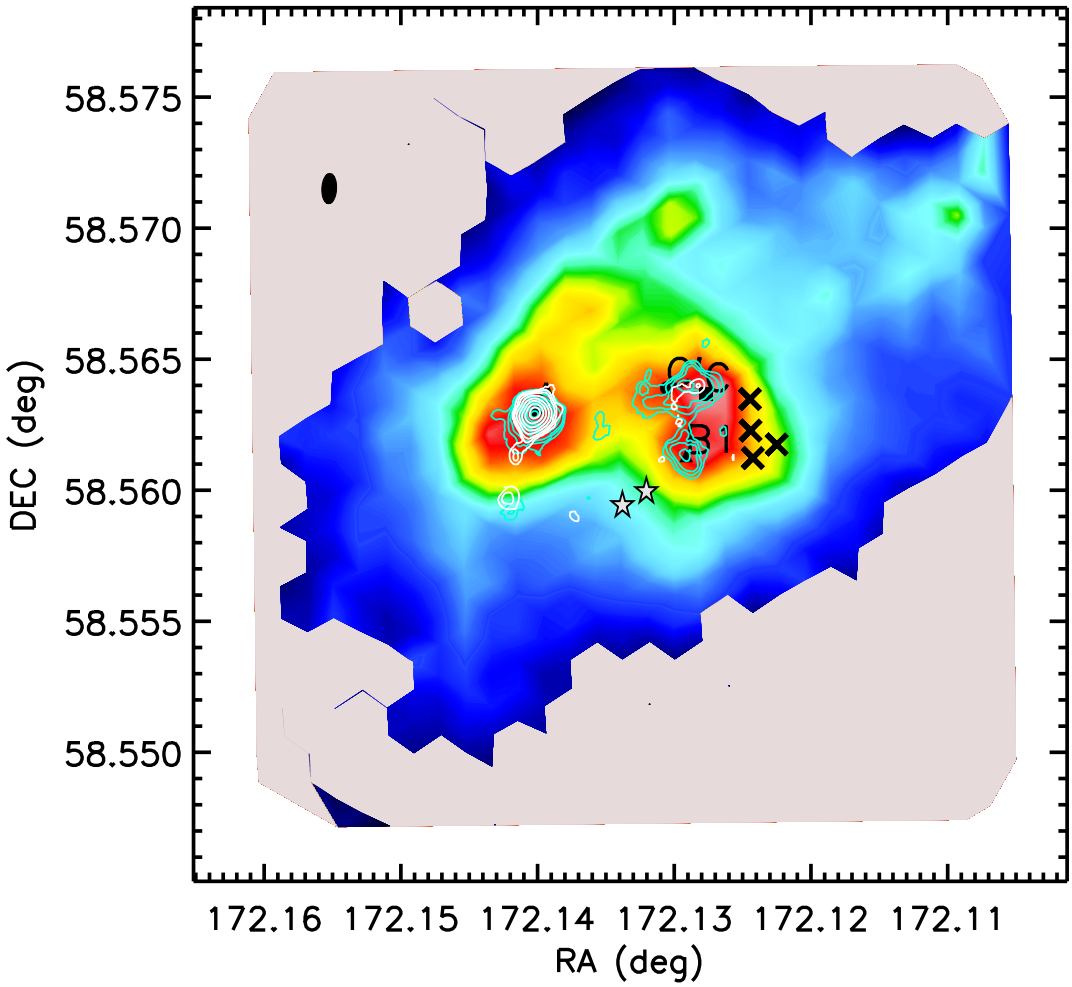

Fig. 17.— Interpolated Hα flux map based on discrete values at each IFU fiber position overlaid with HCN(1–0) (cyan) contours and HCO^+(1–0) contours (white) starting at 2σ above the noise level and increase intervals of 2σ. Map beam sizes are shown in the top left corner. AGN contaminated regions are marked with black cross (X-ray) and stars (IFU).

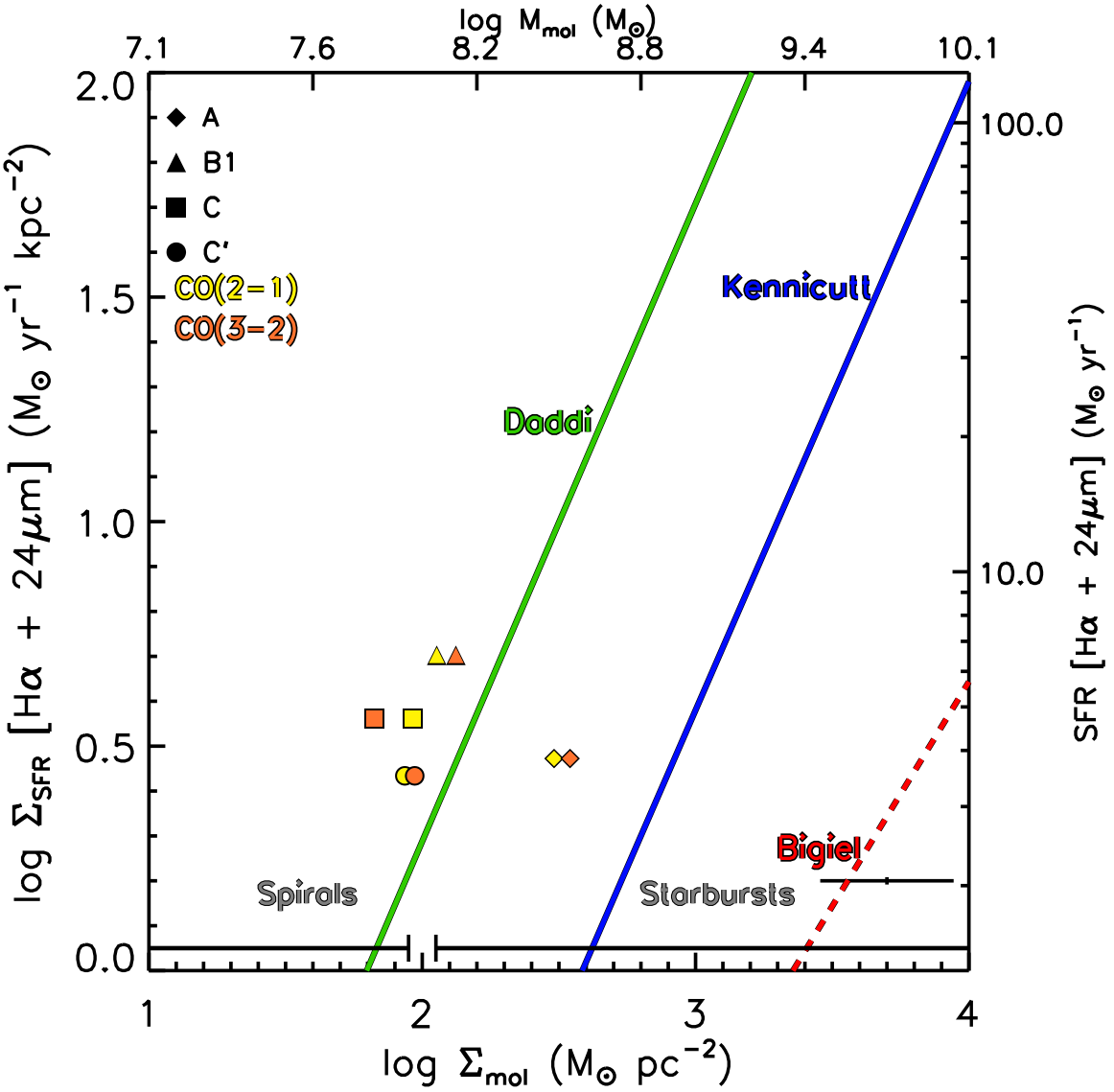

Fig. 18.— SFR–Mol gas surface density measurements of the nuclear regions of Arp 299 using CO$J = 2 \rightarrow 1$ and CO$J = 3 \rightarrow 2$ on scales of 1.3 kpc. The mass ($M_{\rm Mol}$) is calculated using the same aperture area (3″ in radius). Lines indicate extragalactic relations on disk-averaged scales for spirals and starbursts (blue line; Kennicutt 1998) and high-z mergers (green line; Daddi et al. 2010), as well as in 1 kpc regions in spirals and dwarf galaxies (red line; Bigiel et al. 2011).

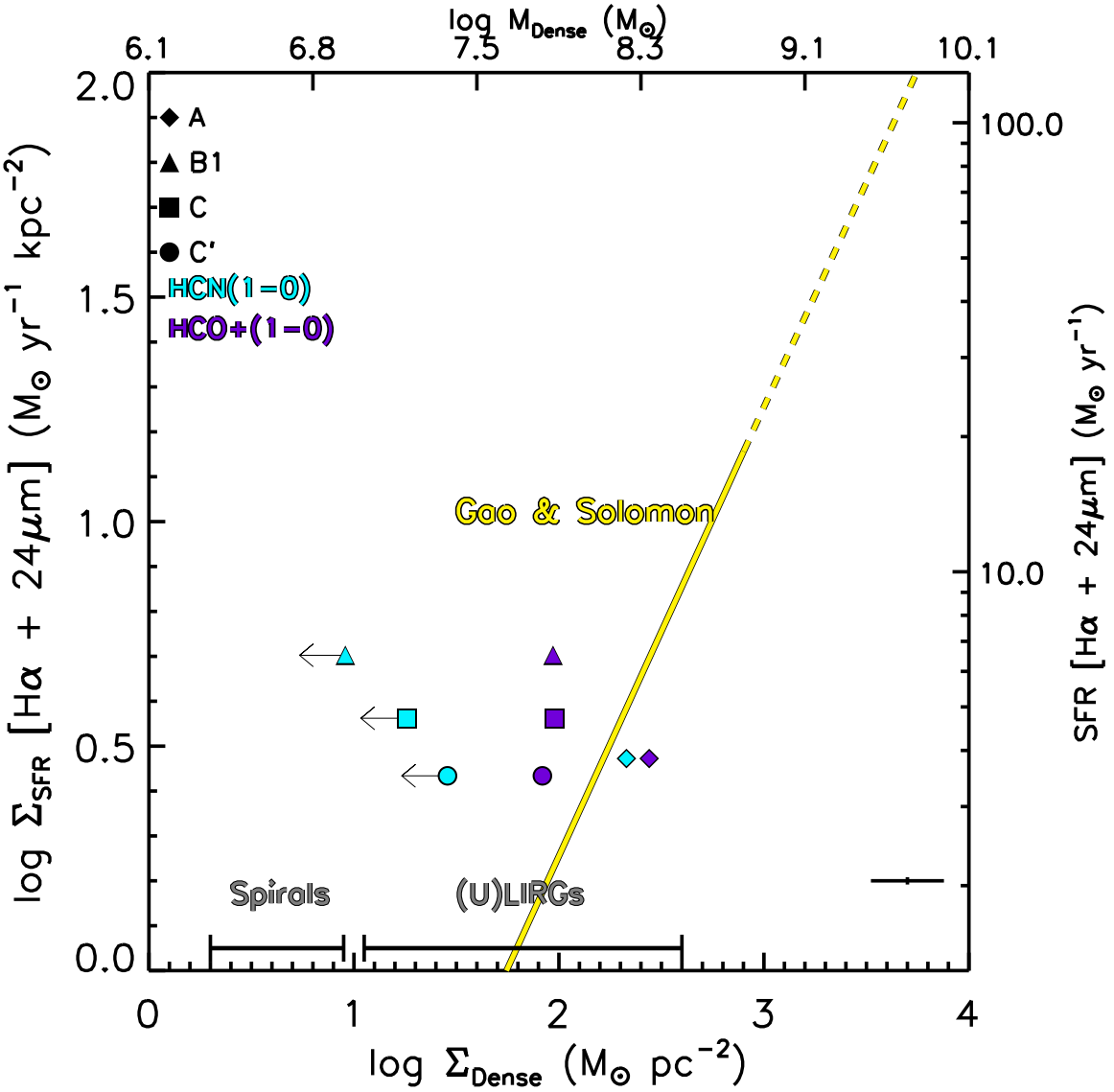

Fig. 19.— SFR–Dense gas surface density measurements of the nuclear regions of Arp 299 using HCN(1–0) and HCO^+(1–0) on scales of 1.3 kpc. The mass ($M_{\rm Dense}$) is calculated using the same aperture area (3″ in radius). The yellow line indicates the SFR–Dense gas relation on disk-averaged scales for spirals and (U)LIRGs (Gao & Solomon 2004b).

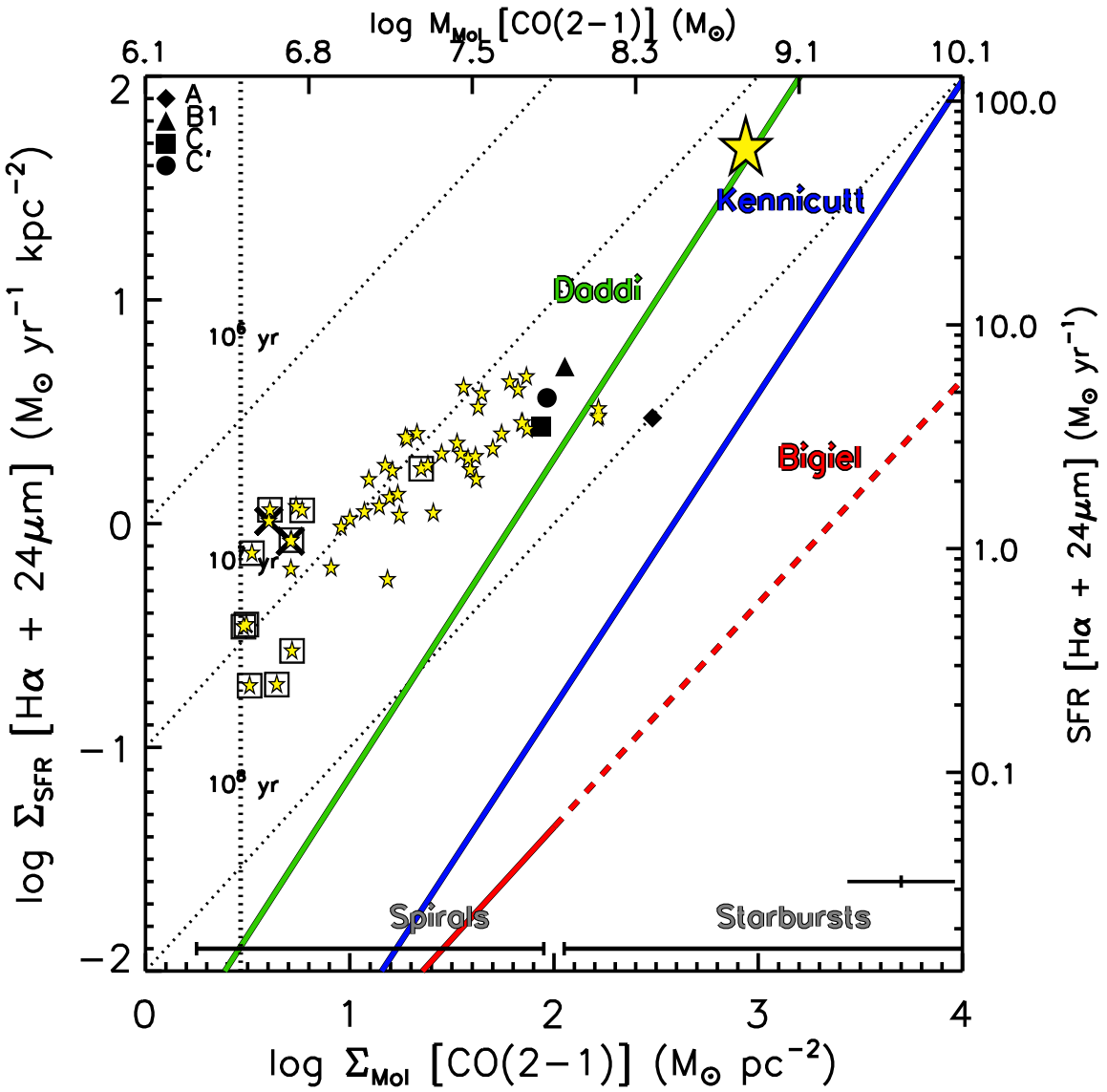

Fig. 20.— Spatially resolved SFR–Mol gas surface density relations from measurements at each IFU fiber position with COJ=2–1 coverage on scales of 1.3 kpc. The mass ($M_{\rm Mol}$) is calculated using the same aperture area (3″ in radius). The dotted vertical line is the sensitivity limit of the CO$J = 2 \rightarrow 1$ map. Large yellow star is the integrated value for Arp 299. Lines indicate extragalactic relations on disk-averaged scales for spirals and starbursts (blue line; Kennicutt (1998)) and high-z mergers (green line; Daddi et al. (2010)), as well as in 1 kpc regions in spirals and dwarf galaxies (red line; Bigiel et al. (2011)). AGN contaminated regions are marked with boxes from IFU line fluxes and black crosses (X-ray).

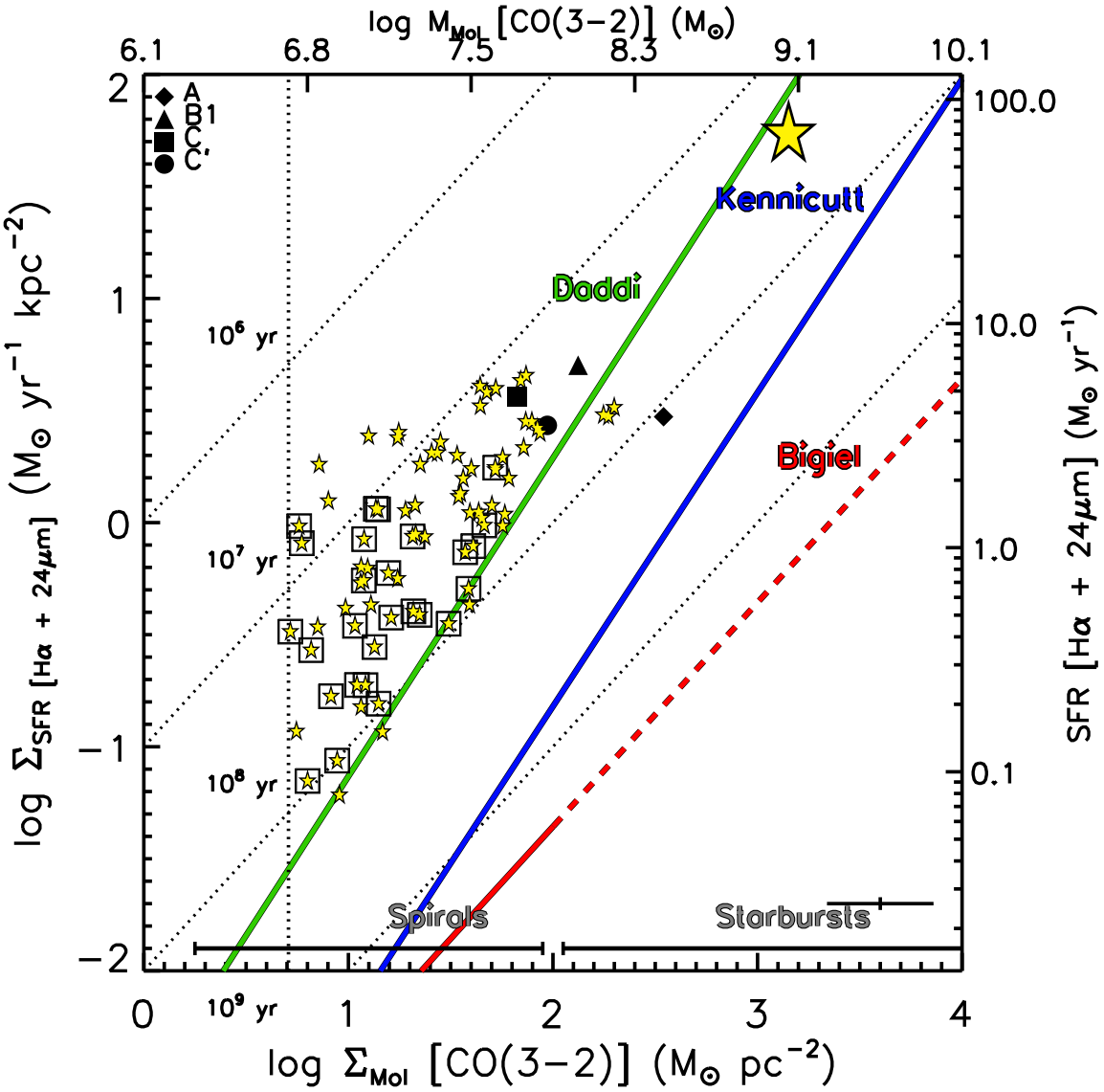

Fig. 21.— Spatially resolved SFR–Mol gas surface density relations from measurements at each IFU fiber position with COJ=3–2 coverage on scales of 1.3 kpc. The mass ($M_{\rm Mol}$) is calculated using the same aperture area (3″ in radius). The dotted vertical line is the sensitivity limit of the CO$J = 2 \rightarrow 1$ map. Large yellow star is the integrated value for Arp 299. Lines indicate extragalactic relations on disk-averaged scales for spirals and starbursts (blue line; Kennicutt (1998)) and high-z mergers (green line; Daddi et al. (2010)), as well as in 1 kpc regions in spirals and dwarf galaxies (red line; Bigiel et al. (2011)). AGN contaminated regions are marked with boxes from IFU line fluxes.

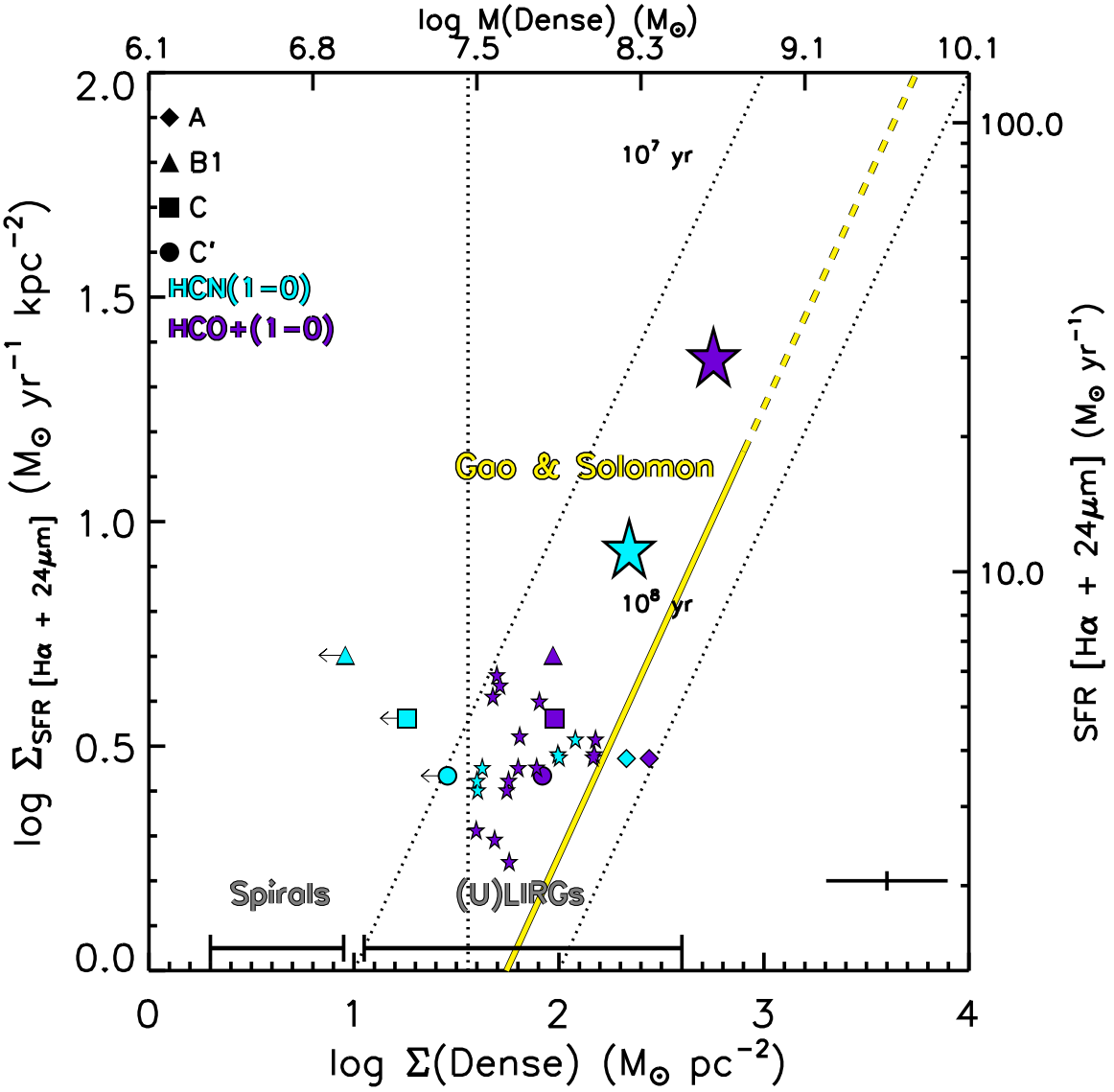

Fig. 22.— Spatially resolved SFR–Dense gas surface density relations from measurements at using HCN(1–0) and HCO^+(1–0) each IFU fiber position on scales of 1.3 kpc. The mass ($M_{\rm Dense}$) is calculated using the same aperture area (3″ in radius). The dotted vertical line is the sensitivity limit of the HCN$J = 1 \rightarrow 0$ and $HCO^+ J = 1 \rightarrow 0$ maps. The large cyan and purple stars are the integrated value of HCN$J = 1 \rightarrow 0$ and $HCO^+ J = 1 \rightarrow 0$ for Arp 299. The yellow line indicates the SFR–Dense gas relation on disk-averaged scales for spirals and (U)LIRGs (Gao & Solomon 2004b).

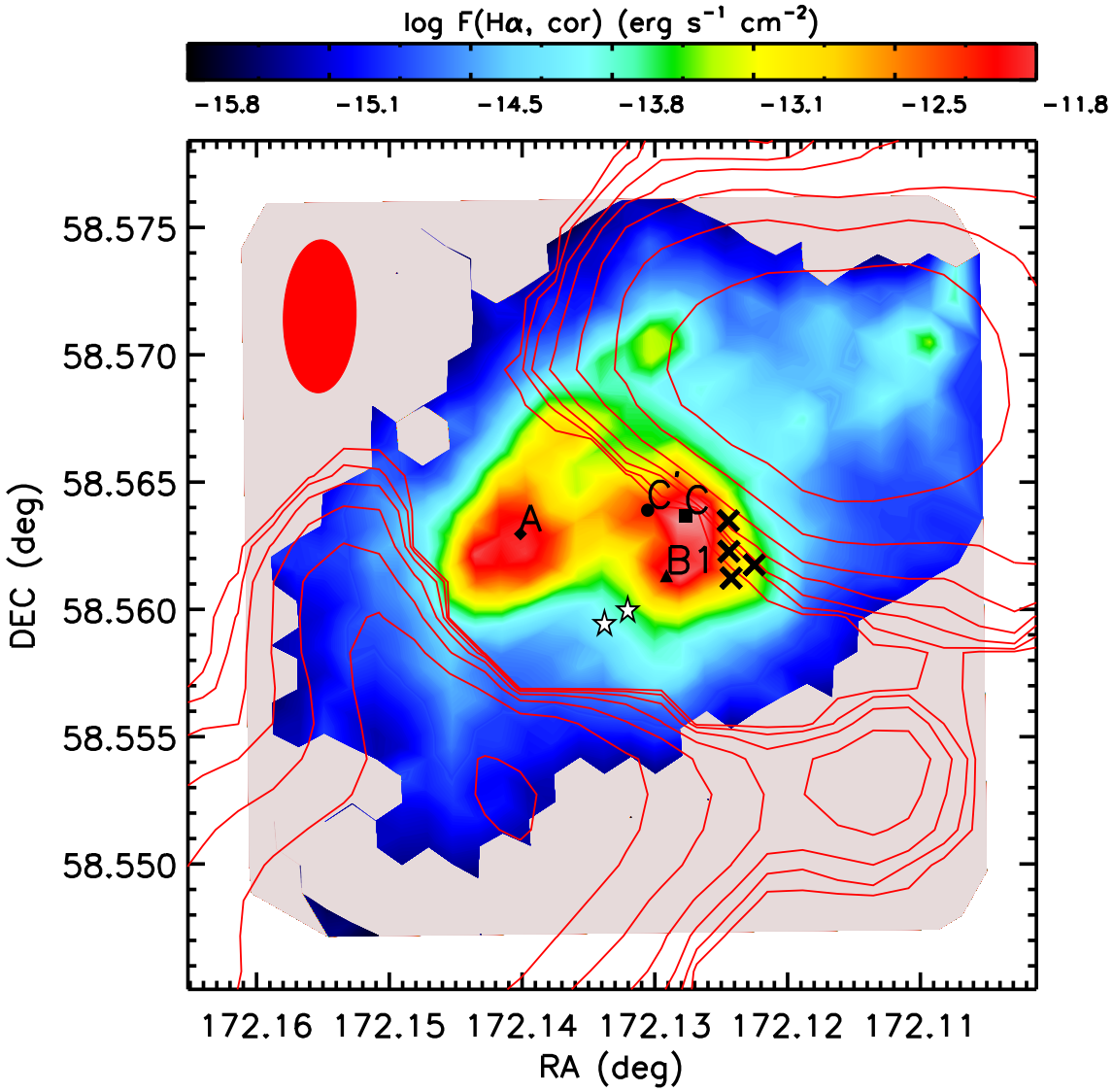

Fig. 23.— Interpolated Hα flux map based on discrete values at each IFU fiber position overlaid with HI (red) contours and contours starting at 2σ above the noise level and increase intervals of 2σ. The two main separate components of the Arp 299 merger IC 694 and NGC 3690 and individual nuclei (A, B1, and B2) and star forming complexes (C, and C′ are indicated. AGN contaminated regions are marked with black cross (X-ray) and stars (IFU).

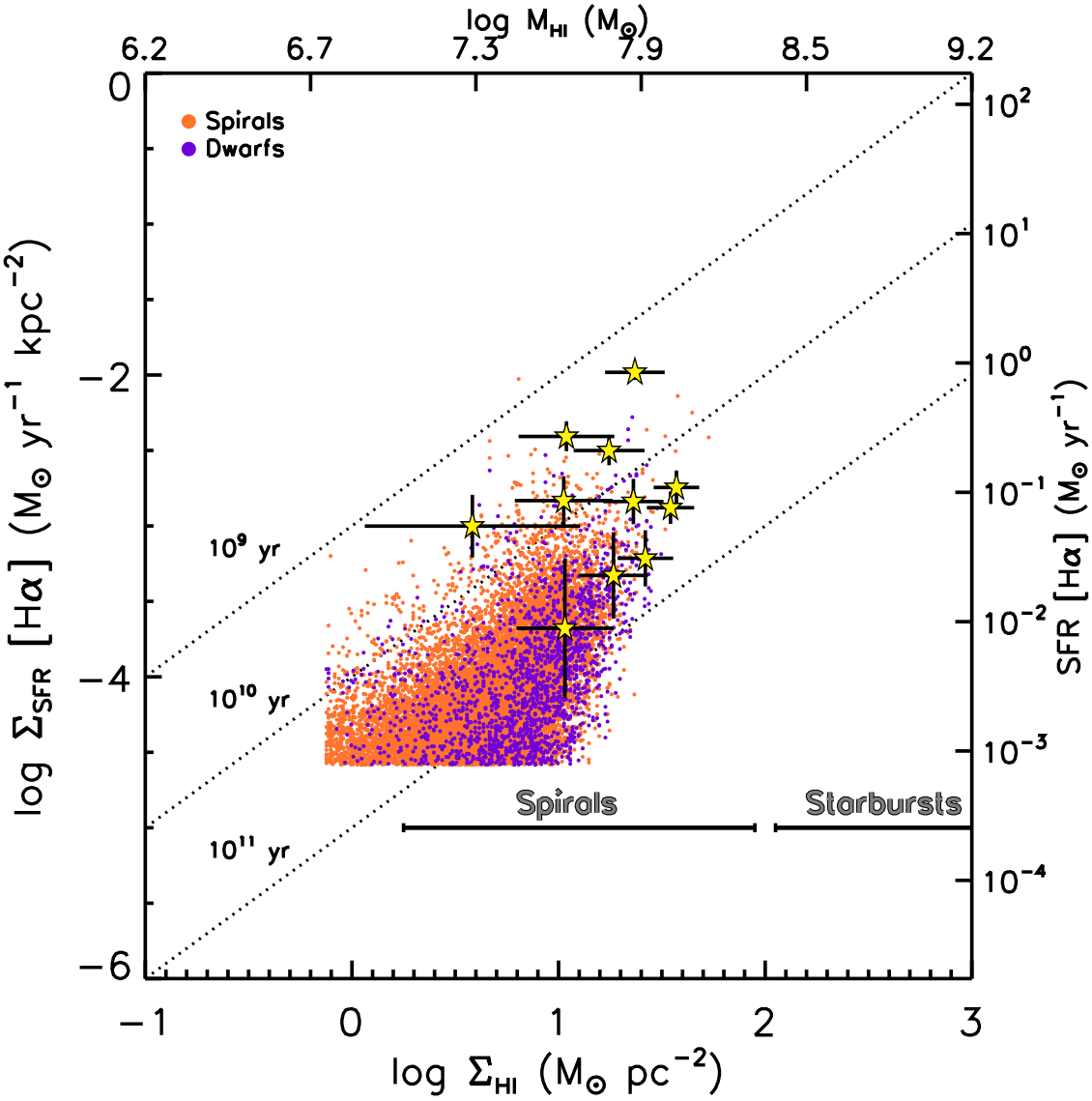

Fig. 24.— Spatially resolved SFR–HI gas surface density relation from measurements scales of 4.7 kpc in the outer regions of Arp 299. The mass ($M_{\rm HI}$) is calculated using the same aperture area (11″ in radius). Regions for the outer disks in normal spiral and dwarf galaxies on scales of 0.6-1 kpc are show as orange and purple circles, respectively from Bigiel et al. (2010).

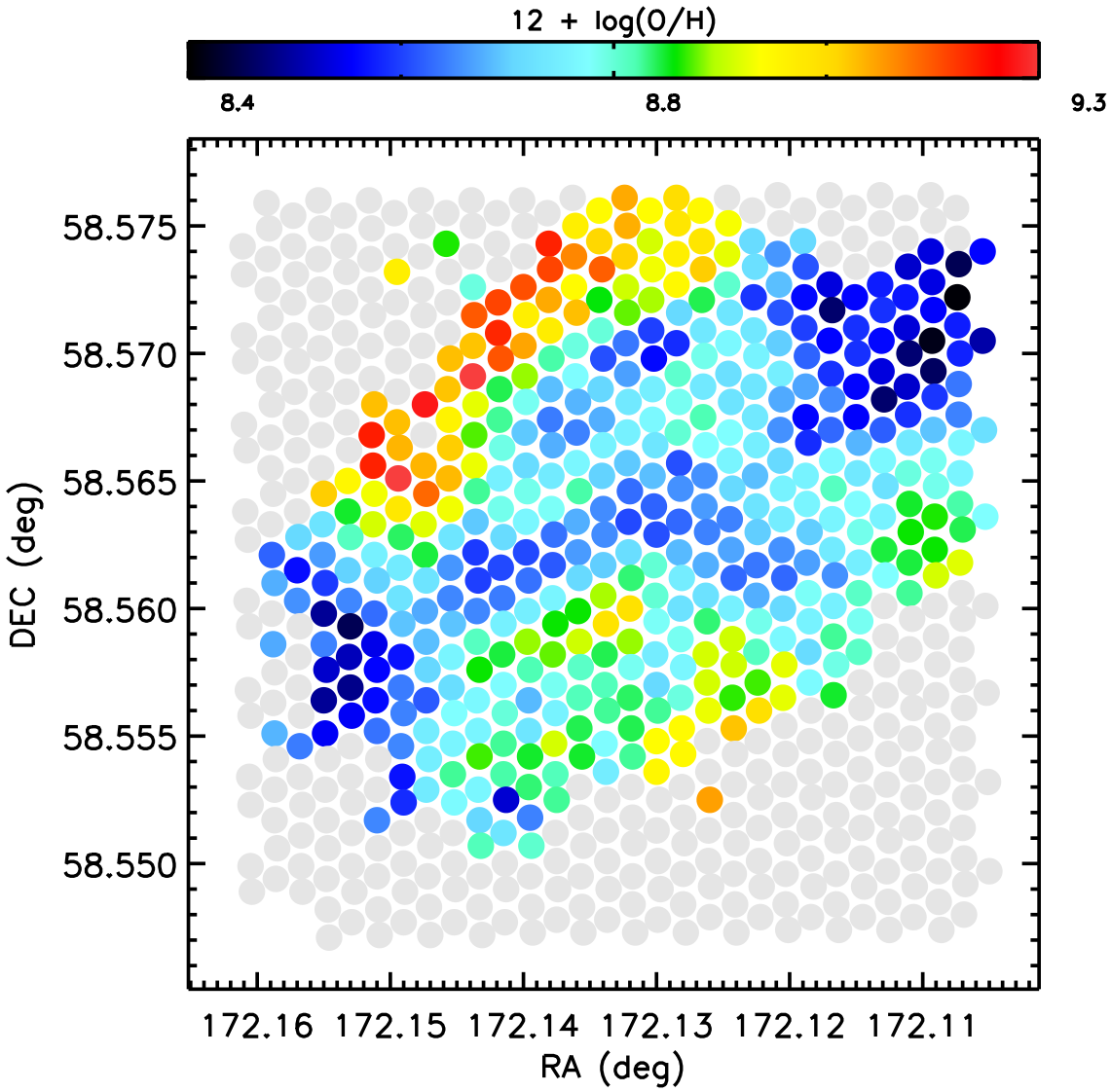

Fig. 25.— Metallicity using the N2 calibration from Pettini & Pagel (2004) and fiber [NII]/Hα line ratios.

Table 2. Global Star Formation Rates

Band	Luminosity 10^{42} erg s^{-1}	SFR $M_\odot$ yr^{-1}
(1)	(2)	(3)
IR (1-1000μm)[a]	1973±118	76.6±4.6
Hα, cor	$\geq 3.52 \pm 0.12$	$\geq$ 18.9±0.7
24 μm	$\geq$ 461±1.9	$\geq$ 43.6±6.3
Hα+24μm[b]	$L_{\mathrm{H}\alpha,\mathrm{obs}}+ 0.031 L_{24\mu\mathrm{m}} \geq 16.6 \pm 1.9$	$\geq$ 89.8±9.9
	$L_{\mathrm{H}\alpha,\mathrm{obs}} = 2.34$±0.01	-

Note. — Total IR luminosity calculated from F_{FIR}=1.26×10^{-14}(2.58F_{60} + F_{100}) (W m^{-2}) (Helou 1986) (F_{60}= 105.82 Jy, F_{100}=111.16 Jy from the IRAS galaxies and quasars catalog) and the ratio of total IR (1-1000μm) to FIR luminosity: $L_{\mathrm{IR}}/L_{\mathrm{FIR}} \sim$ 1.75, assuming a few percent contribution to the total IR luminosity from 1-8μm (Calzetti et al. 2000).

(b) Mixed Hα+24μm luminosity and SFR using the 24μm extinction corrected observed Hα luminosity using equation 6 from Murphy et al. (2011).

(1) Wavelength band; (2) Total luminosity in wavelength band above an observed Hα flux S/N of 5; (3) Star formation rate using same Kroupa (2001) IMF and SFR calibrations taken from Murphy et al. (2011).

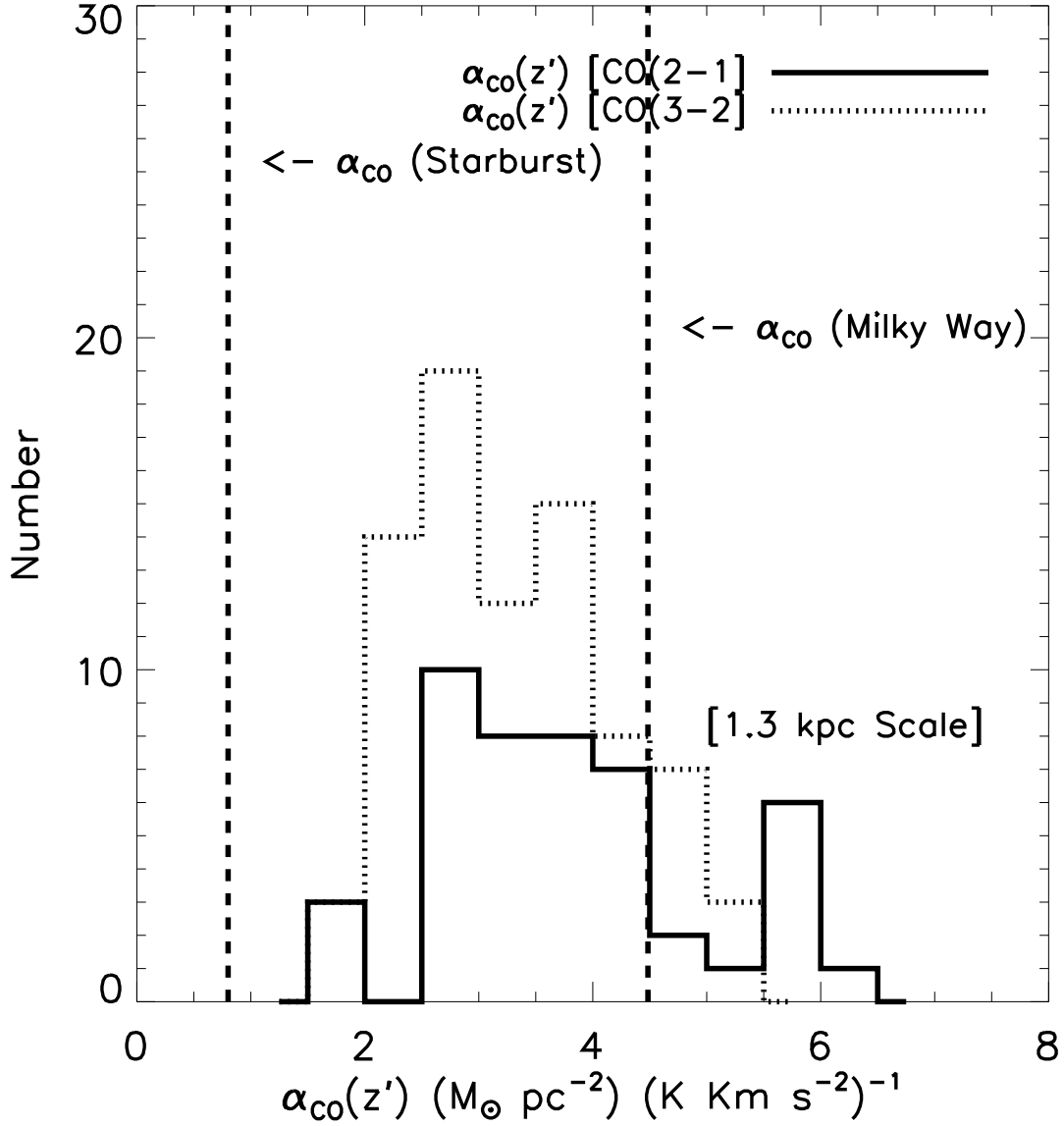

Fig. 26.— Metallicity dependent CO–to–H_2 conversion factor ($\alpha_{CO}(Z')$ from Narayanan et al. (2012) on scales of 1.3 kpc corresponding to the resolution of 24μm PSF for CO$J = 2 \rightarrow 1$ (solid black line) and CO$J = 3 \rightarrow 2$ (dotted black line). The commonly use single value starburst conversion factor (Downes & Solomon 1998) and Galactic conversion factor from (Bloemen et al. 1986) are shown by the dashed black lines.

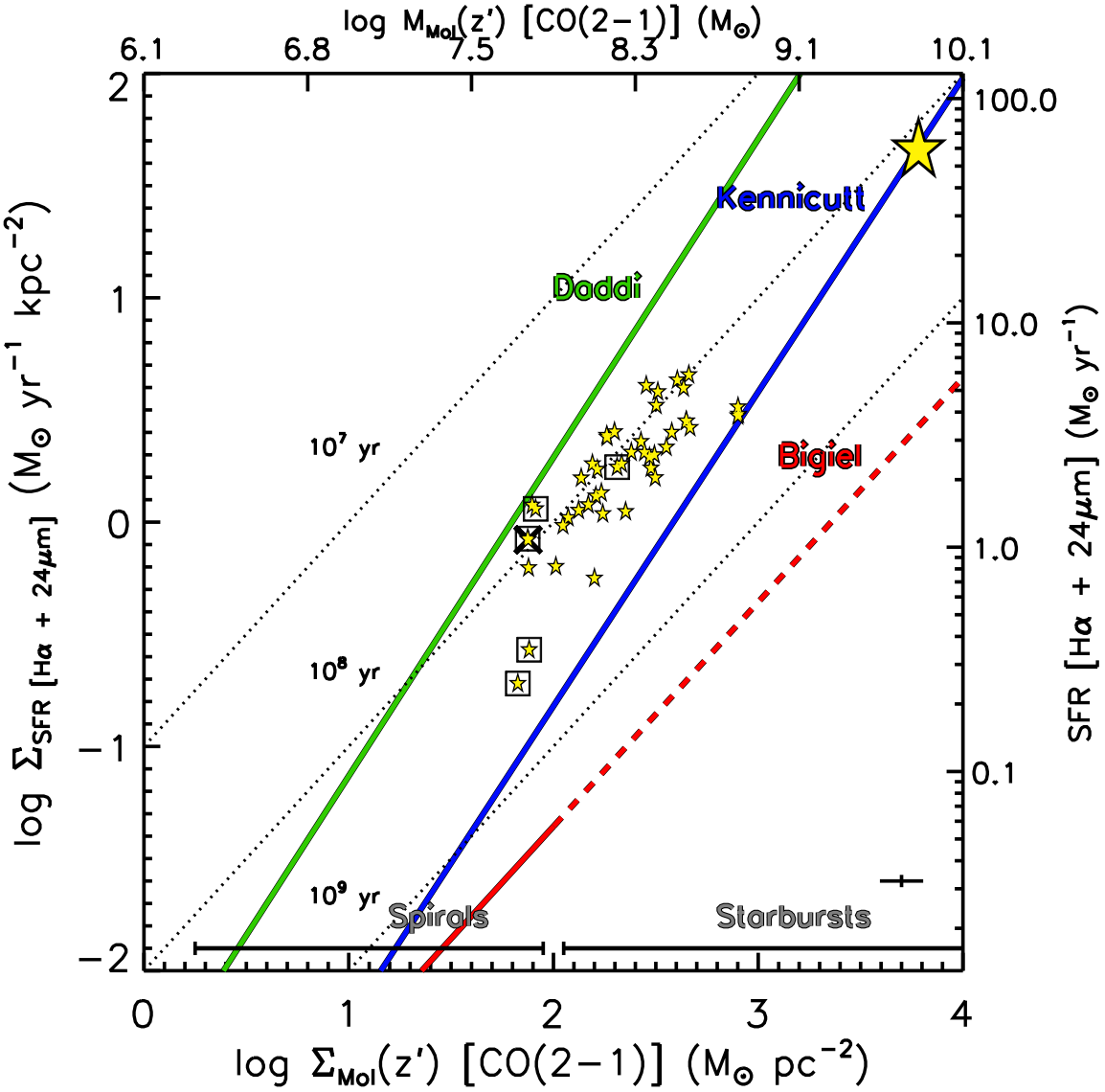

Fig. 27.— Spatially resolved SFR–Mol gas surface density relations from measurements at each IFU fiber position with CO$J = 2 \rightarrow 1$ coverage using a metallicity dependent conversion factor ($\alpha_{\rm CO}$(Z′)) from Narayanan et al. (2012) on scales of 1.3 kpc. The mass ($M_{\rm Mol}$) is calculated using the same aperture area (3″ in radius). The dotted vertical line is the sensitivity limit of the CO$J = 2 \rightarrow 1$ map. Large yellow star is the integrated value for Arp 299. Lines indicate extragalactic relations on disk-averaged scales for spirals and starbursts (blue line; Kennicutt (1998)) and high-z mergers (green line; Daddi et al. (2010)), as well as in 1 kpc regions in spirals and dwarf galaxies (red line; Bigiel et al. (2011)) AGN contaminated regions are marked with boxes from IFU line fluxes and black crosses (X-ray).

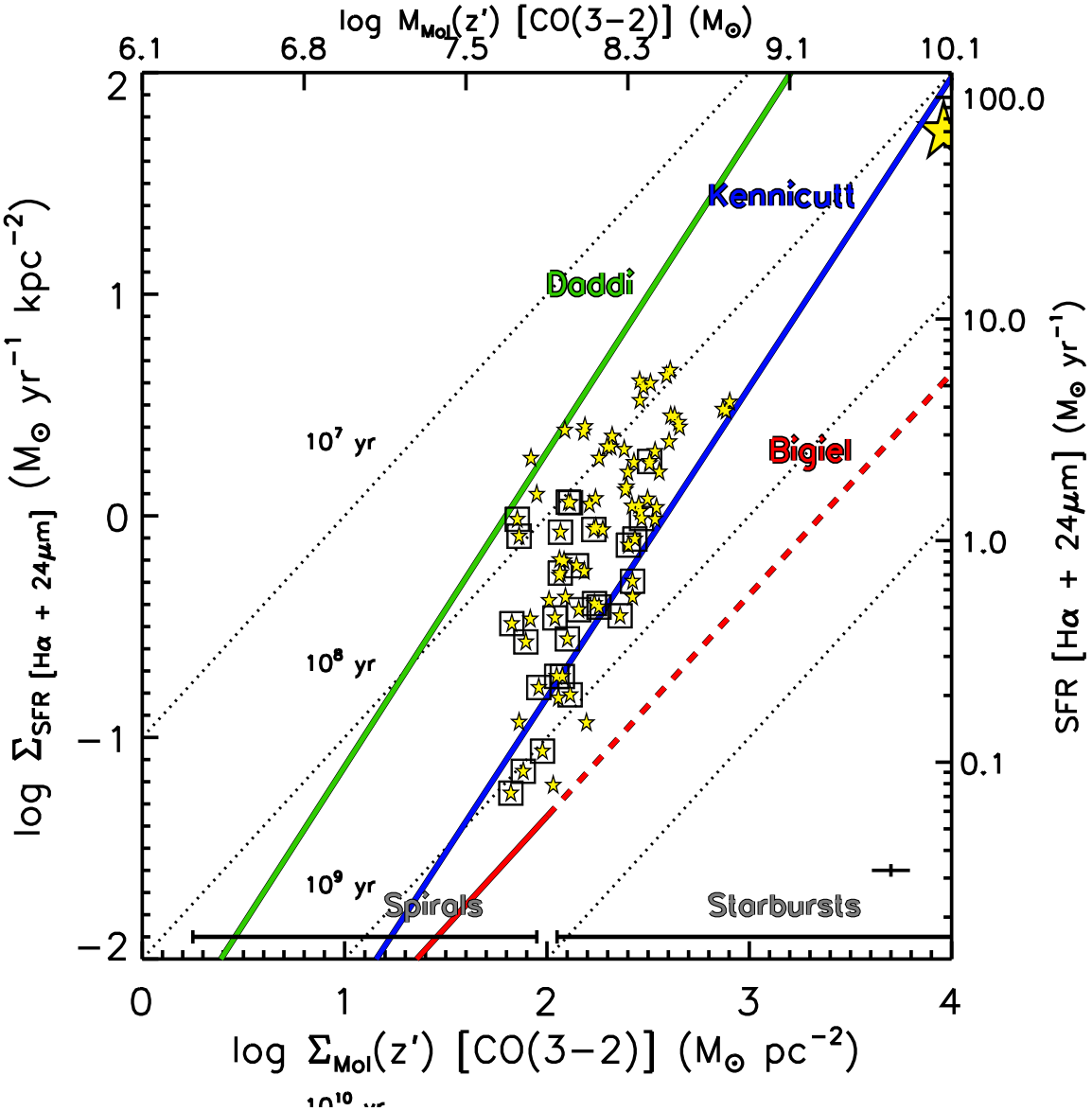

Fig. 28.— Spatially resolved SFR–Mol surface density relations from measurements at each IFU fiber position with CO$J = 3 \rightarrow 2$ coverage using a metallicity dependent conversion factor ($\alpha_{\rm CO}$(Z′))from Narayanan et al. (2012) on scales of 1.3 kpc. The mass ($M_{\rm Mol}$) is calculated using the same aperture area (3″ in radius). The dotted vertical line is the sensitivity limit of the CO$J = 2 \rightarrow 1$ map. Large yellow star is the integrated value for Arp 299. Lines indicate extragalactic relations on disk-averaged scales for spirals and starbursts (blue line; Kennicutt (1998)) and high-z mergers (green line; Daddi et al. (2010)), as well as in 1 kpc regions in spirals and dwarf galaxies (red line; Bigiel et al. (2011)). AGN contaminated regions are marked with boxes from IFU line fluxes.